SLOVAK UNIVERSITY OF TECHNOLOGY IN BRATISLAVA
FACULTY OF ELECTRICAL ENGINEERING AND
INFORMATION TECHNOLOGY

Signal Processing Techniques For Transverse Feedback Systems In Hadron Accelerators

PhD Thesis

Author: Dipl.Ing. Gerd Kotzian

October 2025

SLOVAK UNIVERSITY OF TECHNOLOGY IN BRATISLAVA
Faculty of Electrical Engineering and Information Technology
Institute of Electronics and Photonics

Signal Processing Techniques For Transverse Feedback Systems In Hadron Accelerators

PhD Thesis

Field of study: Electrical engineering
Subject of specialization: Electronics and Photonics

Registration number: FEI-104402-117003

Author: Dipl.Ing. Gerd Kotzian

Supervisor:
doc. Ing. Daniel Valúch, PhD.
Consultant:
prof. Ing. Viera Stopjaková, PhD.

Bratislava/Geneva, October 2025

Slovak University of Technology in Bratislava
Institute of Electronics and Phototonics

Faculty of Electrical Engineering and Information Technology
Academic year: 2025/2026
Reg. No.: FEI-104402-117003

DISSERTATION THESIS TOPIC

Student: **Dipl.-Ing. Gerd Kotzian**
Student's ID: 117003
Study programme: Electronics and Photonics
Study field: Electrical and Electronics Engineering
Thesis supervisor: doc. Ing. Daniel Valúch, PhD.
Head of department: doc. Ing. Anton Kuzma, PhD.
Consultant: prof. Ing. Viera Stopjaková, PhD.
Workplace: ÚEF FEI STU, CERN

Topic: **Signal processing techniques for transverse feedback systems in hadron accelerators**

Language of thesis: English

Specification of Assignment:

Identify and describe relevant parameters affecting the transverse feedback performance, such as: loop gain, feedback phase, delay, processing noise. Research and propose signal processing techniques and analysis algorithms that allow evaluating and quantifying the identified parameters.

Investigate and define methods to measure and set up the key feedback parameters represented by open and closed loop gain, feedback phase, loop delay. The method should be fast (in order of machine turns) and not destructive to the beam. The results should be accurate and easy to objectively interpret. Research and propose required signal processing techniques and analysis algorithms to perform the TFB set-up, using exclusively the TFB system without external instruments and available observables within.

Research and propose methods and required signal processing techniques to extract vital accelerator parameters in real-time from observables available within the transverse feedback system, at least bunch-by-bunch machine tune, damping time, or injection errors. Investigate the feasibility of these measurements from the injection transients (or active excitation) and from passive observation of the circulating beam.

Investigate the computational complexity of the proposed methods and signal processing techniques and evaluate how they could be realized for the respective accelerator (e.g. real-time processing in TFB FPGA, real-time processing in high-performance computing system, suitable only for offline processing etc.).

Research and propose advanced signal processing techniques to obtain a transverse feedback system that is more robust to variations in machine parameters, especially larger tune acceptance. Focus on FIR methods capable to compensate frequency dependent phase variations.

Deadline for submission of Dissertation thesis:	15. 10. 2025
Approval of assignment of Dissertation thesis:	13. 10. 2025
Assignment of Dissertation thesis approved by:	prof. Ing. Viera Stopjaková, PhD. – Chairperson of the field of study board

Declaration

I hereby declare that the following thesis has been elaborated on my own and no portion of the work referred to in this thesis has been submitted in support of an application for another degree or qualification of this or any other university or educational institute.

Geneva, October 2025 .....

Signature

Acknowledgement

I would like to thank my academic advisors, doc. Ing. Daniel Valúch, PhD. and prof. Ing. Viera Stopjaková, PhD., for supporting this work and making it happen.

My gratitude also extends to my colleagues: Adrian Menor De Onate, M.Sc., who talked me through challenging concepts as well as Dr. Kevin Li and Dr. Xavier Buffat, for their assistance with collective effects and the introduction to the pyHEADTAIL software. A heartfelt thanks to Benjamin Todd, B. Eng., PhD., C. Eng., whose unwavering support during the final stages of my thesis motivated me to fully recognize the importance of completing this work.

Last but not least, I am deeply grateful to my family for their constant moral support!

Anotácia

Techniky spracovania signálov pre systémy priečnej stabilizácie zväzku v hadrónových urýchľovačoch

Systémy priečnej stabilizácie zväzku sú vitálne pre hadrónové urýchľovače pracujúce s vysokou intenzitou zväzku.

Dôležitá súčasť takéhoto systému je výkonná jednotka digitálneho spracovania signálu. Súčasné číslicové technológie umožňujú implementáciu veľmi pokročilých algoritmov a analytických techník pre extrakciu dôležitých parametrov urýchľovača, alebo samotného spätnoväzobného systému.

Výskum sa bude zaoberať možnosťami extrakcie parametrov spätnoväzobného systému na základe matematických formalizmov teórie signálov a sústav s použitím aktívneho vybudenia obiehajúceho zväzku týmto systémom a len s použitím informácie získanej z tohoto systému. Minimálne skúmané parametre pre optimálnu prevádzku systému sú fáza a oneskorenie v uzavretej spätnoväzobnej slučke (vrátane zväzku). Súčasné techniky postavené na meraniach externými prístrojmi sú časovo veľmi náročné, poškodzujú obiehajúci zväzok a nedosahujú požadovanú presnosť.

Druhým cieľom výskumu je navrhnúť a implementovať metódy extrakcie kritických parametrov urýchľovača (parameter "tune" a časová konštanta útlmu oscilácií pre každý jednotlivý bunch) s použitím nedeštruktívnych manipulácií so zväzkom bez vytvárania strát častíc a degradácie kvality zväzku. Znalosť týchto parametrov je dôležitá pre dosiahnutie stability obiehajúceho zväzku a spoľahlivej prevádzky urýchľovača, ale v súčasnosti tieto parametre nie sú jednoducho, alebo vôbec dostupné.

Abstract

Signal processing techniques for transverse feedback systems in hadron accelerators

Transverse feedback systems are essential for stable operation of all hadron accelerators with high intensity beams.

An important component of such a system is a powerful digital signal processing unit. Current digital technology allows implementation of very advanced algorithms and analysis techniques to extract key parameters of the accelerator and the feedback itself.

The traditional techniques based on external instruments are time consuming, destructive to the beam and do not provide required precision. The research will aim at possibilities of feedback parameter extraction and performance optimization using only active manipulations of the beam by the transverse feedback system itself and analysis of data acquired from it. Based on formalisms of signals and systems theory, the minimum required parameters will be the closed loop phase and delay. These are essential for optimum feedback operation.

The second aim of the research will be to study and implement methods to extract vital accelerator parameters (e.g. the bunch by bunch machine tune and the damping time) using active manipulations of the beam by the transverse feedback system itself without degradation of the beam parameters. Accurate knowledge of these parameters is essential for ensuring beam stability and the reliable operation of the accelerator.

Easy access to these parameters is important for automated TFB setting up, performance monitoring, or efficient troubleshooting. This kind of information was not accessible until now.

Contents

CONTENTS

List of symbols and abbreviations

The next list describes several symbols that will be later used within the body of the document.

Abbreviations

ADC	Analog-to-digital converter
ADT	Transverse Feedback system at CERN for the LHC
CERN	European Organization for Nuclear Research
CPS	CERN Proton Synchrotron, a particle accelerator at CERN
DAC	Digital-to-analog converter
FFT	Fast Fourier transform
LEIR	Low Energy Ion Ring, a particle accelerator at CERN
LHC	Large Hadron Collider, a particle collider at CERN
PSB	Proton Synchrotron Booster, a particle accelerator at CERN
RF	Radio Frequency
RMS	Root mean square
SPS	Super Proton Synchrotron, a particle accelerator at CERN
SUSSIX	Computer code for frequency analysis of non-linear betatron motion
TFB	Transverse Feedback system
VNA	Vector Network Analyzer

LIST OF SYMBOLS AND ABBREVIATIONS

Physical constants

c	Speed of light in vacuum	$299\,792\,458\,\mathrm{m\,s^{-1}}$
m_p	Proton mass	$1.672\,621\,923\,69 \times 10^{-27}\,\mathrm{kg}$
$\mathsf{E_p}$	Proton mass energy equivalent in MeV	$938.272\,088\,16\,\mathrm{MeV}$
e	Euler's number	$2.718\,281\,828$

Accelerator physics quantities

$\vec{E}$	Electric field vector
E	Electric field, magnitude of $\vec{E}$
$\vec{B}$	Magnetic field vector
B	Magnetic field, magnitude of $\vec{B}$
$\vec{v}$	Velocity vector of a particle
v	velocity, magnitude of $\vec{v}$
$\vec{p}$	Vector momentum of a particle
p	Momentum, magnitude of $\vec{p}$
Δp	Off-momentum
p_0	Reference momentum
ξ	Chromaticity
ρ	Radius of curvature
m	Mass of a particle in motion
m_0	Rest mass
β_r	Relativistic beta, $v = \beta_r c$
γ_r	Lorentz factor, $m = \gamma_r m_0$
E	Particle energy

α	Optical Twiss parameter
β	Optical Twiss parameter
γ	Optical Twiss parameter
Q	Tune, number of betatron oscillations per turn
Q_f	Fractional part of Q
Q_i	Integer part of Q
Q_s	Longitudinal tune
x	Coordinate along the horizontal axis (radial direction)
x'	First derivative of x
x''	Second derivative of x
y	Coordinate along the vertical axis (axial direction)
y'	First derivative of y
y''	Second derivative of y
s	Coordinate along the longitudinal axis
C	Particle accelerator circumference
K	Magnet focusing function
ϵ	Beam emittance
ϵ_n	Normalized transverse beam emittance
σ	RMS beam size
q	Elementary particle charge
V_{cav}	Cavity voltage
T_{REV}	Revolution period
f_{REV}	Revolution frequency

T_{RF}	Period of the RF frequency
f_{RF}	Frequency of the RF cavity accelerating structure
h	Harmonic number $f_{RF} = hf_{REV}$
f_s	Synchrotron frequency
ϕ_s	Synchronous phase
U_{k}	Deflector kick voltage
θ_{kick}	Deflector kick angle
L_k	Deflector/kicker length
d_k	Deflector/kicker aperture
A	Oscillation amplitude
ψ	Phases advance
ϕ	Phase initial condition

Signal processing symbols

n	Index vector of discrete-time signals
x	Discrete-time signal
X	Complex frequency-domain (z-domain) representation of *x*
y	Discrete-time signal
Y	Complex frequency-domain (z-domain) representation of *y*
$\mathcal{Z}\{\cdot\}$	z-transform operator
j	Unit imaginary number $j^2 = -1$
$\lvert\cdot\rvert$	Absolute (magnitude) of a complex number, $\left\lvert Ae^{j\theta}\right\rvert = A$
arg$\{\cdot\}$	Argument of a complex number, *arg*$\left\{Ae^{j\theta}\right\} = \theta$
Re$\{\cdot\}$	Real part of a complex number, *Re*$\{x + jy\} = x$

$Im\{\cdot\}$	Imaginary part of a complex number, $Im\{x + jy\} = y$
α	Complex base
θ	Discrete-time signal of kicker action
Θ	Complex frequency-domain (z-domain) representation of θ
Λ	Linear map operator
X_{n}	Normalized coordinate
$X_{\mathrm{n}}{}'$	Normalized slope
$\mathbb{R}$	Set of all positive and negative integer numbers including zero
$\mathbb{R}^*$	Set of all integer numbers excluding zero, $\mathbb{R}^* = \{x \mid x \in \mathbb{R}, x \neq 0\}$
x	Complex notation of state vector $\boldsymbol{x}$
$\boldsymbol{x}$	State vector representing particle motion
t	Time
τ_{d}	Damping time constant
τ_{dec}	Decoherence time constant
τ_{inst}	Instability rise time constant
n_{d}	Damping time in numbers of turns
n_{dec}	Decoherence time in numbers of turns
n_{inst}	Instability rise time in numbers of turns
u	Unit step sequence
z	Complex number

LIST OF SYMBOLS AND ABBREVIATIONS

List of Figures

LIST OF FIGURES

List of Tables

Introduction

The *European Organization for Nuclear Research* (CERN) was founded in 1954. It is a particle physics laboratory situated at the border between Switzerland and France, where it operates a chain of particle accelerators in order to investigate the constituents of matter. The largest of these accelerators is the *Large Hadron Collider* (LHC) [4] depicted in Figure 1. With its circumference of $27\,\mathrm{km}$ it is the most powerful particle accelerator ever built [4] (at the time of writing). In the LHC two beams made up of protons or ions are accelerated to energies reaching $6.8\,\mathrm{TeV}$ and collide at four interaction points. Highly sophisticated particle detectors installed at these interaction points detect the fragments of the collisions and analyse their trajectories. The outcomes of these experiments are expected to give new insights in many fields of modern high energy physics and lead to a better understanding of the laws of nature.

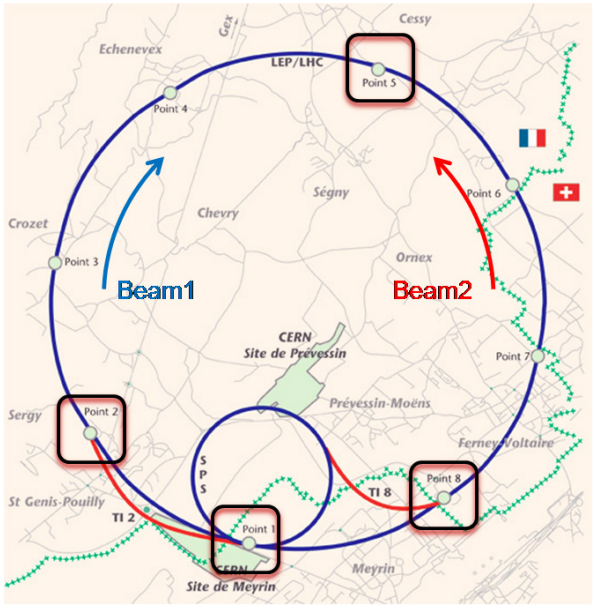

Figure 1: CERN and the LHC.

INTRODUCTION

Transverse Feedback systems (TFB) are an essential part of each high energy circular particle accelerator, regardless if proton [5–7], heavy ion [8, 9], electron-positron storage ring [10, 11] or a synchrotron light source [12, 13] to name only few.

Their task is to stabilize high intensity beams by suppressing any transverse instabilities driven by machine impedance [14, 15], reduce transverse motion induced by external perturbations [16, 17], or preserve emittance of the injected beam by rapid damping of injection oscillation transients [18, 19].

Working on these systems requires broad interdisciplinary skills and knowledge, for example, beam dynamics, analogue electronics, digital electronics, *Radio Frequency* (RF) engineering, high voltage systems, vacuum systems, high intensity beam interaction with the machine to name only few.

With the arrival of very powerful programmable digital electronics more than two decades ago, the data and signal processing hardware is no longer the limiting factor to the complexity of implemented algorithms and digital signal treatment. This opened completely new possibilities for transverse feedback systems in accelerators. The damping or stabilizing function of the transverse feedback is no longer the only service these systems are expected to provide. The TFBs are used now for example, for beam cleaning [20–22], real time transverse activity monitoring and instability detection [23] as well as beam transfer function measurement [24]. Transverse feedback can be a source of controlled machine impedance, allowing for special measurements such as direct Landau damping strength measurement [25], impedance measurement of individual accelerator components (e.g. low-impedance collimators) by means of high precision tune shift detection techniques [26] or impedance measurements of insertion devices in light sources by the grow-damp method [27]. With full-resolution beam position data now available in digital form [28], the focus has shifted beyond the core feedback functionality (which remains necessary) toward added-value services aimed at enhancing accelerator performance and operation.

Engineers working on transverse feedback systems need to thoroughly understand digital signal processing techniques to be able to identify their potential for TFBs, and the data provided by them. With modern digital technology, it is possible to extract the key parameters of the accelerator and the TFB itself from the TFB internal data streams. Such work involves also system design and digital signal processing which are subject of this thesis.

Chapter 1

Current state of the problem

1.1 TFB principle of operation

In Figure 1.1 the key components of a transverse feedback system are outlined. At the injection point where the beam is received from a previous accelerator using a transfer line, there are transverse oscillations launched around the target orbit due to imperfections in this process.

The beam position is measured every turn by one or more position monitors composed of a coupling device to the beam (pick-up) and signal conditioning electronics [29, 30]. This combination is often referred to as a beam position monitor or a beam position measurement module (BPM).

A correction signal is then calculated based on the position data and transformed to the point in the accelerator where the transverse kicker is located such that the overall phase in the feedback loop is negative and the loop is stabilizing the beam. In the early days, the calculation of feedback signals was fully analog, using filters and delay lines, often hundreds of meters [5, 31], or even a few kilometers long [32]. The time alignment of the processing chain delay T_{signal} to the beam time-of-flight T_{beam} between the position monitors and the transverse kicker is a crucial factor for the transverse feedback to work correctly. Fixed cable delays are not compatible with accelerating beams, so complicated tricks needed to be implemented to cope with a decreasing time-of-flight delay T_{beam} during the energy ramp [33].

If multiple beam position monitors can be installed in the machine with an ideal 90°

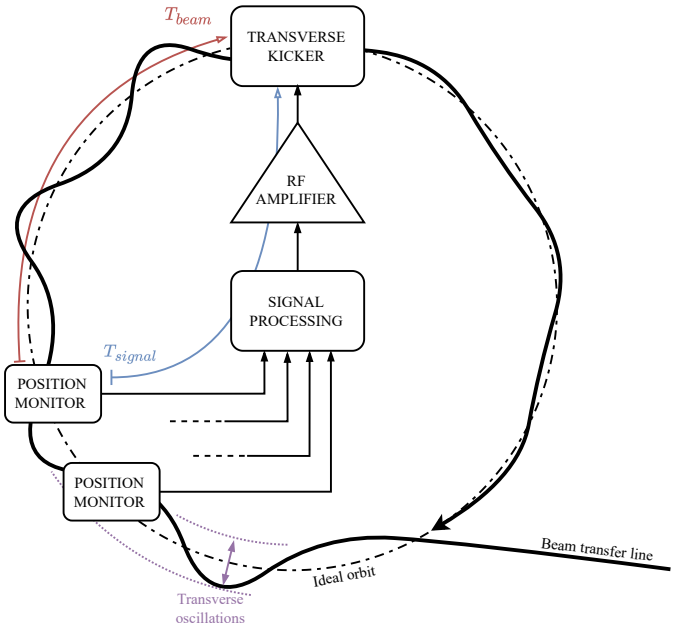

Figure 1.1: Principle blocks of a transverse feedback system in a circular particle accelerator.

betatron phase advance between them, the required feedback phase can be obtained by (analog) vector combination of the two (or more) position signals creating a "virtual pick-up"[34].

The correction signals are finally amplified and fed to kickers which deflect the beam and close the feedback. When a lower deflection voltage and high bandwidth is needed, typically terminated strip-line kickers and solid state amplifiers are used (e.g. [35]). If a high deflection is needed e.g. for highly relativistic beams, high power tetrode based amplifiers feeding unterminated E-field kickers are often used (e.g. [36]).

The availability of the first fast analog to digital converters and digital memories immediately allowed for the replacement of the bulky fixed cable delay lines and introduced the possibility for the TFB to follow the accelerating cycle. For example, at CERN's Super Proton Synchrotron, these efforts date back to the beginning of the 1980s [37–39]. With advancements in digital technology in the 1990s the next natural step was to introduce full digital signal processing with digital filtering [40].

In hadron machines, bunch length is comparable with the length of the RF bucket. In smaller synchrotrons, this is typically hundreds of nanoseconds. Digital low-level RF systems therefore can sample the passing bunch at many points and can easily detect an intra-bunch motion. If such a TFB is equipped with pickups and deflectors with sufficient bandwidth, an intra-bunch feedback can be realized to stabilize the head-tail

motion. A great example of upgrade of a regular "mode-0 only" transverse feedback to a 64-slice intra-bunch feedback is the J-PARC's Main Ring TFB project [41]. Bunch length in the largest synchrotrons is typically nanoseconds, but modern multi giga-sample per second digital systems and GHz bandwidth amplifiers and kickers allow us to also realize intra-bunch feedbacks capable of stabilizing head-tail motion of such short bunches [42].

Today's digital technology offers virtually unlimited resources for advanced signal processing and data storage.

1.2 TFB technology, key parameters, and their determination

Key TFB parameters are the closed loop gain, feedback phase and loop delay. Their adjustment and monitoring is essential for correct feedback operation. However, for machines like the LHC, only the correct operation of the TFB is not enough, we must achieve optimal (and beyond) operation [43, 44].

Transverse feedback systems were introduced in the early days as a remedy against resistive-wall transverse beam instabilities (due to the increasing beam intensity). Back at the time, the engineers had identified which were the key parameters of the TFB and they designed procedures to adjust them [10, 12, 32, 45–48]. Nevertheless, they did not have the means to directly measure, or determine these parameters. The TFB setting-up involved a lot of indirect methods, observation of beam losses while scanning parameters, finding the loop stability limit by monitoring the transmission, and some "educated guesswork" or gut feelings.

Loop delay settings, for example, are an important factor contributing to the phase margin of transverse feedback systems [10]. In particular, the loop delay is directly related to the usable bandwidth of a TFB, that is, the maximum frequency f_{max}. The phase shift $\Delta\varphi$ introduced by delay mismatch ΔT at a given frequency, is described by the formula

$$\Delta\varphi = 360^\circ \Delta T f. \tag{1.1}$$

Considering a feedback system which is designated for and operated up to $100\,\mathrm{MHz}$, as for the CERN *Proton Synchrotron Booster* (PSB) [49], one obtains from (1.1) a

maximum allowed delay error of $0.25\,\mathrm{ns}$ to not exceed an acceptable phase error of 10°. This means that all delays contributing to the control loop, such as cable connections, RF amplifier components, or signal and filter processing delays, must be known and adjusted with a high degree of accuracy, otherwise the anticipated TFB performance might not be reachable.

As an added complication, continuous adjustments of a TFB's loop delay are required within the acceleration cycle, to compensate for the propagation delay changes as particles are getting faster. This problem was addressed as early as in the 1960s. First TFB control loops were built which used switchable coaxial delays for automatic delay compensation [50–53] as the beam was accelerated. The implementation in 1977 was based on hard-wired *Emitter Coupled Logic* (ECL) gates, and allowed variable delays of $2.7\,\mathrm{ns}$ discrete step size, and a 9-bit digital control word [51]. The same technology was exploited for the PSB [48], and further improved for a step resolution of $1\,\mathrm{ns}$. This implied that the tolerance of the delay adjustment had to be further improved to better than a fraction of a nanosecond in order to reach the target bandwidth.

At the time, having had no other means to evaluate the overall loop delay, each individual component of the TFB signal chain needed to be measured. Its group delay and other electrical parameters were entered into a table. The total loop delay was worked out manually. The example in Table 1.1 shows the evaluation of the TFB closed loop delay in the four PSB rings. Each row contains data about one system element, evaluated for both planes. These listed values had to be determined to within a fraction of a nanosecond since the table was used to calculate the final values for the fixed and variable delays to be programmed into the hardware. This method relied on systematic and accurate measurements of each and every contributing delay and other system parameters, making it quite labour intensive and prone to all sorts of errors. This is what we call the "Spread-sheet method", which was used for many years.

Later methods of measuring the loop phase and delay involved external instruments such a *Vector Network Analyser* (VNA). A VNA is an active device that measures complex transfer functions of a system. The instrument injects a sinusoidal excitation and measures the frequency response in a complex format. The VNA can be used as a standard RF instrument to measure transfer functions of individual RF devices (TFB building blocks, like amplifiers, cables, or filters), or an overall transfer function of the entire TFB system including the beam. As an example, Figure 1.2 shows two measurements of a circulating beam in the CERN *Super Proton Synchrotron* (SPS) accelerator using a classical VNA to estimate the feedback parameter settings of an active

	R1H	R1V	R2H	R2V	R3H	R3V	R4H	R4V
PU 4L5	–	–	–	–	–	–	–	–
	3.7	3.7	3.7	3.7	3.7	3.7	3.7	3.7
Head Amplifier	2.6	2.6	2.6	2.6	2.6	2.6	2.6	2.6
	100.4	100.5	98	98.1	94.1	94.1	101.6	101.6
PP BAT	0.1	0.1	0.1	0.1	0.1	0.1	0.1	0.1
	8	8	8	8	8	8	8	8
BOSS (out 1)	8.5	8.5	8.5	8.5	8.5	8.5	8.5	8.5
	16	16	16	16	16	16	16	16
DSPU Tfix	20.5	20.5	20.5	20.5	20.5	20.5	20.5	20.5
	10	10	10	10	10	10	10	10
SP2T	11	11	11.5	11.5	11.5	11.5	11	11
	16	16	16	16	16	16	16	16
4W Driver	10.5	10.5	10.5	10.5	10.5	10.5	10.5	10.5
	10	10	10	10	10	10	10	10
800 W amplifier	36	36	36	36	36	36	36	36
	10	10	10	10	10	10	10	10
PP BAT	0.1	0.1	0.1	0.1	0.1	0.1	0.1	0.1
	117.2	117.1	123.5	123.4	138.7	138.6	145.1	144.9
Kicker 3L1	2.6	2.6	2.6	2.6	2.6	2.6	2.6	2.6
	125.4	125.6	126.4	127.5	138.2	138	150.1	148.9
PP BAT	0.1	0.1	0.1	0.1	0.1	0.1	0.1	0.1
	10	10	10	10	10	10	10	10
Power Atten.	1.2	1.2	1.2	1.2	1.2	1.2	1.2	1.2
Tfix	381.9	381.9	386.3	386.3	397.6	397.5	411.0	410.8
TDSPU	425	425	425	425	425	425	425	425
Tbeam-min	489.9	489.9	489.9	489.9	489.9	489.9	489.9	489.9
Tbeam-max	1491.1	1491.1	1491.1	1491.1	1491.1	1491.1	1491.1	1491.13
VarDelMax	**1109.2**	**1109.2**	**1104.8**	**1104.8**	**1093.5**	**1093.6**	**1080.1**	**1080.3**
VarDelMin	**108.0**	**108.0**	**103.6**	**103.6**	**92.3**	**92.4**	**78.9**	**79.1**

Table 1.1: Calculation of Coarse and Fine delays for PSB TFB. Values are expressed in nanoseconds.

transverse feedback. The measurements presented were made in the early ∼2000's, and the method has not evolved much since then.

Measuring the system transfer function through the beam provides a basis for evaluating TFB parameters and performance, but many problems remain. The beam circulating in the machine must already be stable without the feedback, which is not always the case. In cycling machines, the beam circulates for only a few seconds (as little as $500\,\mathrm{ms}$

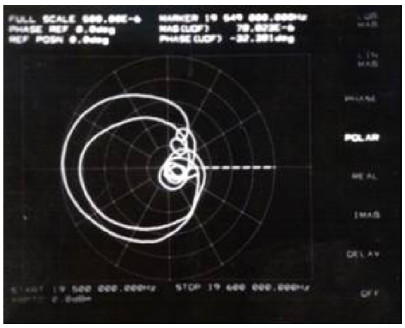

(a) Horizontal plane @20 MHz

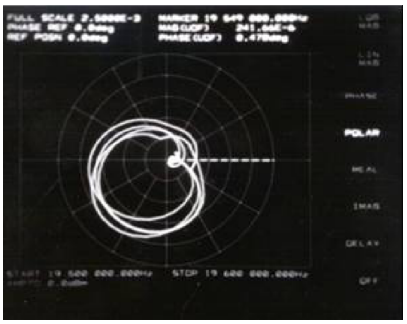

(b) Vertical plane @20 MHz

Figure 1.2: Use of a VNA to measure the beam transfer function with active TFB[1].

in the injector chain, up to $14\,\mathrm{s}$ in the larger synchrotrons). In the PSB, the time required for a meaningful measurement is at least $100\,\mathrm{ms}$. As the PSB cycle does not include a period when the machine is not accelerating (so-called flat top), it required preparation of a special magnetic cycle dedicated for TFB VNA measurements [1]. The creation of a dedicated machine cycle means additional work for the operators to configure, adjust, and verify the accelerator and all necessary components – time-consuming and cost-intensive tasks.

Another problem arises from the noise floor of the VNA instrument and its dynamic range. To obtain only remotely usable readings, many circulating bunches must be excited in order to obtain a sufficiently high return signal for the VNA. However, transverse feedbacks are essential for stable accelerator operation and TFBs are one of the first systems to be set-up. Large machines like the LHC are typically not able to handle more than a few circulating bunches at this stage. In case of the LHC, this is typically 5 to 8 individual bunches (out of 3564 possible) of very low intensity ($< 1/10$ of maximum). A train of nominal intensity bunches is unstable without a fully functional TFB. The use of a VNA to measure the TFB parameters is therefore extremely delicate at this point in time.

The use of the VNA technique in the LHC suffers from another problem - the LHC is the largest particle accelerator ever built. With a circumference of $27\,\mathrm{km}$, one turn takes $88.9\,\mu\mathrm{s}$ at almost the speed of light. The circulating bunches must be evenly spaced around the machine circumference to provide the VNA with regular repetitive response signals, otherwise it cannot measure anything useful within the frequency point measurement window. Increasing the measurement time does not help, since prolonged

[1] Taken from [4], section 14.3.2 on page 100. The images are reproduced in their original quality as provided in the publication.

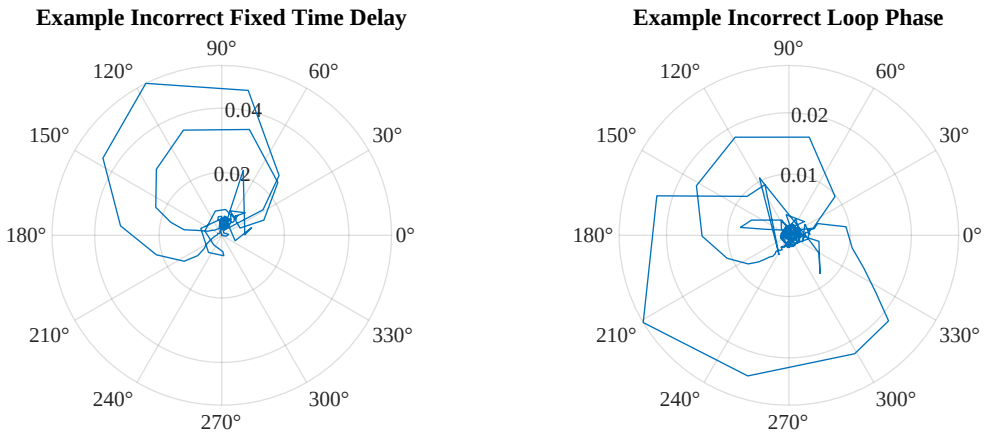

(a) Incorrect delay

(b) Incorrect phase

Figure 1.3: Adjustment of loop delay and feedback phase in the PSB using a VNA [1]. Left: the resonant lobes overlap but do not point towards $180°$. Right: both resonant lobes deviate evenly from the target value ($180°$).

exposure of the beam to the VNA excitation causes it to oscillate in the lattice, rapidly increasing its transverse emittance, and quickly losing the beam at the collimators.

VNA measurements are typically destructive to the beam, very time consuming, and do not provide the required accuracy. The interpretation of the results is not easy because the VNA measures not only the TFB but the entire accelerator. For example, the VNA method was used to set-up and validate the TFB in the PSB accelerator (see Figure 1.3, showing incorrect loop delay setting and incorrect feedback phase configuration). If the system was already in a reasonable state (e.g. the beam position monitor gain was adjusted, and the coarse cable delays were reasonably trimmed), setting it up for one beam type easily took a whole day. The VNA method, with many minor improvements is used at the LHC, but it still takes a full 8 hour shift to set up and validate the TFB performance here. With operating costs of 42'000 € per hour[1] and extremely scarce machine time, this is definitely not ideal.

In the CERN PS Booster, after the VNA measurements with dedicated cycles, also the phase scan measurements were performed, to validate the TFB system performace [1]. The TFB was set in closed loop mode and for a given accelerator tune the feedback phase was scanned over the entire range from 0 to 360 degrees. The beam transmission was measured over the plateau. Phase scans allowed identification of an optimal loop

[1] Assuming 1.1 billion CHF allocated resources for 2009-2012, 9 months of LHC operation per year, and an exchange rate of $1\,\mathrm{CHF}{=}1\,€$.

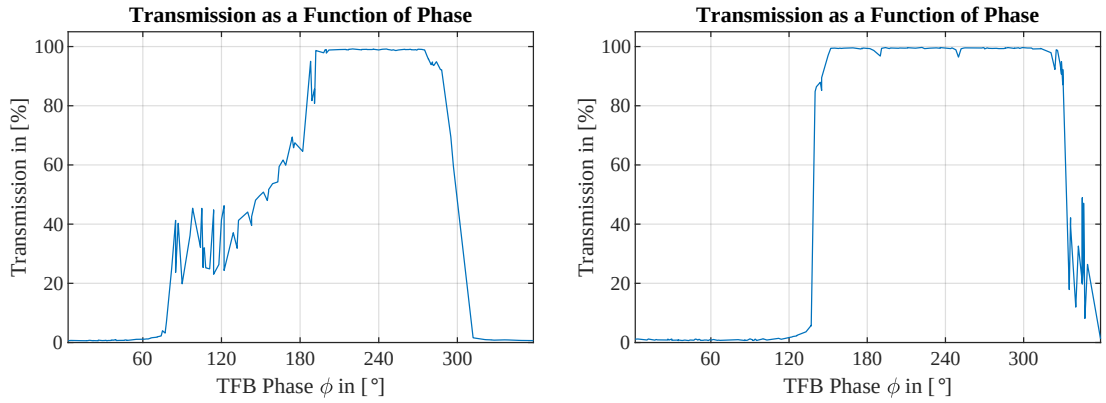

(a) Phase scan before adjusting time delay.

(b) Phase scan after adjusting time delay.

Figure 1.4: Evaluation of PSB beam transmission as a function of TFB feedback phase. Left: initial setting. Right: after loop delay adjustment with the VNA.

gain as well as evaluation of the feedback phase margin. An example of the performance insight obtained is shown in Fig. 1.4. In this example, the loop phase was scanned before and after the loop delay optimisation. It visually illustrates how incorrect delay (and its contribution to the phase error, see (1.1)) can result in reduced phase margin and hence sub-optimal performance of the TFB system, as assessed by measuring and evaluating beam transmission. It is worth noting that one measurement point is one machine cycle, so it is an extremely time-consuming validation process. An important point to note here is that if there is no transmission (as for example in Fig. 1.4 where the value along the y-axis dropped below $100\,\%$ for certain TFB Phase settings), the beam will be lost in the machine. This inevitably increases the radiation exposure of the accelerator components, which should always be kept as low as possible.

Since the tune in the PSB is dynamically changed during the cycle, the digital TFB system was designed with the ability to program the feedback phase along the cycle. Depending on the accuracy of the pre-calculated function, this guarantees optimal performance at any point in the cycle. Phase scans were repeated for several horizontal tunes spanning the current PSB operation working range, from $\mathrm{Q_H} = 4.10$ to 4.40. This step made it possible to validate the correctness of the phase mapping as a function of the tune in the hardware. Excellent agreement between the measurements and the simulation was observed (see Fig. 1.5), however it took several hours of machine time to obtain all the data for this graph.

We can use modern signal processing techniques and methods to quickly and accurately measure the overall TFB performance. This allows us to optimize the TFB system,

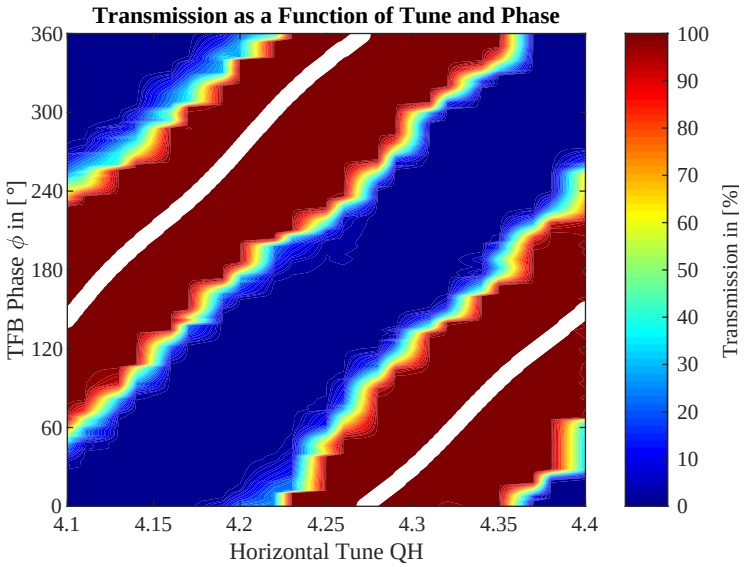

Figure 1.5: PSB transmission measurement as a function of machine tune and TFB phase setting. The white trace corresponds to the mapped horizontal tune as a function of the phase.

compensate for hardware imperfections, dynamically reconfigure the TFB performance through the machine cycle, provide individually tailored TFBs for different bunches, or sub-sets of bunches in the fill, and many more.

There is a strong need to research and introduce novel methods that will allow the TFBs to be set up in an accurate, scientific, fast, and efficient way. Novel methods, which will ideally not rely on any external instruments, but should fully utilize the potential of the TFB's digital signal processing hardware. Topics of this thesis.

1.3 Analogue and digital signal processing for TFBs

The TFBs act as a closed-loop feedback systems, taking the measurement of the instantaneous beam position as input and feeding a kicker that acts on the transverse momentum. The measured quantity (position) and the actuator action (momentum) are not of the same kind, so a conversion from position to correction kick requires some transformation. Historically, this has been achieved through various techniques [10, 32, 46, 54–56]. The sensors had to be positioned in the accelerator lattice such that the total phase shift between the sensor and the kicker provided the position to momentum

conversion. However, this is not always possible. In [32, 57], one solution to this utilized two independent position sensors spaced 90° apart in the lattice. Their output signals formed in-phase and quadrature components that could be combined in an analogue domain to provide the desired vector rotation. Beneficial to this, the actuator position in the lattice is no longer constrained to a favourable phase advance position, which relaxes some machine design constraints.

With the introduction of the first generation digital technology, it became possible to use very simple digital filters to process the sensor data. In 1984, the three pioneers at CERN, Bossart, Lambert and Louwerse introduced a very simple digital finite impulse response filter made out of hard-wired ECL gates, multipliers and adders. The filter was tested in the SPS [53, 58]. The demonstrator worked, but the idea was ahead of the available 8-bit technology – the resolution was not sufficient for operation in the accelerator [59]. Years later, an improved logic was implemented in a *Field Programmable Gate Array* (FPGA) [60]. The digital system made it possible to overcome some of the limitations of earlier analogue technology, such as temperature dependence, immunity to noise and interference, non-linearities, dynamic parameter reconfiguration, loss-less data transmission over long distances, and others.

State-of-the-art particle accelerators require state-of-the-art transverse feedback systems. With machines like the LHC and its injectors, machine optics change on the fly, TFB performance is critical, and feedbacks are operated at the stability limit defined by processing delay and the gain/phase margins. There is a strong need for research and adoption of novel signal processing methods that make it possible to extend the tune acceptance range, minimize processing delay to allow for higher gains or margins, design signal processing methods that allow dynamical reconfiguration as the machine accelerates the beam through the cycle. Topics that this thesis will cover.

1.4 Extraction of valuable machine parameters from TFB data

Modern TFBs are based on powerful digital technology. The system has digital information available about the bunch by bunch, turn by turn beam position for all bunches and a history of turns, all from several independent sensors distributed in the machine (in LHC four sensors per beam per plane, 16 in total). In addition, the digital

systems can synthesize virtually any signal to excite the beam using the same deflectors already used for the transverse feedback functionality.

Fully digital transverse feedback systems are a game changer. Suddenly, extremely valuable information about the accelerator and the circulating beam could be made available to the machine operators and accelerator scientists. Availability of the bunch by bunch and turn by turn position information opens completely new possibilities for the extraction and monitoring of machine parameters. Thanks to powerful, modern computing systems, these can even be extracted in real-time. With a good understanding of signal processing theory and techniques and the availability of powerful technology, we can go even further. Get the real-time data from the TFB, process it by computation-intensive algorithms and use it for various real-time feedbacks in the machine. As an example, the available data was used to demonstrate the proof-of-principle direct measurement of the Landau damping strength in LHC [25].

Tune is a critical machine parameter, precise knowledge of which is essential for accelerator operation. In high-intensity machines, where collective effects play an important role, the tune is not only a function of the magnetic lattice, but also of the beam intensity, the machine impedance, and the interaction between the beams via the wake fields. The LHC can accelerate up to 2808 bunches distributed in 3564 possible positions. Typically, the beam circulates in a form of tightly spaced bunch trains. Up to 288 bunches per train can be injected into the LHC. Additional tune shift is introduced by the beam itself, with a different value for each individual bunch in the train. The effect can be caused by beam-beam effects (so called Pacman bunches)[61, 62], by machine impedance [63, 64] or by electron cloud [65]. In order to operate machines like the LHC, it becomes important to measure the bunch by bunch tune, something unprecedented until now. The problem is even more difficult since the measurement must be accurate to a resolution of at least 10^{-3}, preferably 10^{-4}.

Tune measurement, in a regime of strong damping by an active transverse feedback system is a challenge even for the regular LHC tune measurement system called BBQ [66, 67]. Due to the analogue way of measuring the tune by the BBQ system, it is not possible to measure the tune for individual circulating bunches. With some gating in the RF domain, an average tune value can be obtained for a group of consecutive bunches [68]. However, measuring bunch by bunch tune values by traditional RF methods is unattainable. The TFB has digital information about the transverse position of each bunch, so using the TFB data to measure and extract the tune is an attractive idea. Similar to the BBQ, even digital bunch by bunch tune measurement in a strong damping

regime is very challenging, especially for FFT based algorithms (e.g. SUSSIX [69]), or curve fitting tools. There is a strong interest in researching and developing novel methods that allow extracting bunch by bunch tune information in real-time with a resolution of 10^{-3} or better. Topics that this thesis will address.

1.5 TFB status monitoring

An important aspect of TFB operation is constant monitoring of the system status. A well-known wisdom says: complex systems break in complex ways. When operating machines such as the LHC or its injectors, complex problems are the order of the day. Typically, it is not immediately apparent what the root cause of the emerging or already existing problem is. In such situations the operations group contacts the equipment experts with a request to verify that their system is functioning well. Answering the famous operator's question *Is the damper damping?* is more difficult than it might seem.

There is a strong interest in exploring and introducing a simple, well-defined parameter, a single number, or defining a simple method (that can be automated), which makes it possible to answer this question – *Yes, the TFB is functioning well, and the damper is damping*. A subject that is addressed by this thesis.

Chapter 2

Research objectives

In line with the analysis of the current state of the problem and the work motivation, the research objectives for this thesis are stated as follows:

Objective #1:

Identify and describe relevant parameters affecting the transverse feedback performance, such as: loop gain, feedback phase, delay, processing noise.

Research and propose signal processing techniques and analysis algorithms that allow evaluating and quantifying the identified parameters. The method should also be applicable to automatic performance verification while the machine is operated with beam.

Objective #2:

Investigate and define methods to measure and set up the key feedback parameters represented by open and closed loop gain, feedback phase, loop delay. The method should be fast (in order of machine turns) and preferably not destructive to the beam. The results should be accurate and easy to objectively interpret. The results should be usable directly for automated transverse feedback setting-up.

Research and propose required signal processing techniques and analysis algorithms to perform the TFB set-up, using exclusively the TFB system without external instruments and available observables within.

Objective #3:

Research and propose methods and required signal processing techniques to extract vital accelerator parameters in real-time, from observables available within the transverse feedback system, at least bunch-by-bunch machine tune, damping time, injection errors, or injection kicker waveform. Investigate the feasibility of these measurements from the injection transients (or active excitation) and from passive observation of the circulating beam.

Objective #4:

Investigate the computational complexity of the proposed methods and signal processing techniques and evaluate how they could be realized for the respective accelerator (e.g. real-time processing in TFB FPGA, real-time processing in high-performance computing system, suitable only for offline processing).

Objective #5:

Research and propose advanced signal processing techniques to obtain a transverse feedback system that is more robust to variations in machine parameters, especially larger tune acceptance. Focus on FIR methods capable to compensate frequency dependent phase variations.

Chapter 3

Background - Introduction to beam dynamics

3.1 Basis of charged particle acceleration

Both electrons and protons are elementary particles with a property charge – when subjected to an electric field or a time-varying magnetic field they experience a force, resulting in a change of their initial momentum, denoted as $\vec{p}$,

$$\frac{d\vec{p}}{dt} = q\left(\vec{E} + \vec{v} \times \vec{B}\right). \tag{3.1}$$

This equation is known as the Lorentz's force [70–72]. As can be seen, the electric field $\vec{E}$ deflects a charge q in the direction of the field, while a magnetic field $\vec{B}$ acts perpendicular to the particle's velocity $\vec{v}$.

The force from the magnetic field has the advantage that it scales with the speed of the particle. For accelerators that operate close to the speed of light, this means a benefit by a factor of $\approx 3 \times 10^8$. Therefore, in a circular particle accelerator, magnetic fields keep the charged particles on their trajectories around the machine and for one complete revolution, while electrical fields change their momentum in either the *longitudinal* direction, i.e. azimuthal, or in a *transverse* plane (horizontal/radial or vertical).

According to the cross product in (3.1) the vertical bending fields cause a horizontal deflection force. This is exploited by rewriting (3.1) in cylindrical coordinates, to formulate an equation for the radial motion. As a simplified condition for a circular orbit, one

could assume that the Lorentz force acting on a particle with mass m is equal to the centrifugal force, i.e.

$$qvB = \frac{mv^2}{\rho}. \tag{3.2}$$

Rearranging the last equation results in

$$B\rho = \frac{p}{q}, \tag{3.3}$$

what is known as the "momentum rigidity": If the momentum p is increased by an accelerating electric field, then the magnetic field B must increase by the same factor in order to keep the radius of curvature ρ constant. In the LHC, for example, the particles are injected with momentum $450\,\mathrm{GeV/c}$ and are accelerated to $6.8\,\mathrm{TeV/c}$. Correspondingly, the magnetic field is ramped up during the injection from $B = 0.53\,\mathrm{T}$ to the peak field of $B = 8\,\mathrm{T}$.

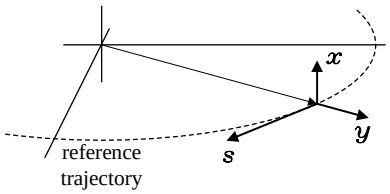

Figure 3.1: Moving reference coordinate system.

The coordinate system in Figure 3.1 represents a moving frame, it follows a reference particle around the design orbit. The coordinate axes x and y denote the horizontal and vertical planes, whereas small deviations from the reference orbit in s are denoted longitudinal direction.

The motion of particles requires a transverse focusing force to keep the trajectories of many particles close to the ideal orbit. With a Taylor expansion of the B-field in (3.3) such that

$$B_y(x) = B_{y0} + \frac{dB_y}{dx}x + \frac{1}{2!}\frac{d^2B_y}{dx^2}x^2 + \frac{1}{3!}\frac{d^3B_y}{dx^3}x^3 \ \ldots \tag{3.4}$$

then each term of the magnetic rigidity can be assigned to a local bending curvature as a function of transverse position:

$$\frac{q}{p}B_y(x) = \frac{1}{\rho} + kx + \frac{1}{2!}mx^2 + \frac{1}{3!}ox^3 + \ \ldots \tag{3.5}$$

The first term in (3.4) has a uniform field along the transverse coordinate, equivalent to a constant bending radius ρ of the particle trajectory in (3.5). This field is generated by a magnet with two poles, hence the generating magnet is called *dipole*.

The second term represents a restoring force on a particle trajectory. Since it depends linearly on the deviation from the design orbit, the resulting force is proportional to the displacement x. The sign of the normalised field gradient k determines whether the effect is focusing or defocusing. A magnet with four poles (*quadruploe*) that is tilted by $\pi/4$ along the longitudinal axis generates the corresponding linear field pattern. The arrangement of the magnetic poles implies that a quadrupole has the opposite focusing property in the orthogonal plane. For example, if the magnet is focusing in the horizontal plane then it has a defocusing effect in the vertical plane.

To continue the multipoles expansion, which corresponds to the terms in the Taylor series (3.4), a *sextupole* produces a quadratic gradient field, *octupoles* have a cubic field function of the position, and so on. These higher order terms in (3.5) are characterised by normalised gradients m, o, and act as non-linear forces onto a transverse particle displacement. Here, sextupoles are used to control chromatic effects, called *chromaticity* (see below), while octupoles compensate for fringe field errors or other higher order geometric aberrations.

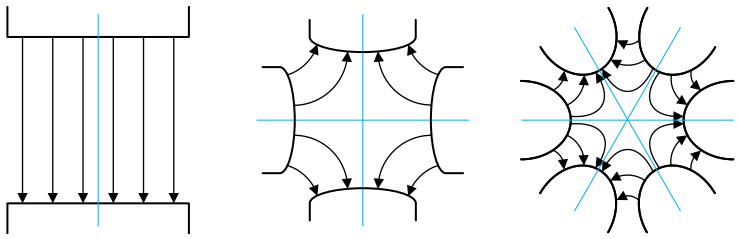

Figure 3.2: Different magnet types, from left to right: dipole, quadrupole, sextupole.

Particle accelerator physicists utilize the different types of magnets outlined in Figure 3.2 to design the guidance field of the moving charges in the accelerator. The pattern of the sequentially arranged magnets is refereed to as the *lattice* or simply as *optics*, since the magnets modify the particle beams in a similar way to how optical lenses affect rays of light.

As stated in (3.1), the force originating from the electric field accelerates in the same direction as the electric field component. Figure 3.3 outlines two dedicated applications

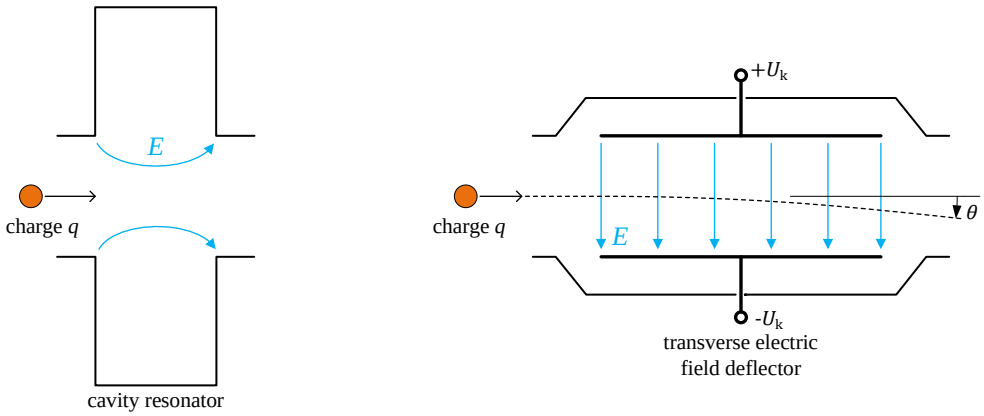

(a) Longitudinal acceleration in cavity structures.

(b) Transverse acceleration in a transverse deflectors.

Figure 3.3: Principle applications of external electric fields in particle accelerators.

that utilize the electric field in particle accelerators: resonant cavities and transverse electric field deflectors.

Resonant structures like cavities are commonly used to generate the longitudinal electric field component to accelerate the particles. Thereby, the voltage experienced by a particle over one turn simply is the integrated electric field around the accelerator circumference,

$$\Delta V = -\int E_s ds. \tag{3.6}$$

The RF cavities make the largest contribution to this voltage, but other effects also occur, which are summarized in Section 3.4.

In general, the voltage in a cavity resonator oscillates at a precisely controlled frequency, known as the radio or RF frequency f_{RF}, which is an integer multiple (also known as the harmonic number) h of the revolution frequency f_{REV}, such that

$$f_{RF} = h f_{REV}. \tag{3.7}$$

Here the revolution frequency follows as the reciprocal of the time of flight T_{REV} of a particle with speed v, for a complete revolution around an accelerator with circumference C,

$$T_{REV} = \frac{1}{f_{REV}} = \frac{C}{v}. \tag{3.8}$$

With the voltage in the cavity modulated,

$$V_{cav}(t) = V_0 \sin(2\pi f_{RF} t), \tag{3.9}$$

the resulting RF field creates islands of stable longitudinal oscillations, as illustrated in Figure 3.4 [72].

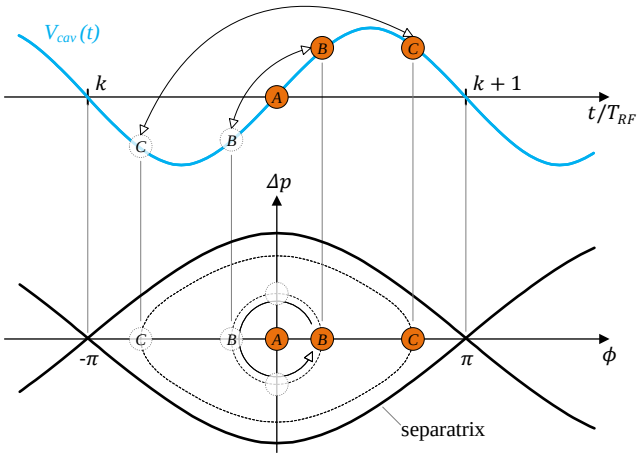

Figure 3.4: Longitudinal particle motion in a stationary RF bucket

Let's take the example of particle *A* crossing the RF cavity at exactly the time when $V_{cav} = 0$, i.e. there is no voltage in the cavity. Particle *A* therefore experiences no accelerating voltage. Assuming that the initial momentum does not change when the particle is not in the cavity, then after every revolution in the machine this particle will continue to arrive at exactly the same moment where $V_{cav} = 0$. Such a (hypothetical) particle does not oscillate in longitudinal direction, it has a reference momentum p_0 and always passes through the cavity with the *synchronous phase* denoted as ϕ_s.

On the other hand, particle *B* which lags behind particle *A*, experiences a positive voltage as it passes through the cavity, and therefore is accelerated. The additional energy speeds up the particle over several turns until both particles *A* and *B* arrive in the cavity at the same time. But their energy is now different, as can be seen in the longitudinal phase space in Figure 3.4 (bottom plot). Due to the higher energy, particle *B* now overtakes particle *A*, which means that after several turns there is a negative voltage in the cavity each time *B* passes. Eventually the particle slows down and the process repeats itself with particle *B* falling back due to its lower energy compared to particle A - it oscillates in longitudinal direction at the synchrotron frequency f_s.

More distant particles such as C, which only enter the cavity at or after the peak voltage V_0 has been reached, are still accelerated, but their oscillation patterns are no longer described by a simple harmonic motion. The limit of stability is called the /emph(separatrix). It forms the so called *RF bucket*. Without external perturbations the particles inside these buckets perform stable oscillations, so-called *synchrotron oscillations*; they are *captured* by the RF field, so to speak. These captured particles form a so-called *bunch*, the maximum temporal extend of which is defined by the RF period

$$T_{RF} = \frac{1}{f_{REV}}. \tag{3.10}$$

According to (3.7), there are h identical buckets distributed over the entire circumference in a machine at any time. Not all buckets necessarily have to be filled. The filling of buckets with particles is defined by a predetermined *filling pattern* which varies depending on the type of particles and intended use.

As sketched in Figure 3.3 (b), the second application of the electric field to accelerate particles is transverse deflection, commonly used to precisely influence the direction of motion of a particle — this process is generally known as *kick*. The simplified model presented can be viewed as a capacitor with parallel plates of mechanical length L_k and distance d_k apart. Both plates are charged with a voltage U_k, resulting in a transverse electric field strength in between of

$$E = \frac{U_\mathrm{k}}{d_k}. \tag{3.11}$$

Assuming a static deflector voltage, then the obtained deflection kick angle θ_kick is determined by comparing the longitudinal momentum p of the particle with the perpendicular momentum generated by the transverse electric field,

$$\tan\left(\theta_\mathrm{kick}\right) = \frac{p_\perp}{p} = \frac{EL_k}{v}. \tag{3.12}$$

As can be seen from equations (3.11) and (3.12), longer kicker structures as well as reduced spacing increase the deflection angle. On the other hand, increased particle momentum proportionally reduces deflection capacity — a particle beam becomes more rigid with higher momentum, an effect that can be compensated for by proportionally increasing the deflection voltage.

The illustration in Figure 3.4 shows the case of a stationary RF bucket with $\phi_s = 0$. In this configuration, the B-field is also constant and bunches are stored in the bucket for a certain time.

This situation is particularly useful once a machine has reached the end of acceleration, to *transfer* bunches to the next larger synchrotron. To achieve this, the accelerators concerned are brought to the same energy level and one ore more bunches are then *extracted* by the smaller machine with a slow or fast extraction mechanism into a *transfer line*, which transports them to the receiving machine [71]. In order to *inject* these into empty RF buckets without disturbing the already circulating beam, fast injection kickers are required.

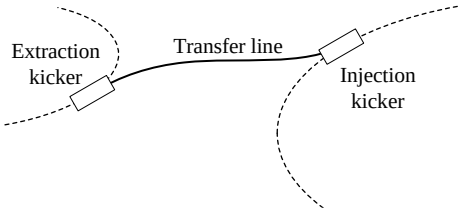

Figure 3.5: Beam transfer between synchrotrons.

In the transfer process of particle accelerators, several imperfections can arise that affect the overall beam quality. Variations in extraction and injection kicker timings can lead to substantial transverse oscillations, disrupting the intended beam trajectory. Additionally, precise steering in the transfer line is crucial to ensure a smooth transition of the beam from one accelerator to another. Orbit bumps, which are implemented during the transfer process, can inadvertently cause oscillations in the receiving machine, further complicating the injection dynamics.

3.2 Single particle dynamics

The restoring forces of the lattice described in the previous section repel a particle that deviates from the designed, i.e. equilibrium orbit, to oscillate around it [73].

Since the oscillation amplitude is generally considered to be small with respect to the reference orbit, a linearized *betatron motion* model can be obtained by neglecting higher-order non-linear fields in (3.4) within an accelerator structure. With this assumption, the lattice consists of only two types of magnets: strong dipole magnets, which bend

the trajectory for a complete turn, and quadrupole magnets to linearly focus displaced particles (see Figure 3.6). The resulting linear betatron motion is described in the reference frame with a second-order differential equation of motion

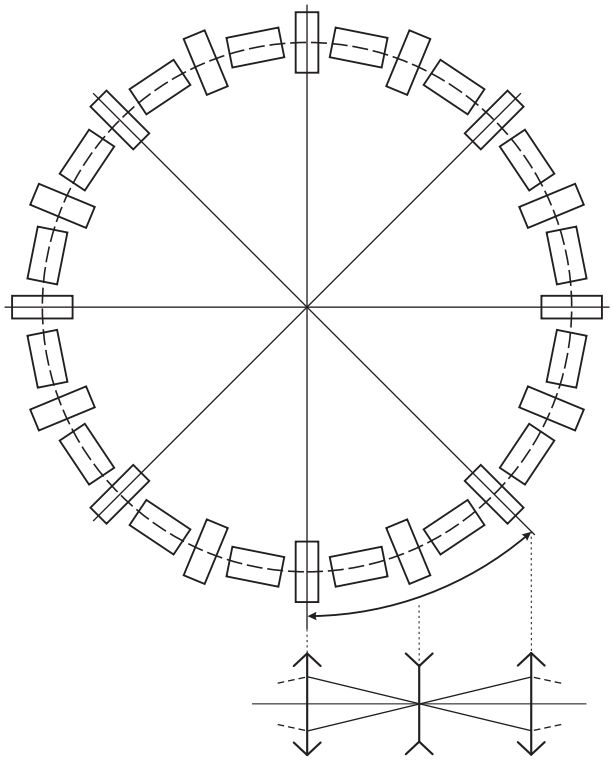

Figure 3.6: A basic lattice consisting of dipole magnets and focusing/defocusing quadrupole magnets that built a FODO cell.

$$x'' + K_x(s)\, x = 0, \tag{3.13}$$

where $K_x(s)$ is the magnetic focusing function in the horizontal plane. A general solution for (3.13) is readily available through the Mathieu-Hill Equation of charged particle trajectories in a magnetic guidance field,

$$x(s) = A\sqrt{\beta(s)}\cos\left(\psi(s) + \phi\right). \tag{3.14}$$

This equation is commonly referred to as *betatron oscillation* and describes the solution of a particle's trajectory in one plane. The two constants of integration A and ϕ are determined by initial conditions. The amplitude function, or simply β-function, is fully characterised by the magnetic guidance fields of the lattice and is periodic around the circumference of the machine, C, such that

$$\beta(s + C) = \beta(s)\,. \tag{3.15}$$

The phase advance $\psi(s)$ in (3.14) between any two points with longitudinal coordinates s_1 and s_2 in the lattice results from the integral over the inverse β-function

$$\psi_{21} = \int_{s_1}^{s_2} \frac{d\sigma}{\beta(\sigma)}. \tag{3.16}$$

The above equation states that for a known β-function of the accelerator, the phase advance between any two points around the machine circumference can be directly expressed using (3.16).

Within one machine revolution, each particle exhibits Q oscillations, commonly known as machine *tune*. The tune is a dimensionless unit, which is generally > 1 for strong focusing circular machines. For example, for the LHC, the horizontal tune is given as $\mathrm{Q}_h = 64.28$, and the vertical plane $\mathrm{Q}_h = 59.32$ [4]. For stability reasons, the tune has to be a non-integer number, expressed as

$$\mathrm{Q} = \mathrm{Q}_i + \mathrm{Q}_f\ , \tag{3.17}$$

where Q_f is the fractional tune and Q_i is an integer. Consequently, a single particle has a phase advance of

$$\psi_C = \oint_C \frac{d\sigma}{\beta\,(\sigma)} = 2\pi\mathrm{Q} \equiv 2\pi\mathrm{Q}_f \tag{3.18}$$

after one full machine revolution.

Observing the oscillation amplitude x of a single particle at a fixed azimuth position s_0 over subsequent turns and plotting it against its first derivative $x' = dx/ds$ gives the *transverse phase space* plot (see Figure 3.7). The shape of the resulting ellipse is fully defined by the β-function (its property follows from the accelerator design), and the area of the ellipse – also called *emittance* – follows from the particle's initial conditions.

Liouville showed that for linear optics the area in phase space, i.e. the area of the ellipse, remains constant as a particle travels around the accelerator and that it is completely defined by the lattice properties of the magnetic guidance field. Figure 3.8 sketches the phase space plot of a single particle as observed at different longitudinal coordinates.

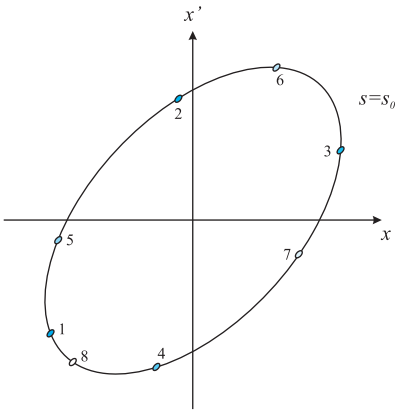

Figure 3.7: Transverse phase space plot

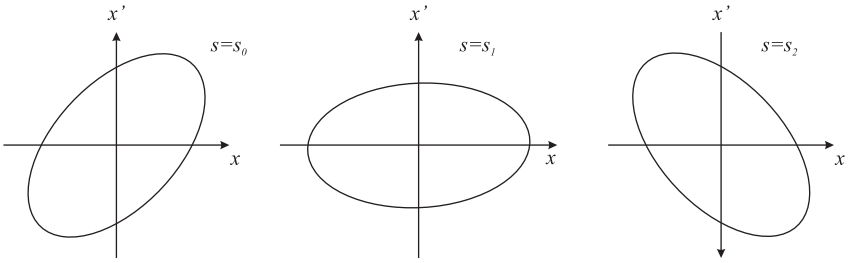

Figure 3.8: Phase space ellipses for different longitudinal coordinates.

3.3 Beam of bunched particles

The lattice is designed for a particle with reference momentum p_0 which is the nominal momentum of the synchronous particle following the reference orbit (see also Section 3.1). Any particle with momentum p slightly deviating from p_0,

$$\Delta p = p - p_0, \tag{3.19}$$

undergoes a different deflection in the lattice and therefore follows a different closed orbit. The restoring force for the momentum deviation in (3.19) is provided by the RF fields in longitudinal direction applied through cavity structures (see Section 3.1). The movement in the longitudinal plane is defined around the synchronous particle (with respect to the cavity voltage), and it is much slower than the betatron oscillations.

An important parameter of every circular accelerator is called *chromaticiy* ξ. It is generated by the lattice itself,

$$\xi = \frac{1}{4\pi} \oint K(s)\,\beta(s)\; ds, \tag{3.20}$$

where the main contribution comes from the strong focusing gradients in the magnetic guidance field. Particles captured in the RF bucket experience a tune spread $\Delta \mathrm{Q}/\mathrm{Q}$ due to momentum spread, a consequence of the quadrupole focusing strength dependence, which is inversely proportional to momentum (see Equations (3.4) and (3.5)). A small spread in momentum $\Delta p/p$ causes a spread in tune proportional to chromaticity,

$$\frac{\Delta \mathrm{Q}}{\mathrm{Q}} = \xi \frac{\Delta p}{p}. \tag{3.21}$$

In circular accelerators, the chromaticity is usually overcompensated, namely ξ is carefully adjusted to always be slightly positive. This is to avoid negative chromaticity values that could cause instabilities known as head-tail instability.

3.4 Collective effects

In addition to the external magnetic guidance field of the magnets and the electric acceleration fields of the RF cavities, each charged particle creates its own electromagnetic (EM) fields. These self-induced EM fields affect other particles due to their interaction with the surrounding environment, called the *space charge effect*. This effect has an increased importance when it comes to generating high-intensity beams (threshold behaviour).

A distinction is made between *coherent* and *incoherent* transverse collective effects. In the first case, the beam *centroid* (the weighted average of the positions of all particles in the beam) is affected, observable as transverse motion: betatron tune shift, possibly becoming unstable as the number of particles increases above a certain threshold (single/multi bunch, strong head-tail);

Incoherent collective effects are not visible by beam position monitors because the beam centroid is not affected, but they result in emittance growth, halo/tail formation, slow particle losses, reflecting poor beam lifetime.

Another classification is made on single bunch and multi bunch effects:

1. Single bunch effects

- space charge [74]
- resistive wall instability [75, 76]

2. multi-bunch effects [77]

- coupled bunch modes [78, 79], betatron oscillations are coupled through magnetic fields
- mode structure
- Machine impedance/Wake fields [80–85]
- Instabilities [86, 87]
- Landau damping [88, 89]
- Radiation damping [90]

These effects require to study a system of many particles, with kinetic models based on distribution functions $\psi(x, y, s, x', y', \delta)$:

$$N = \int_{-\infty}^{\infty} \psi(x, y, s, x', y', \delta) dx dx' dy dy' ds d\delta. \tag{3.22}$$

The mean position of an ensemble of N particles follows from the particle distribution by evaluating

$$< x >= \frac{1}{N} \int_{-\infty}^{\infty} x\psi(x, y, s, x', y', \delta) dx dx' dy dy' ds d\delta. \tag{3.23}$$

Equivalently, the standard deviation from the distribution is given as,

$$\sigma_x^2 = \frac{1}{N} \int_{-\infty}^{\infty} (x - < x >)^2 \psi(x, y, s, x', y', \delta) dx dx' dy dy' ds d\delta. \tag{3.24}$$

Longitudinal collective effects are: energy loss, synchronous phase shift, bunch lengthening, instabilities (negative mass instability, single or coupled bunch instabilities, microwave instability)

Chapter 4

Methods

To investigate the methods and techniques necessary to achieve Objective #1, a comprehensive system model must first be created [12, 91]. This chapter begins by breaking down the TFB into individual blocks, for which we develop detailed mathematical models. These models will be analyzed to determine their contributions to the overall TFB function, assess key parameters, identify which TFB blocks can be simplified or omitted for analysis, and define the critical blocks and parameters needed to meet the objective.

Building upon this foundational modeling, key system parameters associated with the TFB will be identified and elaborated upon within the context of controls engineering, aligning with Objective #1.

Additionally, this chapter will discuss methods for reconstructing the transverse phase space, introducing new algorithms for both spatial and temporal analysis. These methods will provide valuable insights into the system's dynamics. The exploration of transverse phase space reconstruction represents a significant contribution of this thesis, as it is essential for fulfilling Objectives #2 and #3, thereby enhancing the understanding of the field.

Subsequently, the focus will shift to the extraction of TFB parameters, including gain, phase, and delay, alongside accelerator parameters such as bunch-by-bunch tune and damping time. This extraction is made possible by the data obtained from the reconstructed transverse phase space. The sensitivity of the algorithm to noise will also be evaluated as part of Objective #1, outlining further requirements for the data quality of the available observables from the TFB.

Finally, this chapter will conclude with an assessment of the computational complexity associated with the methodologies, in line with Objective #4.

4.1 System modeling

The aim is to obtain a simplified representation of the overall TFB system and all of its components. The simplified model makes it possible to derive stability constraints and to identify a controller that ensures that the dynamic system and the overall system function in a stable manner.

Figure 4.1 illustrates the situation in a concise block diagram. Considering the use of an embedded digital controller suggests the introduction of two domains, one of which is the continuous-time domain covering analogue systems and the beam model in the Laplace domain. On the other hand, all operations performed digitally are best represented in the z-domain, or equivalently, the discrete-time domain. Transitions between domains are included in the sensor block and the actuator block, respectively.

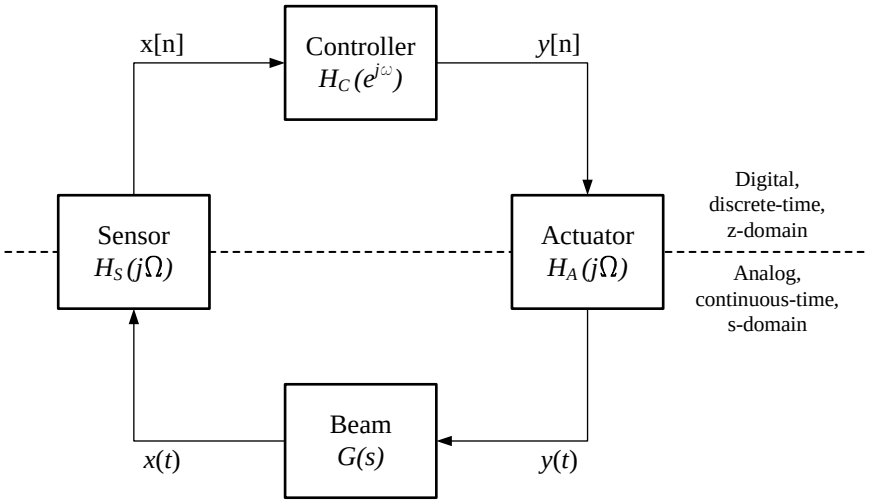

Figure 4.1: Feedback loop

The digital controller calculates the necessary control signal from the sensor input and feeds the actuator that manipulates the beam. Ideally, the sensor does not change the information that it collects. It exhibits a constant gain within the frequency band of interest, along with a constant signal delay that is independent of frequency. The transverse beam motions $x(t)$ are monitored in such a way that the sensor's output represents the position of each individual bunch, and is readily converted into a discrete-time sequence $x[n]$. This data stream is fed into the digital controller to calculate a correction signal $y[n]$. The actuator, in turn, converts the information into a continuous-

time deflection signal $y(t)$, which acts back on the beam. Just like the ideal sensor, the ideal actuator also has a constant gain and a linear phase over the desired frequency range.

In the following it is shown that the beam model $G(s)$ can also be modeled as a discrete-time system $G(z)$, a notation best suited to signal processing techniques. This is based on the assumption that the sensor and the actuator can be simplified to a pure continues-to-discrete and discrete-to-continuous converter – this will be addressed in the following sections.

4.1.1 Beam representation in z-domain

Although the beam is essentially an ensemble of discrete particles, its 'macroscopic properties'—or directly observable phenomena—are best described in the continuous-time domain. However, the beam moves close to the speed of light, while observations, for example with beam position monitors, are stationary (ignoring ground movements). Those position monitors basically 'sample' the passing beam, and thus generate a discrete-time representation. Therefore, the parameters of interest are optimally described using the concept of discrete-time signal processing.

Starting with the equation of motion from equation (3.14),

$$x(s) = A\sqrt{\beta(s)}\cos\left(\psi(s) + \phi\right). \tag{4.1}$$

Here $\beta(s)$ is the optics β-function, a location-dependent parameter that accounts for the magnetic guidance field at a longitudinal coordinate s. The magnetic field also defines the oscillation phase, $\psi(s)$. Initial conditions are given by the peak oscillation amplitude A and an initial phase ϕ. In the following notations a dependence on the longitudinal coordinate s is omitted for simplicity.

The first derivative of (4.1) with respect to the longitudinal coordinate follows directly as

$$\frac{dx}{ds} \equiv x'(s) = -A\frac{1}{\sqrt{\beta}}\left[\alpha\cos\left(\psi + \phi\right) + \sin\left(\psi + \phi\right)\right]. \tag{4.2}$$

Here x' is the slope of the particle trajectory along the longitudinal direction. The parameter α is another Twiss optics function describing the magnetic lattice.

The equations (4.1) and (4.2) describe the particle motion through the magnetic guidance field. Rewriting them as a vector, $\tilde{\boldsymbol{x}}$, one gets,

$$\tilde{\boldsymbol{x}} = \begin{pmatrix} x \\ x' \end{pmatrix}. \tag{4.3}$$

The dependency of the Twiss parameters can be eliminated by applying a linear transformation. The linear operator, denoted as Λ, is a function of the azimuthal location s that maps the vector $\tilde{\boldsymbol{x}}$ to the state vector $\boldsymbol{x}$:

$$\tilde{\boldsymbol{x}} \overset{\Lambda(s)}{\rightarrow} \boldsymbol{x}, \tag{4.4}$$

This mapping provides a representation of a state vector that is independent of local amplitude functions. With the operator of the form

$$\Lambda(s) = \frac{1}{\sqrt{\beta}} \begin{pmatrix} 1 & 0 \\ -\alpha & -1 \end{pmatrix}, \tag{4.5}$$

the state vector therefore simplifies to

$$\boldsymbol{x} = A \begin{pmatrix} \cos(\psi + \phi) \\ \sin(\psi + \phi) \end{pmatrix}. \tag{4.6}$$

Considering the trigonometric form of (4.6), this suggests introducing a complex notation for representing $\boldsymbol{x}$ in two-dimensional space. Equivalently to,

$$x = A(\cos\psi + j\sin\psi) = Ae^{j\psi}, \tag{4.7}$$

where the initial conditions of the transverse oscillations, the oscillation amplitude A and the initial phase ϕ, have been combined in a complex phase vector (phasor[1]),

$$A = |A| e^{j\phi}. \tag{4.8}$$

If the complex oscillation amplitude at a location s_1 is known, i.e.

$$x_1 = Ae^{j\psi_1}, \tag{4.9}$$

then the oscillation condition at any other point s_2 follows from

[1] Throughout this book a phasor shall refer to a complex constant, i.e. $C = |C| e^{j\phi}$.

$$x_2 = Ae^{j\psi_2} = Ae^{j(\psi_1+\Phi_{21})}. \tag{4.10}$$

Here the machine-dependent phase advance Φ_{21} between the two locations, s_1 and s_2 has already been found in Chapter 3. It is given by the definite integral

$$\Phi_{21} = \int_{s_1}^{s_2} \frac{d\sigma}{\beta(\sigma)}, \tag{4.11}$$

which rewrites with (3.16) to the difference in phase advances

$$\Phi_{21} = \psi(s_2) - \psi(s_1)\,. \tag{4.12}$$

The values for the phase advances can be obtained directly from optics simulations or extracted from dedicated measurements.

Since a particle exhibits an exact number of Q oscillations during a complete turn, it follows from (3.18) for the phase advance over one turn,

$$\Phi_{21} = 2\pi\mathrm{Q}. \tag{4.13}$$

Inserting (4.13) into (4.10) and including the constant phase value ψ_1 in the initial phase leads to a representation for the state vector and the n-th turn,

$$x[n] = Ae^{j2\pi\mathrm{Q}n} \qquad n \geq 0. \tag{4.14}$$

The previous equation describes a discrete-time complex exponential sequence. It represents the sampled transverse beam oscillations observed at a single location and for every turn.

Since the absolute value of the complex exponential function in (4.14) is unity, the sequence is stable in magnitude, and its initial oscillation amplitude $|A|$ is preserved (see Figure 4.2).

A more general form of this sequence is described in [92, Chapter x, Equation(y.z)] as

$$x[n] = A\alpha^n u[n]\,, \tag{4.15}$$

where A is a phasor (see (4.8)) and with a complex base, α,

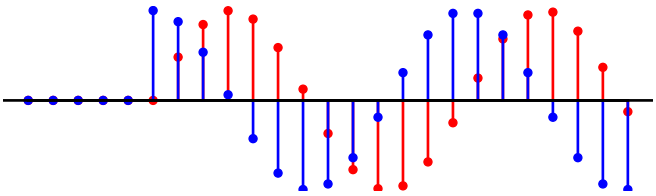

Figure 4.2: A transverse displacement (blue) converts into slope (red) with a phase lag of $\pi/2$.

$$\alpha = |\alpha|\, e^{j\omega_0}. \tag{4.16}$$

In (4.15) the unit step sequence $u[n]$ follows from

$$u[n] = \begin{cases} 1, & n \geq 0 \\ 0, & n < 0 \end{cases} \tag{4.17}$$

to take into account that no oscillations exist for $n < 0$.

The equivalent first-order difference equation of (4.15) is given by the recursion formula

$$x[n] = \alpha x[n-1] \qquad n > 0. \tag{4.18}$$

Introducing the z-transform [92], defined by the $\mathcal{Z}\{\cdot\}$-operator[1],

$$\mathcal{Z}\{x[n]\} = \sum_{n=-\infty}^{\infty} x[n]\, z^{-n} = X(z)\,. \tag{4.19}$$

and applying it to (4.15) yields

$$X(z) = \mathcal{Z}\{x[n]\} = A \sum_{n=0}^{\infty} |\alpha|^n\, e^{j\omega_0 n} z^{-n}. \tag{4.20}$$

The preceding equation requires the definition of a region of convergence (ROC) for which the sum is finite, i.e. the sequence is absolute summable. The necessary condition is therefore

[1] Here the bilateral transform has been chosen, which eventually leads to the unilateral z-transform when the signals are causal.

$$\sum_{n=0}^{\infty} \left|\alpha z^{-1}\right|^n < \infty. \tag{4.21}$$

This inequality is only fulfilled for values of $|z| > |\alpha|$. If one restricts the evaluation of (4.20) to the region of convergence, it follows with the general solution of a power series that the infinite sum can be expressed in closed form as

$$X(z) = A\frac{1}{1-\alpha z^{-1}} \qquad |z| > |\alpha|\,. \tag{4.22}$$

The properties of this remarkable compact equation will be explored in more detail below. The rational function has a single pole at $z = \alpha$ (see Figure 4.3), which corresponds to the fact that the time sequence is complex-valued: the convention used in (4.7) and (4.3) attributes the real part of $x[n]$ as the transverse displacement and the imaginary part as the slope.

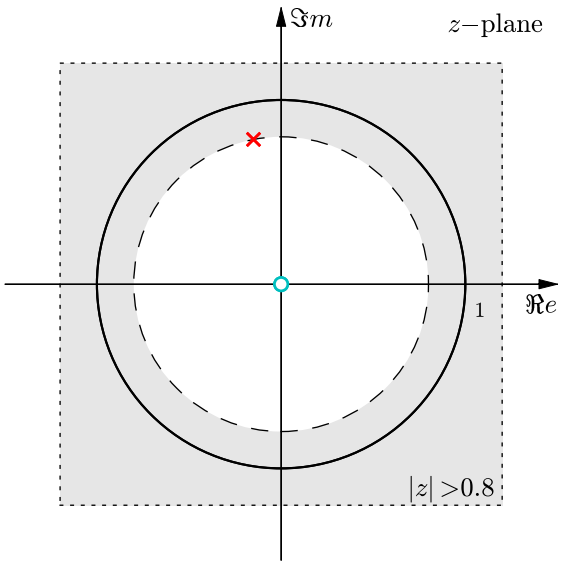

Figure 4.3: Pole-zero plot and ROC for (4.22) in the complex z-plane. The function has a single pole, denoted by '$\times$', and a zero at the origin, denoted by '$\circ$'. The dotted circle represents the unit circle, $z = e^{j\omega}$.

The amplitude value A in (4.22) is a linear scaling factor, while α characterizes the behaviour of the oscillation. The value of $|A|$ defines the magnitude of the oscillation amplitude for $n = 0$. The complex factor $e^{j\phi}$ determines the initial ratio between displacement versus slope. For example, a phase value of $\phi = 0$ starts the oscillations with maximum displacement. On the other hand, if the angle is equal to $\phi = \pi/2$, then the trajectory has no offset, but is maximally inclined.

Since $|\alpha|^n$ in (4.20) is an exponential sequence, it is the base value $|\alpha|$ that defines the resulting sequence. That is, if $|\alpha| > 1$ then the sequence values increase as n increases. If $0 < |\alpha| < 1$, then the sequence values decrease with increasing n. The oscillation remains stable in the case $|\alpha| = 1$.

The oscillation frequency is determined by the argument of α, which is defined as ω_0 in (4.16). Analogously to (4.14), it is a complex exponential sequence that oscillates with frequency $\omega_0 = 2\pi Q$ as n increases.

The sequence $x[n]$ completely describes the transverse state for each sample n. The state variables x and x' thereby are represented by the real and imaginary parts. The beam propagates through the magnetic guidance field of the accelerator, which applies focusing forces to prevent the beam from diverging. This in turn causes an oscillation that continuously converts transverse displacement into slope and vice versa (i.e. the trajectories of a free-running undamped system are circles). The previous derivation showed that the single pole in the z-plane characterises a complex sequence $x[n]$. If the roots of the denominator in (4.22) consisted of a pair of conjugate complex poles, then the resulting sequence would be real-valued, i.e. the imaginary part would always be zero. However, the transverse position still oscillates which is obviously a non-physical behaviour.

Furthermore, transverse deflecting devices act solely on the slope of a particle's trajectory (trajectories must be continuous at all times; a stepwise displacement at an infinitesimal short longitudinal distance requires either infinite energy—or transverse teleportation). Accordingly, all manipulations that also represent a physical meaning must be made for the imaginary part only.

A note on the convention of the principal coordinate system (see Chapter 3, page 18), a positive displacement commutes into a negative slope (positive angular frequency in clockwise direction). However, by defining a linear mapping as in (4.5), the direction of rotation also changes. This leads to the conclusion that – for the signal processing part – a positive displacement commutes to a positive slope. This conforms to the general convention in signal processing and engineering that a positive angular frequency rotates in counter-clockwise direction.

With the above, and to get an input-output relationship for a simplified beam model, let us now revisit the rational function $X(z)$ in (4.22). It has a single complex-valued pole at $z = \alpha$, which corresponds to the fact that the sequence $x[n]$ is also complex-valued.

It represents the simplest form of an Infinite Impulse Response filter (IIR), as outlined in Figure 4.4. Thereby, the convention used for Eq. (4.3) attributes the real part of $x[n]$ as transverse displacement, $y = \Re\{x\}$, and the imaginary part as the trajectory's slope. Accordingly, in Figure 4.4 the beam position monitor (or pick-up) extracts transverse displacement as $y[n] = \Re\{x[n]\}$.

The action of a kicker only changes the particle's slope. Consequently, in Fig. 4.4 the real-valued input sequence $\theta[n]$ is first multiplied by the imaginary unit $j = \sqrt{-1}$ and subsequently added to the complex-valued sequence $x[n]$.

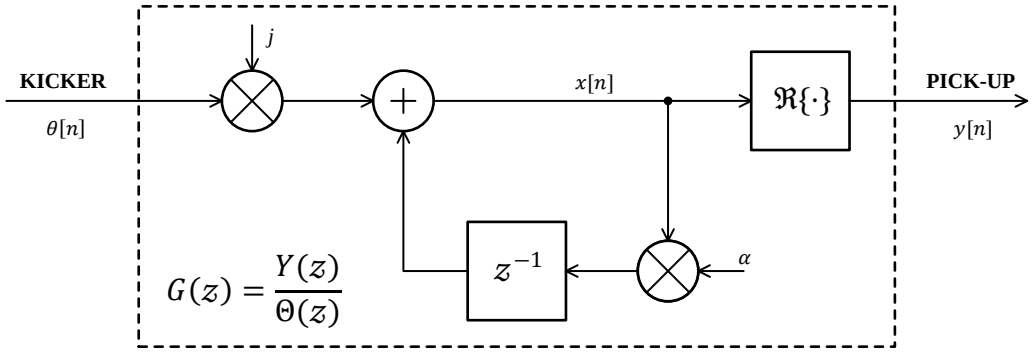

Figure 4.4: Simple beam model in z-domain.

The overall beam transfer function $G(z)$ can therefore be expressed as

$$G(z) = \frac{Y(z)}{\Theta(z)} = j\frac{1}{2}\left(\frac{1}{1-\alpha z^{-1}} - \frac{1}{1-\alpha^* z^{-1}}\right). \tag{4.23}$$

Here, α and α^* are the two conjugate complex poles of $G(z)$. It is worth noting that the second pole seen at the output, $Y(z) = G(z)X(z)$, is the result of the pick-up and its ability to only detect transverse position.

Equation (4.23) can be expanded and rewritten as

$$G(z) = \frac{r \sin\omega_0 \; z^{-1}}{1 - 2r\cos\omega_0 \; z^{-1} + r^2 \; z^{-2}}, \tag{4.24}$$

which makes it evident that due to the term z^{-1} in the numerator the output sequence is readily delayed by one sample, corresponding to the fact that a response to a transverse deflection at a particular longitudinal position is visible only after one turn.

In Eq. (4.24) the parameter r determines whether the oscillation at frequency ω_0 is stable ($|r| < 1$), steady ($|r| = 1$), or unstable ($|r| > 1$).

Taking into account an arbitrary phase shift ϕ_{PU} between the kicker and the pick-up, i.e. by extending the pick-up output such that $y[n] = \Re\{x[n] \cdot e^{j\phi_{PU}}\}$ one obtains more generally as beam transfer function

$$G(z, \phi_{PU}) = \frac{r \sin(\omega_0 + \phi_{PU})\, z^{-1} - r^2 \sin\phi_{PU}\, z^{-2}}{1 - 2r\cos\omega_0\, z^{-1} + r^2\, z^{-2}}. \tag{4.25}$$

As can be seen from Eq. (4.25) the introduction of a betatron phase advance ϕ_{PU} between pick-up and kicker has no impact on the position of the poles (the denominator is unaltered). In fact the required phase shift is established solely by an additional zero in the numerator, moving on the real axis of the z-plane as the phase angle changes.

4.1.2 Sensor model

This section is about identifying an analytical model for a transfer function between the transverse beam position as input to a sensor and the generated output. The transverse feedback systems of the LHC and the SPS are designed to measure bunch-by-bunch transverse displacements and damp oscillatory movements by means of fast electric field kickers. In order to detect the time-varying beam position the signals of individual bunches are processed in analog and digital [2, 93], generating one position reading per bunch per turn.

The design criterion for position signal processing is to have one position reading per bunch, that is, one sample spaced every T_s.

Independent treatment of bunches does require no cross-talk between adjacent bunches, a parameter known as inter-symbol interference (ISI). This restriction limits the continuous-time response of the sensor's analog system, $g(t)$, to zero at adjacent sampling points, i.e.,

$$g(kT_s) = 0; \quad \forall k \in \mathbb{R}^*. \tag{4.26}$$

If this condition is fulfilled then each bunch position can be treated independently by the feedback control as there is no coupling term added in the analog processing chain. At this point it is worth noting that the time limit on the impulse response, as required by (4.26), implies that the frequency response of the entire analog system must extend beyond the sample repetition rate $f_s = 1/T_s$.

In the following we analytically evaluate the performance of the sensor's beam position signal processing scheme for normalized longitudinal bunch profiles $\lambda(t)$ and transverse oscillation patterns $x(t)$ as test inputs (see Figure 4.5).

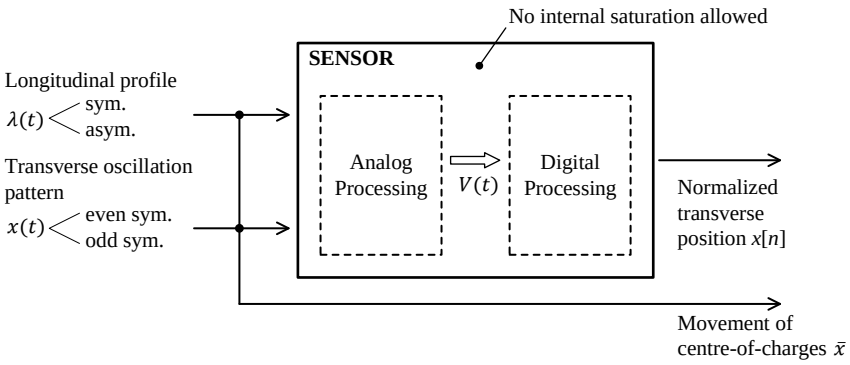

Figure 4.5: Evaluation of the TFB sensor performance.

For comparison, the true motion of the center-of-charges $\bar{x}$, given as

$$\bar{x} = \int x(t)\lambda(t)\ \mathrm{d}t, \tag{4.27}$$

for different excitation frequencies is tested against the digital representation of the beam normalized transverse position $x[n]$, as calculated by the LHC TFB beam position sensor.

The block diagram in Figure 4.6 outlines the signal processing chain of the LHC beam position measurement hardware. Beam-induced signals in a pickup go through an analog processing chain before being synchronously converted to digital in analog-to-digital-converters (ADC). An FPGA calculates a normalized position for each individual bunch from the data streams. This value is independent of the intensity per bunch or the longitudinal bunch shape.

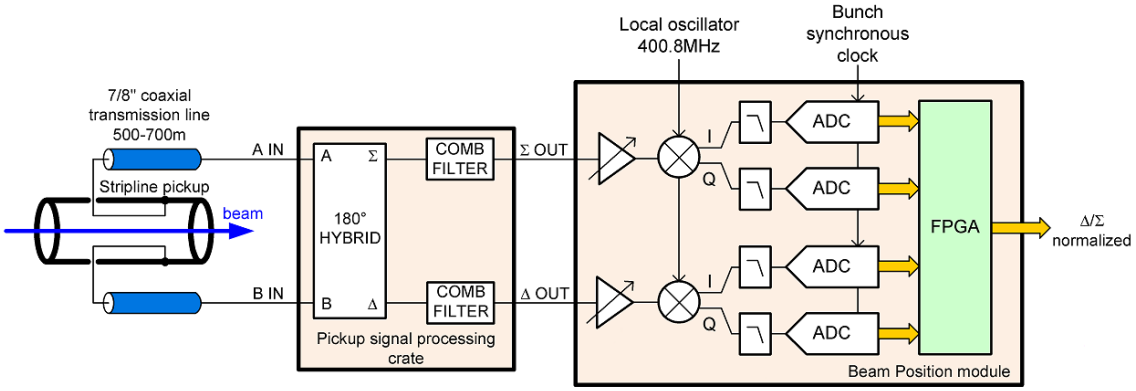

Figure 4.6: LHC beam position hardware signal processing scheme for Run I and Run II (taken from [2]).

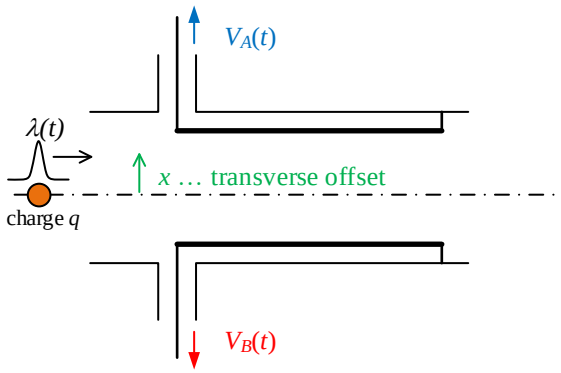

Figure 4.7: BPM coupler type pick-up with constant coupling.

Analog processing scheme

The electromagnetic field generated by a circulating bunch with normalized longitudinal profile $\lambda(t)$ and total charge q interfaces with a stripline type beam position monitor (BPM), thereby inducing a signal into two opposing electrodes (denoted A and B), whose amplitude depends on the transverse position $x(t)$ with respect to the vacuum chamber, and the pick-up geometry d_x (linear approximation for small amplitudes). See Figure 4.7 for a simplified graphical representation. The mechanical design of the stripline electrodes achieves a characteristic impedance of $50\,\Omega$ and no matching network is needed. The BPM output voltage follows from,

$$V_{A,B}(t) = Z_T \int_{-\infty}^{t} \left(1 \pm \frac{x(\tau)}{d_x}\right) \cdot q\lambda(\tau) \cdot h_{\mathrm{BPM}}(t-\tau)\,\mathrm{d}\tau, \tag{4.28}$$

with Z_T as the transfer impedance, and $h_{\mathrm{BPM}}(t)$ the impulse response of the BPM.

Since the BPM for the configuration of the LHC TFB is short-circuited at the downstream end of the electrode, the beam signal induced at the upstream end is eventually completely reflected. The reverse signal returns after the roundtrip time $T_0 = 2L/c$ with negative polarity at the upstream port. The resulting impulse response of the BPM (assuming $v = c$) therefore follows as

$$h_{\mathrm{BPM}}(t) = \delta\left(t + \frac{T_0}{2}\right) - \delta\left(t - \frac{T_0}{2}\right). \tag{4.29}$$

Here, $\delta(t)$ denotes the Dirac-Delta distribution which has the well-known properties, $\delta(t) = 0$ for $t \neq 0$, and $\int_t \delta(\tau)d\tau = 1$.

Note that (4.28) denotes a convolution integral of the longitudinal bunch profile with the pick-up response. The position information is encoded in the signal amplitude, which is AM modulated, with a strong common signal.

The peak voltages of the two electrodes can easily reach up to $400\,\mathrm{V}$ in the LHC for full intensity beam. This voltage is sufficient to transmit signals from the beam line in the underground tunnel to the surface electronics using low-loss coaxial transmission lines of identical length. The transmission line attenuates the raw pick-up signals to levels acceptable to the hybrid and adds a dispersion to the pulse response, represented by $h_{\mathrm{COAX}}(t)$.

The first element at the surface is a $180°$ hybrid. It combines the transmitted signals $\bar{V}_A$ and $\bar{V}_B$ into a sum signal Σ, which is common to both pickup electrodes, and it generates the difference or Δ-signal. The sum signal represents the longitudinal profile of the beam, i.e. the bunch shape and the number of charges, while the delta signal contains additional information about the transverse position.

Assuming an ideal hybrid, i.e. no crosstalk between the outputs, then

$$V_\Sigma(t) = \frac{1}{\sqrt{2}}\left[\bar{V}_A(t) + \bar{V}_B(t)\right], \tag{4.30}$$

$$V_\Delta(t) = \frac{1}{\sqrt{2}}\left[\bar{V}_A(t) - \bar{V}_B(t)\right]. \tag{4.31}$$

A special type of bandpass filter, called a comb filter, shapes both the sum and the delta signal in the time domain into a well-defined wavelet [2]. The filter response is designed for a time-limited rectangular window of less than $25\,\mathrm{ns}$, shorter than the nominal bunch spacing, to ensure no mixing between adjacent bunch signals. These filters have a center frequency of $400.8\,\mathrm{MHz}$, which corresponds to the LHC RF frequency.

The bandpass filter output (denoted with a tilde), applied for the Σ signal in (4.30) by inserting Eq. (4.28), results from

$$\tilde{V}_\Sigma(t) = q\lambda(t) * h_{\mathrm{PU}}(t), \tag{4.32}$$

where

$$h_{\mathrm{PU}}(t) = \sqrt{2} Z_T \cdot h_{\mathrm{BPM}}(t) * h_{\mathrm{COAX}}(t) * h_{\mathrm{BP}}(t). \tag{4.33}$$

Equation (4.33) represents the cascade or convolution (here and hereafter referred to with asterisk notation) of impulse responses in the time domain, including the beam transfer impedance, the signal gain by $\sqrt{2}$ in the hybrid, and passive linear elements that shape the response in time and frequency domain.

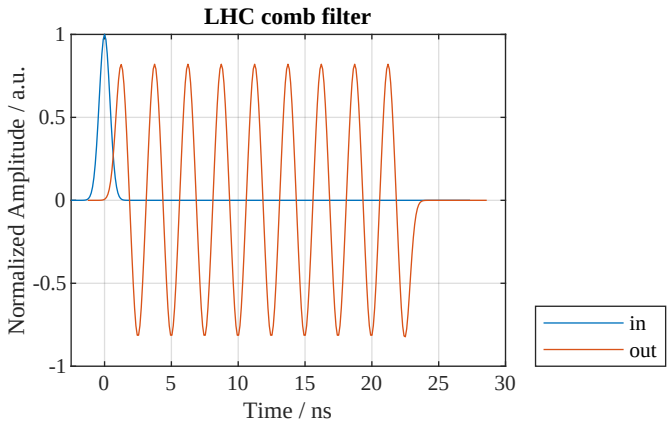

Figure 4.8: Bandpass filter response

Similarly, the Δ signal output follows from Eq. (4.31) in combination with Eq. (4.28) as,

$$\tilde{V}_{\Delta}(t) = \left(\frac{x(t)}{d_x} \cdot q\lambda(t) \right) * h_{\mathrm{PU}}(t). \tag{4.34}$$

These equations (4.32) and (4.34) describe the underlying formalism in the time domain, the effects of which are visible in the frequency domain. Namely, the convolution in the time domain leads to a multiplication in the frequency domain, or

$$\tilde{V}_{\Sigma}(j\omega) = q\Lambda(j\omega) \cdot H_{\mathrm{PU}}(j\omega). \tag{4.35}$$

On the other hand, multiplication in the time domain as within (4.34) leads to a convolution in frequency domain. Therefore,

$$\tilde{V}_{\Delta}(j\omega) = \left(\frac{X(j\omega)}{d_x} * q\Lambda(j\omega) \right) \cdot H_{\mathrm{PU}}(j\omega). \tag{4.36}$$

For the case of a sinusoidal excitation with $X(j\omega) = \delta(\pm\omega_x)$, the previous equation states that a transverse oscillation causes a shift in the spectrum of the longitudinal bunch profile to the carrier frequencies at $\pm\omega_x$,

$$\tilde{V}_{\Delta}(j\omega) = \frac{1}{d_x} q\Lambda\left[j(\omega \pm \omega_x)\right] \cdot H_{\mathrm{PU}}(j\omega). \tag{4.37}$$

As shown in Figure 4.6, the Beam Position Module uses a set of mixers to demodulate the bandpass filtered signals into in-phase and quadrature components (I/Q pairs for Δ and Σ). This is followed by optimized Gaussian low-pass filters, which suppress image frequencies and shape the system response to minimize output ripples.

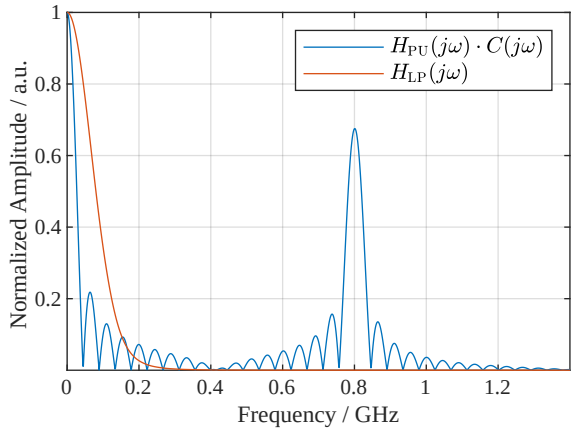

Figure 4.9: Frequency response of $h_{\mathrm{PU}}(t) \cdot c(t)$ and lowpass filter $h_{\mathrm{LP}}(t)$.

The baseband response of the in-phase component, which has even symmetry, is obtained by multiplying by $c(t) = \cos(\omega_{\mathrm{LO}} t)$. In contrast, the quadrature component, which has odd symmetry, is obtained by multiplying by $s(t) = \sin(\omega_{\mathrm{LO}} t)$.

Therefore, from (4.32) we get for the Σ-signal after low-pass filtering:

$$\begin{aligned} I_{\Sigma}(t) &= k_{\Sigma} \left[q\lambda(t) \cdot c(t) \right] * g(t), \\ Q_{\Sigma}(t) &= k_{\Sigma} \left[q\lambda(t) \cdot s(t) \right] * g(t), \end{aligned} \tag{4.38}$$

where signal level adjustments and other coefficients are combined into a single scalar, k_{Σ}, and with

$$g(t) = \left[h_{\mathrm{PU}}(t) \cdot c(t) \right] * h_{\mathrm{LP}}(t). \tag{4.39}$$

Equation (4.39) states that the response function of (4.33) is demodulated into baseband and then lowpass filtered by $h_{\mathrm{LP}}(t)$. A graphical representation of this relationship in frequency domain is shown in Figure 4.9.

At this point it is worth noting that the shape of the baseband response of (4.38) is completely defined by $g(t)$ and only its amplitude is a function of the demodulated longitudinal profile.

An assessment of the sensor response function $g(t)$ in both the time and frequency domains is presented in Figure 4.10.

Similarly, I/Q demodulation of the bandpass filtered Δ signal provided by (4.34)

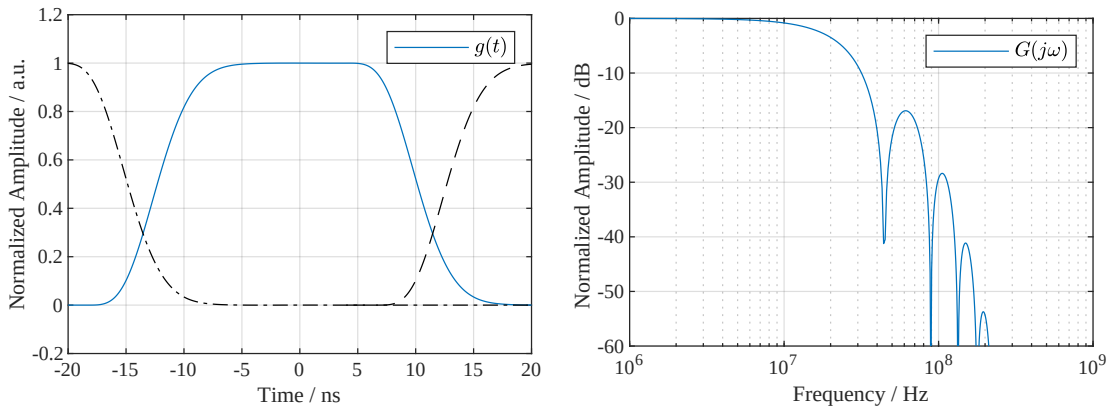

(a) Baseband impulse response $g(t)$.

(b) Baseband transmission response $G(j\omega)$.

Figure 4.10: Sensor response function. Left: time domain. Right: frequency domain.

gives the following:

$$\begin{aligned} I_\Delta(t) &= k_\Delta \left\{ \left(\frac{x(t)}{d_x} \cdot q\lambda(t) \right) \cdot c(t) \right\} * g(t), \\ Q_\Delta(t) &= k_\Delta \left\{ \left(\frac{x(t)}{d_x} \cdot q\lambda(t) \right) \cdot s(t) \right\} * g(t). \end{aligned} \tag{4.40}$$

Here the order of multiplication is important: (1) transverse position modulation $x(t)$, (2) demodulation with $c(t)$ or $s(t)$.

Similar to the baseband response defined in (4.38), the shape of the baseband response in (4.40) is determined solely by $g(t)$. However, in this case, the amplitude also depends on the excitation frequency and the longitudinal profile.

Digital position calculation

A total of twelve beam-synchronously clocked analogue to digital converters sample the I/Q pairs and provide a digitized sample per bunch and signal[93].

The normalized bunch position is given by taking the ratio of the Δ-signal to the Σ-signal, $\mathrm{X}_N = \Delta/\Sigma$, which is independent of the intensity per-bunch. A more elegant way was found by expanding the ratio mathematically with the conjugate complex Σ^*,

$$\mathrm{X}_N = \frac{\Delta}{\Sigma}\frac{\Sigma^*}{\Sigma^*} = \frac{\Delta \cdot \Sigma^*}{|\Sigma|^2}. \tag{4.41}$$

By introducing the two phasors, $\Delta = A \cdot e^{j\alpha}$ and $\Sigma = B \cdot e^{j\beta}$,

$$\begin{aligned} \Delta &= A\cos\alpha + jA\sin\alpha \doteq I_\Delta + jQ_\Delta, \\ \Sigma &= B\cos\beta + jB\sin\beta \doteq I_\Sigma + jQ_\Sigma, \end{aligned} \tag{4.42}$$

we rewrite (4.41) in I/Q components provided by the sampling,

$$\mathrm{X}_N = \frac{I_\Delta I_\Sigma + Q_\Delta Q_\Sigma}{{I_\Sigma}^2 + {Q_\Sigma}^2} + j\frac{Q_\Delta I_\Sigma - I_\Delta Q_\Sigma}{{I_\Sigma}^2 + {Q_\Sigma}^2}. \tag{4.43}$$

For perfect alignment of the two phasors (i.e. $\alpha - \beta = 0$), the first term maximizes in (4.43). Only the real part of X_N is used as position input in the TFB, while the imaginary part provides an indication of head-tail activities and asymmetries in the longitudinal bunch profile.

Simulation Model

Due to the sampling of the continuous-time signals, where only one value is selected, it can be shown that the convolutions in (4.38) and (4.40) can be simplified to definite integrals. Consequently, the described analytical model can be further refined into a more practical implementation that is essentially independent of hardware parameters:

1. The time-varying transverse position signal across a bunch and the longitudinal beam profile are multiplied by two fixed frequency signals in quadrature,

$$\begin{aligned} c(t) &= \cos\left(\omega_0 t\right), \\ s(t) &= \sin\left(\omega_0 t\right), \end{aligned} \tag{4.44}$$

   where $\omega_0/(2\pi) = 400.8\,\mathrm{MHz}$ for the case of the LHC TFB.

2. The longitudinal profile is demodulated to the baseband as

$$\begin{aligned} \hat{I}_\Sigma(t) &= \int c(t)\lambda(t)\,\mathrm{d}t, \\ \hat{Q}_\Sigma(t) &= \int s(t)\lambda(t)\,\mathrm{d}t. \end{aligned} \tag{4.45}$$

3. With the delta signal, the longitudinal profile is first modulated with the position signal and then demodulated into baseband, as indicated by

$$\begin{aligned} \hat{I}_\Delta(t) &= \int c(t)x(t)\lambda(t)\,\mathrm{d}t, \\ \hat{Q}_\Delta(t) &= \int s(t)x(t)\lambda(t)\,\mathrm{d}t. \end{aligned} \tag{4.46}$$

4. Finally, the normalization algorithm implemented in the LHC TFB follows from,

$$x_N = \frac{\hat{I}_\Delta \hat{I}_\Sigma + \hat{Q}_\Delta \hat{Q}_\Sigma}{\left(\hat{I}_\Sigma\right)^2 + \left(\hat{Q}_\Sigma\right)^2}. \tag{4.47}$$

Numerical Simulation

Figure 4.11(a) presents the numerical input of the bunch length simulation, based on the work by Salvant et al. (Ref. [94]. In this study, the first notch in the spectrum was observed at approximately $1.5\,\mathrm{GHz}$. This profile is modulated with an even-symmetric excitation up to $3\,\mathrm{GHz}$.

In Figure 4.11(b), the blue curve represents the result from (4.47), while the red curve indicates the true movement of the center-of-charges as described by (4.27). It is evident that the damper's sensitivity to symmetrical intra-bunch motion depends on the longitudinal beam spectrum. This sensitivity extends well beyond the highest betatron frequency of coupled bunch oscillations up to $20\,\mathrm{MHz}$, with the first notch appearing at around $1.9\,\mathrm{GHz}$ due to the demodulation process.

In Figure 4.11(c), we evaluate the imaginary part of (4.43) for odd-symmetrical excitation (green). In the anti-symmetric case, the normalization algorithm detects no oscillation amplitude (blue), which confirms that the center-of-charges is not moving and, therefore, that odd modes are not visible to the damper.

As a result of the analytical model described above, we derived a practical set of equations in (4.44)-(4.47) that characterize the sensitivity of the bunch-by-bunch sensors used in the LHC and SPS TFB to intra-bunch motion. Numerical simulations revealed that the current beam position signal processing actually detects even-symmetric intra-bunch movements beyond $20\,\mathrm{MHz}$, for which the TFB applies corrective measures in baseband (up to 20 MHz) through feedback control. However, if only one value is available per bunch, the information about the excitation frequency is lost. These equations should be used for particle tracking simulations to accurately model the actual behaviour of the bunch-by-bunch LHC and SPS TFB.

An important observation from equations (4.44)-(4.47) is that they not depend on hardware parameters, except for the demodulation frequency, provided the hardware has been properly commissioned. Additionally, the numerical simulations (see Figure 4.11(b)) indicate that the sensor's sensitivity corresponds to the true movement of the centre-of-charges up to the highest coupled bunch oscillation frequency. For the overall system

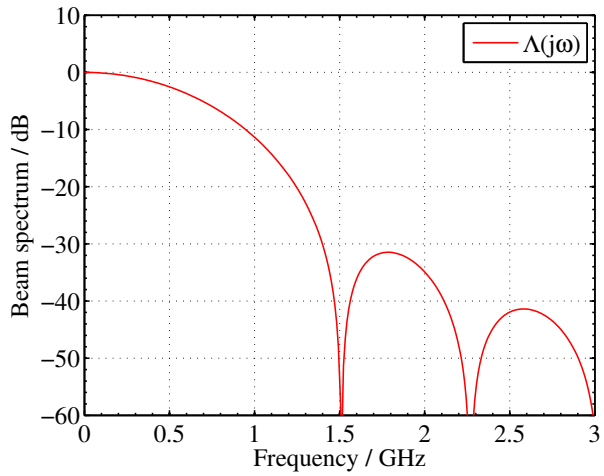

(a) Longitudinal profile $\lambda(f)$.

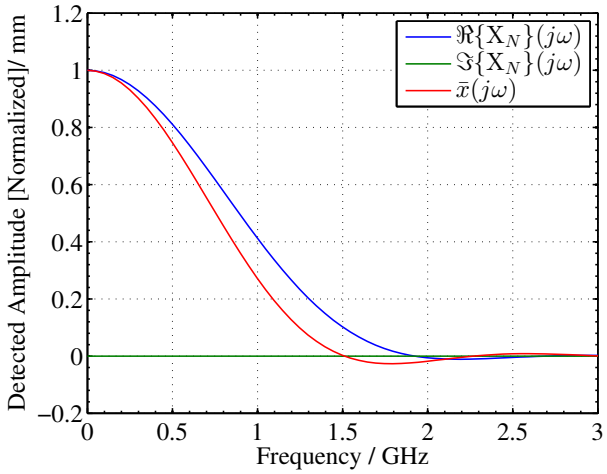

(b) Even-symmetric excitation.

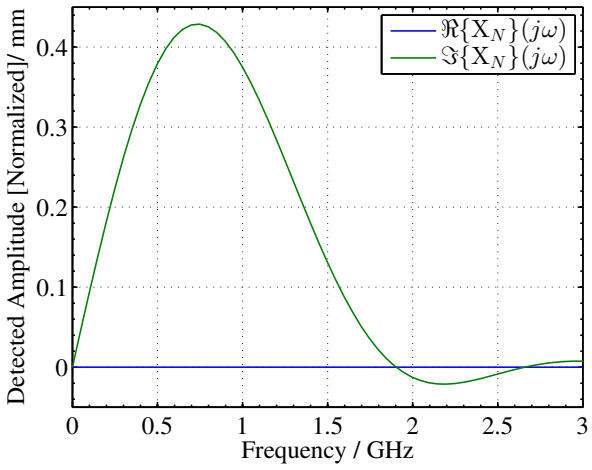

(c) Odd-symmetric excitation.

Figure 4.11: Numerical results obtained from simulation.

evaluation, this confirms the validity of our previous assumption and we can simplify the contribution of the sensor to the overall system transfer function:

$$H_{\mathrm{S}}(j\Omega) \equiv H_{\mathrm{S}}(z) = 1. \tag{4.48}$$

4.1.3 Actuator model

In this section, we simplify the actuator model, demonstrating that it can be regarded as transparent in the overall system evaluation, with no influence on the assessment of the closed-loop dynamics.

The actuator converts the output sequence $y[n]$, produced by the controller, into the deflector signal $y(t)$, which is utilized to manipulate the transverse beam momentum. The signal chain, beginning at at the output of the embedded controller, is illustrated in Figure 4.12.

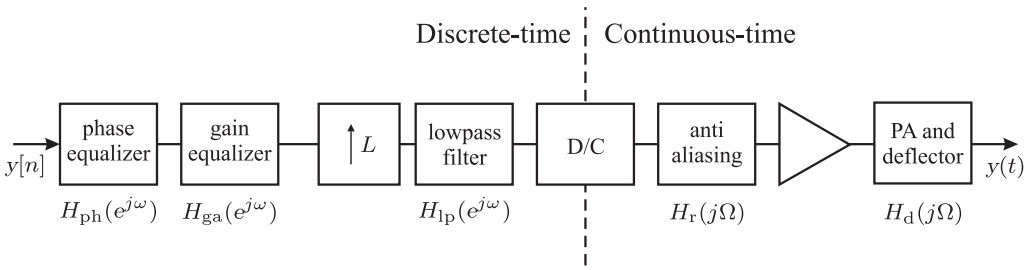

Figure 4.12: Feedback actuator

To achieve the desired performance, two digitally implemented FIR filters, designated as $H_{\mathrm{ph}}(e^{j\omega})$ and $H_{\mathrm{ga}}(e^{j\omega})$, are employed for phase linearisation and to compensate for the amplitude droop introduced by the zero-order hold in the digital-to-continuous conversion process. The latter filter also serves as a digital lowpass filter, effectively limiting the maximum output frequency. To further reduce the requirements for the analog reconstruction filter, the data is oversampled, with an oversampling factor of $L = 3$ for both the LHC TFB and the SPS damper.

The convention of an ideal discrete-to-continuous-time (D/C) converter models the behaviour of the digital-to-analog converter utilized in the hardware implementation.

The analog reconstruction filter $H_{\mathrm{r}}(j\Omega)$ contraints the continuous-time signal $Y\left(e^{j\Omega T}\right)$ to its representation within the baseband. The signal subsequently drives the final stage,

which consists of a power amplifier connected to either a horizontal or vertical deflector (kicker).

The individual elements depicted in Figure 4.12 will be discussed in greater detail in the following sections. The explanations will be presented in reverse order, starting from the right-hand side block, to emphasise the effects of the analog elements in the chain and their interaction with digital signal processing.

Let the overall actuator response be denoted as $h_{\mathrm{A}}(t)$. The discrete corrector values $y[n]$ are related to the continous-time deflection signal $y(t)$ through the well-known convolution sum, expressed as follows:

$$y(t) = k_A \sum_{n=-\infty}^{\infty} y[n]\, h_{\mathrm{A}}(t - T_A - nT_{out}) \ . \tag{4.49}$$

In this context, k_A represents a conversion parameter, while T_A denotes a constant inherent delay time of the system, which will be omitted in the subsequent discussion for simplicity. The output values are generated at the sample rate of the discrete-to-continuous-time converter, T_{out}, thereby linking the n-th sequence value to the actuator response at the time instances $t = nT_{out}$. To ensure that there is no interference between consecutive symbols, the actuator's impulse response must satisfy the following condition:

$$h_{\mathrm{A}}(nT_{\mathrm{b}}) = \begin{cases} 1 & n = 0 \\ 0 & n \neq 0 \end{cases} \tag{4.50}$$

The zero crossings at the locations of neighbouring bunches prevent energy transfer that could lead to unwanted bunch coupling. This criterion is valid only when the longitudinal bunch dimension is small compared to the bunch spacing. In other words, the signal level should not change significantly during a bunch passage, which can be expressed as $T_{RF} << T_{\mathrm{b}}$. This condition is analogous to representing the bunches as macro particles with negligible temporal length ($T_{RF} \approx 0\,\mathrm{s}$).

Any response function that satisfies (4.50) will exhibit no inter-symbol interference. The set of such functions can be obtained by sampling (multiplying) (4.50) with a pulse train of Dirac delta functions, $\delta(t)$, at equidistant bunch positions, kT_{b},

$$h_{\mathrm{A}}(t) \sum_{k=-\infty}^{\infty} \delta(t - kT_{\mathrm{b}}) = \delta(t) \tag{4.51}$$

The Fourier transformation of both sides ultimately yields the necessary condition for the ideal actuator transfer function, $H_{\mathrm{A}}(j\Omega)$:

$$\frac{1}{T_{\mathrm{b}}} \sum_{k=-\infty}^{\infty} H_{\mathrm{A}}(j\,(\Omega - k\Omega_{\mathrm{b}})) = 1 \tag{4.52}$$

As can be seen, (4.52) does not necessarily imply that the actuator must be bandlimited. However, it does require that the sum of the contributions from the overlapping parts of the sidebands—periodic with a centre frequency of $k\Omega_{\mathrm{b}}$ due to the modulation with the sequence values $y[n]$—remains constant across all frequencies. By rewriting (4.52) and separating the complex components, we obtain:

$$\frac{1}{T_{\mathrm{b}}} \sum_{k=-\infty}^{\infty} \mathit{Re}\{H_{\mathrm{A}}(j\,(\Omega - k\Omega_{\mathrm{b}}))\} = 1 \tag{4.53}$$

$$\frac{1}{T_{\mathrm{b}}} \sum_{k=-\infty}^{\infty} \mathit{Im}\{H_{\mathrm{A}}(j\,(\Omega - k\Omega_{\mathrm{b}}))\} = 0 \tag{4.54}$$

These equations necessitate that the actuator's transfer function be real-valued (aside from a linear phase due to constant delay), which implies that $h_{\mathrm{A}}(t)$ exhibits even symmetry about the origin. Assuming that the actuator transfer function is bandlimited to frequencies $\Omega \leq \Omega_{\mathrm{b}}$ (which anticipates the reasonable requirement of having an economically realizable solution) allows some general statements to be made about the ideal transfer function.

First, since the band limitation implies no gain at the bunch frequency and above, the gain must be provided at DC, i.e. $H_{\mathrm{A}}(0) = 1$. Second, the transfer function at half the bunch frequency will be superimposed with a shifted version of itself, thus fixing its value at $H_{\mathrm{A}}(j\Omega_{\mathrm{b}}) = 0.5$. Rewriting (4.52) points out that the sidebands complement each other to produce a flat frequency response (see Figure 4.13)

$$H_{\mathrm{A}}(j\,(\Omega_{\mathrm{b}} - \Omega)) = 1 - H_{\mathrm{A}}(j\Omega) \tag{4.55}$$

The narrowest bandwidth solution for the actuator transfer function would be an ideal rectangular frequency characteristic:

$$H_{\mathrm{A}}(j\Omega) = \begin{cases} 1 & |\Omega| < \Omega_{\mathrm{b}}/2 \\ 1/2 & |\Omega| = \Omega_{\mathrm{b}}/2 \\ 0 & \text{otherwise} \end{cases} \tag{4.56}$$

This results in the well-known sinc-function for the impulse response. Any other transfer function that satisfies (4.55), or more generally (4.52), will deviate from the sinc pulse in time domain but will maintain the same equidistant zero crossings at the bunch locations. This observation will be further utilized to define the necessary gain and phase equalizer filters.

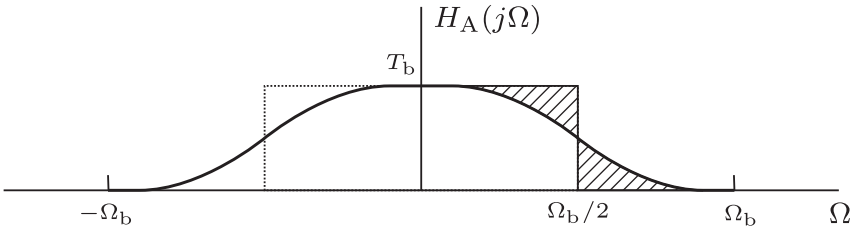

Figure 4.13: Transfer function of ideal actuator.

In summary, the simplification of the actuator model to a transparent block, as expressed in (4.73), allows us to streamline our analysis of the overall system dynamics. By treating the actuator as a non-contributing element in the closed-loop evaluation, we can simplify the mathematical treatment of the system's behavior under various operating conditions.

The subsequent subsections will delve deeper into the individual components of the actuator model, including the digital filters, the analog reconstruction process, and their respective roles in ensuring optimal performance of the feedback control system.

LHC and SPS power amplifier and deflector

The electrostatic deflector is a stretched parallel-plate capacitor through which the beam passes through at its centre. The electric field that builds up between the charged electrodes is perpendicular to the average beam trajectory, resulting in a Coulomb Force that accelerates the bunch transversely.

This type of kicker deflects the beam through the electric field. The orientation of the plates determines the operating plane, which can be either horizontal or vertical. The deflector plates are L_k long and are connected to the amplifier at their midpoint. With a kicker aperture d_k, a total deflection angle of

$$\theta_{\mathrm{kick}} = \frac{L_k}{d_k}\left(\frac{E}{q}\right)^{-1} U_{\mathrm{k}} \tag{4.57}$$

can be achieved by supplying a voltage U_{k}. Here, the longitudinal beam energy E is expressed in electron volts.

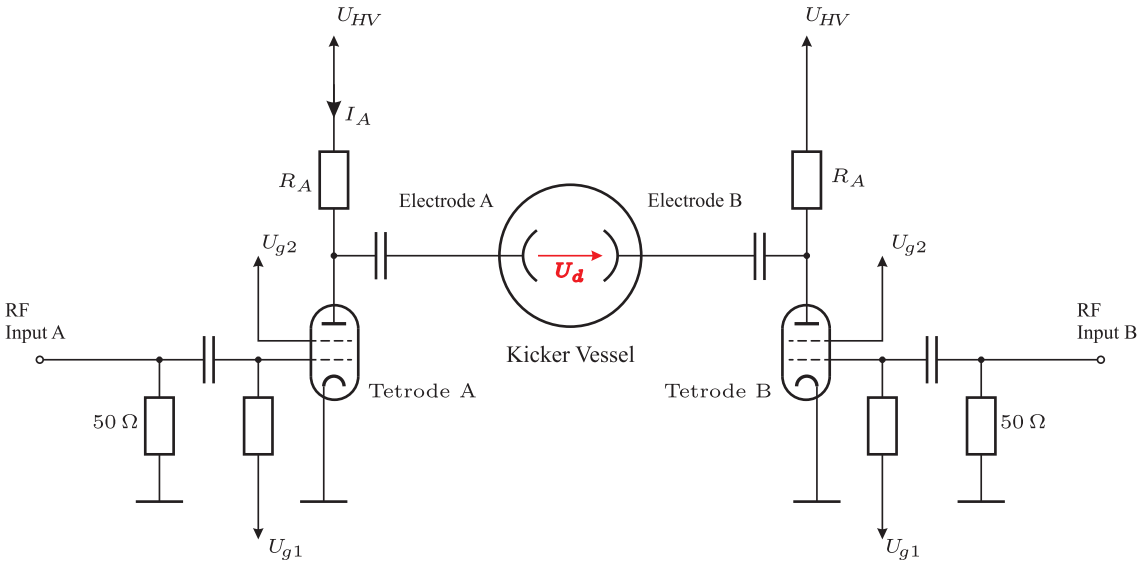

Figure 4.14: Simplified electrical circuit model of the power amplifier and deflector.

Broadband tetrode amplifiers provide the necessary drive currents to charge or discharge the deflector electrodes to the desired deflection voltage U_{k}. These amplifiers are installed beneath the damper-kicker structure in the accelerator tunnel. Each amplifier consists of two tetrodes[1], which form a push-pull stage, with one tetrode supplying one deflector plate (see Figure 4.14). The RF tubes are operated in class AB mode to minimize crossover distortion for small input signal amplitudes.

A sufficiently large RF drive signal on Input A or Input B will alternately block the tetrodes, resulting in a deflector voltage, U_{k}, that is maximally measured between the two kicker electrodes. This voltage is defined by the drawn anode current, I_A, and the voltage drop at the anode resistance, R_A. Several high voltage power converters supply the amplifiers with a regulated DC-voltage U_{HV}, a screen grid voltage U_{g2}, and a control grid voltage U_{g1}. The RF input signal is superimposed on the control grid voltage, thereby modulating the current flow in the tetrode.

The tetrode functions as a voltage-controlled current source with output impedance R_A. It operates on a reactive load impedance, specifically the total capacitance of the kicker electrode C_{K}, which allows for a large output voltage at low frequency, where it is essential for injection damping. However, as frequency increases, the capacitance shunts

[1]LHC TFB: RS-2048-CJ (Siemens design) or RS-2048-CJC (Thales design)

the impedance, thereby reducing the available kick strength at higher frequency. An equivalent circuit is illustrated in Figure 4.15, neglecting the overall gain of the amplifier between the input and the output voltages.

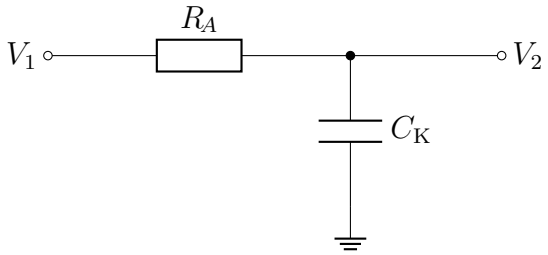

Figure 4.15: Equivalent circuit of power amplifier and kicker

As can be seen from Figure 4.15, the capacitor, in conjunction with the anode resistance, forms a first-order low-pass filter [95] with cutoff frequency of Ω_d. Transfer function measurements of the power systems performed in 2008 showed good agreement up to $10\,\mathrm{MHz}$ with the theoretical response of a first order low pass,

$$H_\mathrm{d}(j\Omega) = \quad = \frac{1}{1 + j\Omega/\Omega_d}. \tag{4.58}$$

Figure 4.16 illustrates the magnitude and phase response of (4.58) for the case of the LHC TFB, featuring a $3\,\mathrm{dB}$ cutoff frequency $\Omega_d/2\pi$ at $1\,\mathrm{MHz}$ and a nominal voltage of $V_\mathrm{max} \pm 7.5\,\mathrm{kV}$. As observed, the transfer function exhibits a distinctly non-linear phase response.

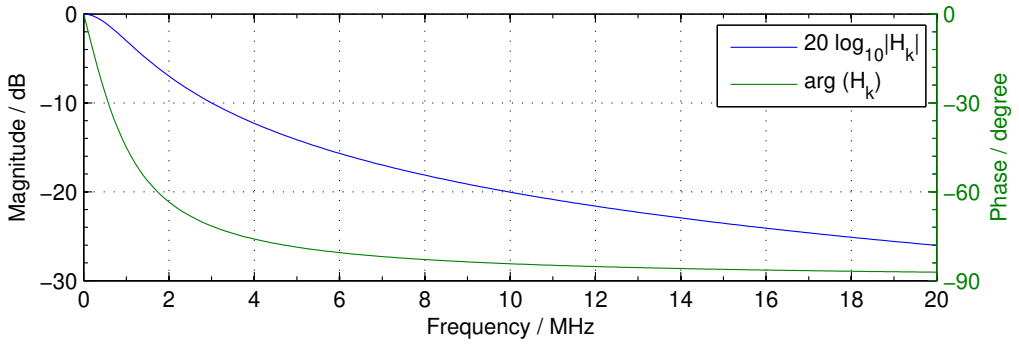

Figure 4.16: LHC power amplifier and deflector frequency response

Between $10\,\mathrm{MHz}$ and $20\,\mathrm{MHz}$ the actual power amplifiers exhibit more gain than suggested by the 1-pole roll- off [95]. Nonetheless they represent the main limitation in bandwidth in the system.

Reconstruction filter

The reconstruction filter is an important component in the digital signal processing systems of both the LHC Transverse Feedback (TFB) and the SPS damper. Its primary function is to convert the discrete-time signals generated by the digital processing units back into a continuous-time signal that can drive the actuator effectively.

In an ideal scenario, the frequency response of the reconstruction filter, denoted as $H_r(j\Omega)$, can be characterized by the following piecewise function:

$$|H_r(j\Omega)| = \begin{cases} T & |\Omega| < \Omega_N \\ 0 & |\Omega| > \Omega_N \end{cases} \tag{4.59}$$

Here, T represents the gain of the filter within the passband, and Ω_N is the Nyquist frequency, which is half of the sampling frequency. This ideal response indicates that the filter allows all frequencies below Ω_N to pass through without attenuation while completely attenuating frequencies above this threshold. This characteristic is important for preventing aliasing and ensuring that the reconstructed signal accurately represents the original continuous-time signal.

The digital signal processing system for both the LHC TFB and the SPS damper operate at a sampling frequency of $120.24\,\mathrm{MHz}$. To facilitate the reconstruction process, an analog reconstruction low-pass filter is integrated into the signal chain. The specific filter used in this application is a Mini Circuits SCLF-27, which features a cut-off frequency of $27\,\mathrm{MHz}$.

While the reconstruction filter does play a role in shaping the output signal, it is important to note that the power amplifier in the system has a first-order cut-off frequency of $1\,\mathrm{MHz}$. This means that the power amplifier will significantly limit the bandwidth of the output signal, making the reconstruction filter's role less critical in terms of frequency response. The SCLF-27 filter primarily serves to smooth the output signal and mitigate any potential high-frequency noise that may arise from the digital processing, but its impact is somewhat overshadowed by the characteristics of the power amplifier.

Discrete-to-continuous-time (D/C) converter

The Discrete-to-Continuous-Time (D/C) converter is a critical component in the signal processing chain, responsible for transforming discrete digital signals into continuous analog signals that can be utilized by the actuator. This conversion process is essential for

ensuring that the control signals generated by the digital processing units can effectively manipulate the beam dynamics in the accelerator.

The D/C converter model is illustrated in Figure 4.17. The primary function of the D/C converter is to reconstruct a continuous-time signal from a sequence of discrete samples. This is achieved through a process known as zero-order hold (ZOH), which maintains each sample value constant over a specified time interval until the next sample is available.

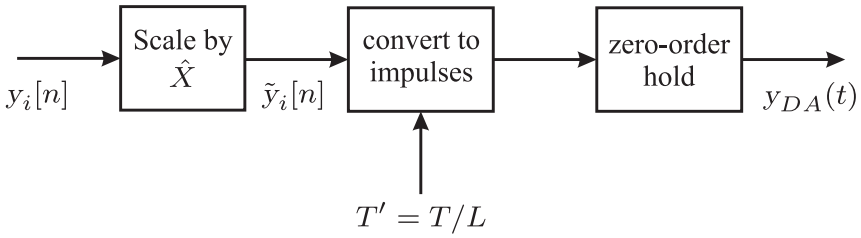

Figure 4.17: Discrete-to-continuous-time converter

The output of the D/C converter can be expressed mathematically as follows:

$$\tilde{y}_i[n] = \hat{X} y_i[n] \tag{4.60}$$

Here, $\tilde{y}_i[n]$ represents the scaled discrete signal, and $\hat{X}$ is a scaling factor that adjusts the amplitude of the signal as needed.

The continuous-time output signal $y_{DA}(t)$ generated by the D/C converter is given by:

$$y_{DA}(t) = \sum_{n=-\infty}^{\infty} \tilde{y}_i[n]\, h_0(t - nT/L) \tag{4.61}$$

In this equation, $h_0(t)$ is the impulse response of the zero-order hold, which is defined as:

$$h_0(t) = \begin{cases} 1 & 0 < t < T \\ 0 & \text{otherwise} \end{cases} \tag{4.62}$$

The zero-order hold effectively holds each sample value constant for a duration of T, creating a staircase-like waveform that approximates the original continuous signal. The output signal can then be expressed as:

$$y_{DA}(t) = \hat{X} \sum_{n=-\infty}^{\infty} y_i[n]\, h_0(t - nT/L) \tag{4.63}$$

To analyze the behavior of the D/C converter in the frequency domain, we apply the Fourier transformation to the impulse response $h_0(t)$. The corresponding transfer functions $H_0(j\Omega)$ is obtained by considering the scaled sampling period $T' = T/L$,

$$H_0(j\Omega) = \frac{T}{L} \frac{\sin(\Omega T/(2L))}{\Omega T/(2L)} e^{-j\Omega T/(2L)}\,. \tag{4.64}$$

This transfer function characterizes the frequency response of the zero-order hold, illustrating how the D/C converter affects the signal across different frequencies. The sinc function component in the transfer function indicates that the D/C converter introduces a low-pass filtering effect, which limits the bandwidth of the output signal. This is an important consideration, as it can impact the overall performance of the feedback control system.

Upsampling and gain equalization

In the context of TFBs, data is typically sampled at the bunch repetition frequency, which is $40\,\mathrm{MHz}$ in both the SPS and the LHC. However, advancements in modern digital electronics, including ADCs, FPGAs, and DACs, have enabled the support of significantly higher data rates. By leveraging upsampling and digital pre-distortion techniques, we can unlock valuable new functionalities that can enhance the performance and flexibility of the actuator. These signal processing techniques enable us to adjust the frequency response of the actuator to meet operational requirements.

Upsampling is a critical process that involves increasing the sampling rate of the input signal by an integer factor L. This is achieved through lowpass interpolation filtering, which smooths the signal and prevents aliasing (see Figure 4.18). The upsampling process effectively allows for a higher sampling rate, thereby enabling the introduction of low-pass filters with cut-off frequencies near the input sampling frequency. Without upsampling, the implementation of such filters would not be feasible, as the original sampling rate would limit the frequency response that could be accurately represented.

The relationship between the input signal $y_e[n]$ and the upsampled signal $y_g[n]$ can be expressed as:

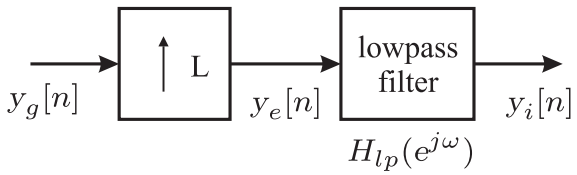

Figure 4.18: Upsamling and lowpass filtering

$$y_e[n] = \sum_{k=-\infty}^{\infty} y_g[k]\delta(n - kL), \tag{4.65}$$

where $\delta(n)$ is the Dirac delta function, and L the upsampling factor. This relationship indicates that the upsampled signal is constructed by inserting $L-1$ zeros between each sample of the original signal.

The discrete convolution sum between an input signal $y_e\,[n]$ and a finite impulse response (FIR) filter with response function $h_{lp}\,[n]$ results in the output $y_i\,[n]$:

$$y_i\,[n] = \sum_{k=0}^{N-1} y_e\,[n]\,h_{lp}(n-k) \tag{4.66}$$

where N denotes the number of filter coefficients used to describe the filter response $h_{lp}\,[n]$. This convolution effectively smooths the upsampled signal, ensuring that the transition between samples is gradual and does not introduce high-frequency artifacts.

The lowpass filter compensates for the effects of the zero-order hold (ZOH) that occurs during the digital-to-analog conversion process. The transfer function of the lowpass filter can be defined as:

$$H_{lp}(e^{j\omega}) = \begin{cases} L\tilde{H}_r & |\omega| < \pi/L \\ 0 & |\omega| < \pi/L \end{cases} \tag{4.67}$$

where $\tilde{H}_r$ is the reconstruction filter defined as:

$$\tilde{H}_r = \frac{\omega/2}{\sin(\omega/2)} \tag{4.68}$$

and $\omega = \Omega T' = \Omega T/L$. This filter ensures that the frequency components of the upsampled signal are preserved while attenuating frequencies above the Nyquist limit, thus preventing aliasing.

Gain Equalization is an essential aspect of the actuator's functionality that enhances its operational flexibility. By employing digital pre-distortion techniques, we can adjust the frequency response of the actuator to meet specific operational requirements. This capability is particularly beneficial in scenarios where the actuator can operate in two distinct modes: a "low" bandwidth mode, which provides full kick strength, and an "extended" bandwidth mode, which simulates an ideal bunch-by-bunch transverse feedback.

In the "low" bandwidth mode, the actuator delivers maximum kick strength, making it suitable for applications that require robust damping performance. Conversely, the "extended" bandwidth mode allows for finer control and responsiveness, effectively simulating an ideal feedback mechanism that can address the dynamics of individual bunches. This dual-mode operation enables tailored control of the beam dynamics, enhancing the overall stability and performance of the system.

Furthermore, the ability to switch between these modes dynamically is crucial during critical phases of beam operation, such as the squeeze phase, where precise control of the beam parameters is necessary. During this phase, the TFB can be switched to a "quiet," low-noise mode when the beams are brought into collisions, minimizing disturbances and ensuring optimal performance.

Digital phase compensation

In the context of transverse feedback systems, the power amplifier and kicker form a low-pass type circuit, as illustrated in Figures 4.14 and 4.15. The dominant pole frequency of this combination is typically much lower than the bunch repetition frequency. This disparity can lead to significant phase shifts in the feedback loop, which can adversely affect the stability and performance of the system. Therefore, it is essentail to implement phase compensation to ensure stable feedback loop operation.

Digital signal processing provides a robust framework for compensating the phase deviation introduced by the power amplifier and the deflector, denoted as H_d in (4.58). By chaining the deflector with a phase compensation filter H_{ph}, we can achieve an overall transfer function that exhibits a linear phase response with a defined group delay T_{ph}. This relationship can be expressed mathematically as:

$$H_{ph}(e^{j\omega})H_d(j\Omega) = |H_d(j\Omega)|\mathrm{e}^{-\Omega \mathrm{T_{ph}}}. \tag{4.69}$$

This equation indicates that while the magnitude of H_d remains invariant and is not altered by the phase equalizer, the phase response is adjusted to achieve the desirec linearity. Consequently, the magnitude of the phase equalizer is defined to be,

$$|H_{ph}(e^{j\omega})| \equiv 1. \tag{4.70}$$

The evaluation of the arguments in (4.69) leads to the required phase term that is to be provided by the equalizer,

$$\angle H_{ph}(e^{j\omega}) = -\angle H_d(j\Omega) - \Omega T_{ph}. \tag{4.71}$$

By substituting $\Omega = \omega/T$, we can derive the sampled representation of the phase compensation filter from the continuous-time response H_d:

$$\angle H_{ph}(e^{j\omega}) = -\angle H_d(j\omega/T) - \omega T_{ph}/T. \tag{4.72}$$

This equation provides a clear pathway for determining the necessary phase adjustment required from the phase compensation filter. The evaluation of this equation for the power system response ultimately leads to the calculation of filter coefficients that will be utilized in the phase compensation filter.

It is important to note that achieving a continuous phase response across the entire frequency spectrum can present challenges, particularly at the Nyquist frequency $\omega = \pi$. This phenomenon is reminiscent of the Gibbs phenomenon, where discontinuities in the phase response can lead to oscillations and artifacts in the output signal. Careful design of the phase compensation filter is therefore crucial to mitigate these effects and ensure a smooth transition in the phase response, thereby enhancing the overall stability and performance of the feedback control system.

Filter Coefficients from Experimental Data

The shaping of the time domain response of the actuator is critical for ensuring effective control of individual bunches within the transverse feedback system. This section discusses the measurement techniques employed, the response characteristics without digital correction, and the implementation of digital equalization, ultimately demonstrating the actuator's capability to treat bunches independently.

To accurately assess the performance of the actuator, a capacitively coupled pick-up is utilized to directly sense the voltage on the kicker. This setup is electrically terminated in $50\,\Omega$, forming a high-pass filter with a bandwidth of approximately $500\,\mathrm{MHz}$. The signals are measured in the time domain using an oscilloscope, and the raw signals are subsequently differentiated. To ensure accurate representation, all measured responses are corrected through integration of the raw signals.

In initial tests, both the digital phase equalizer and the digital pulse shaping filter were disabled. The expected response, illustrated by the green curve in Figure 4.19, is characterized by a step-up followed by an exponential decay, governed by the time constant of the power amplifier-kicker low-pass system. However, the measured response (blue curve) deviates from this expectation, primarily due to a peak in group delay introduced by the analog reconstruction filter following the DAC. The red curve represents the measured response after applying digital corrections, highlighting the improvements achieved through digital processing.

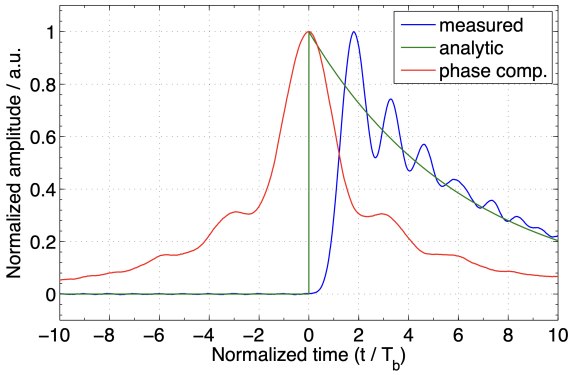

Figure 4.19: Actuator impulse response comparison: ideal (green), measured without correction (blue), and with digital phase correction (red).

In standard bandwidth operation, a digital phase equalizer compensates for the phase changes with frequency, achieving an ideal 1-pole roll-off at $1\,\mathrm{MHz}$. This compensation allows the system to operate effectively up to $20\,\mathrm{MHz}$, accommodating the maximum coupled bunch mode oscillation frequency associated with $25\,\mathrm{ns}$ bunch spacing. A digital low-pass filter begins to roll off at approximately $15\,\mathrm{MHz}$, ensuring that the overall measured response (red curve in Figure 4.19) remains symmetric. This symmetry is a direct result of the linear phase response, which yields frequency-independent group delay—an essential characteristic for damping all frequencies of interest.

The operational capabilities of the $200\,\mathrm{W}$ driver amplifier are limited to a maximum bandwidth of $25\,\mathrm{MHz}$. This constraint prompted the development of a digital pulse

shaping filter, which is specifically designed to approximate the ideal actuator transfer function illustrated in Figure 4.13.

The filter systematically tapers in magnitude, beginning at $15\,\mathrm{MHz}$, reaching a gain of 0.5 at $20\,\mathrm{MHz}$, and ultimately dropping to zero at $25\,\mathrm{MHz}$. The ideal time domain impulse response, represented by the red curve, is compared with the measured response, depicted by the blue curve, in Figure 4.20.

Although there remains potential for further enhancement—particularly in aligning zero crossings of the measured response with bunch crossings—the configurations outlined herein are designated as "extended bandwidth" settings. In this mode, which leverages both digital phase and gain equalizer filters, the actuator works like an ideal feedback system. It effectively affects individual bunches while having little effect on bunches next to them.

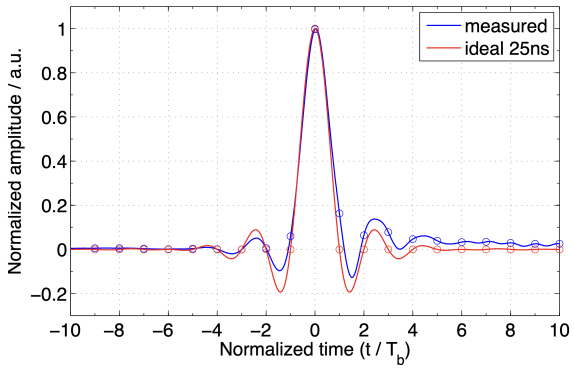

Figure 4.20: Actuator impulse response comparison: ideal (green), measured without correction (blue), and with digital phase correction (red).

The analytical modeling and experimental data of the actuator confirm its capability to treat bunches independently. The detailed modeling and thorough analysis have provided significant insights into the actuator's performance within the transverse feedback system. The hardware implementation has demonstrated its ability to manage individual bunches with minimal inter-symbol interference, ensuring accurate control and stabilization of the beam dynamics.

In summary, we demonstrate that the actuator model can be simplified to:

$$H_{\mathrm{A}}(j\Omega) \equiv H_{\mathrm{A}}(z) = 1. \tag{4.73}$$

This simplification indicates that, for the overall system evaluation, we can assume that this block is transparent and does not contribute to the closed-loop evaluations.

4.1.4 TFB controller

In transverse feedback systems, a phase adjustment is typically necessary to convert a beam position signal from a pick-up into a momentum correction signal used by a transverse kicker [10, 32, 46, 54–56]. In larger synchrotrons, pick-ups and kickers can often be positioned such that the betatron phase advance between them allows the signal to be directly applied for feedback without further phase adjustments. However, these optimal locations are not always available for installing a dedicated monitor, and the required phase advance may change in machines with cycle-dependent optics.

The following analysis aims on identifying potential solutions for transverse feedback phase adjustments using short *finite impulse response* (FIR) digital filters and one or more pick-ups.

The ultimate goal could be stated as follows: determine the slope of a particle's trajectory at the position of the kicker, to be able to counteract oscillations by correcting its trajectory (i.e. the transverse momentum p_y) on a turn-by-turn basis.

Given that — at the time of writing — there is no technique known which allows to directly measure transverse momentum, it requires an indirect method to obtain the slope via position measurements.

By recalling that a pick-up measures the real part (see Figure 4.4) it becomes obvious that if the sequence is phase rotated, by -90° or $-j$, then the corresponding slope is returned as position, y_p, seen by the pick-up:

$$y_p = \Re\{-jx\} = \Re\{-jy + y'\} = y' \,. \tag{4.74}$$

This procedure allows for two possible interpretations to realize the phase rotation: (a) Spatial phase shift, and (b) Temporal phase shift.

Spatial phase shift

Technically speaking, equation (4.74) means nothing else than to physically place a pick-up at betatron phase advance -90° with respect to the kicker. This is the simplest form of a transverse feedback. The correct phase shift required between the position measurement and application of the correction kick can be obtained by integration into properly selected positions in the accelerator lattice. However, such a scheme makes the optics design, TFB and accelerator operation complicated as there is no flexibility in any of the parameters.

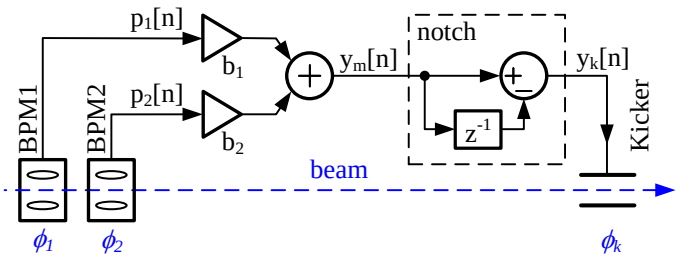

Figure 4.21: TFB signal processing using two pickups spaced exactly by $\pi/2$ (or close to) betatron phase advance. Sampling is once per turn per bunch passage, the structure is implemented for every individual bunch.

The problem can be overcome by using two beam pickups, which are conveniently placed in the lattice to have an ideal $\pi/2$ betatron phase advance between them. The two orthogonal components can be used to rotate the measured position vector by any phase by simple multiplication as illustrated in Fig. 4.21, often referenced to as *Pick-up Vector Sum*:

$$y_k[n] = p_1[n]b_1 + p_2[n]b_2 = p_1[n]\cos\varphi + p_2[n]\sin\varphi\,, \tag{4.75}$$

where φ is the required phase rotation angle.

For the combination of two pick-up signals that have a phase advance different than 90° a more general solution has been already formulated in Ref. [56], as *Pick-up Vector Sum*. As detailed therein, the two pick-up mixing coefficients follow from

$$b_{1,2} = -\frac{1}{2}\left(\frac{\cos(\Delta\phi_{Qkm})}{\cos(\Delta\phi/2)} \mp \frac{\sin(\Delta\phi_{Qkm})}{\sin(\Delta\phi/2)}\right)\,, \tag{4.76}$$

where $\Delta\phi = \phi_2 - \phi_1$ describes the phase advance between the two pick-ups, and with

$$\Delta\phi_{Qkm} = -3\pi Q_f + \phi_k - \frac{\phi_2 + \phi_1}{2}\,. \tag{4.77}$$

The fractional tune is denoted as Q_f, and ϕ_1, ϕ_2, and ϕ_k are the betatron phase advances at pick-up and kicker locations with respect to some fixed reference. Equation (4.77) is readily taking into account a one-turn delay and the phase shift of the notch filter.

Temporal phase shift

During one complete revolution a particle exhibits a precise number of oscillations, thus if the fractional tune Q_f is 0.25 then a phase rotation of 90° is achieved between

consecutive turns. By reconsidering (4.74) we can exploit this as

$$y_p[n] = \Re\{jx[n-1]\} = -y'[n-1]\,, \tag{4.78}$$

which states that the position y_p at turn n represents the negative slope, $-y'$, of the previous turn, $n-1$.

In reality, a fractional tune close to the quarter integer resonance is usually not very practical.

Using more complex digital filters, a TFB can be realized with a single pickup placed at any location in the lattice. The correction kick would be calculated from data acquired from one location, but over a number of turns. The Hilbert transform, which provides two orthogonal vector components—commonly referred to in signal processing as the in-phase *I* and quadrature *Q*—is typically used, followed by a phase rotation. The scheme is often referred to as a Hilbert phase-shifter. A typical TFB architecture (for one pickup) using this principle with the Hilbert transform realized by a finite impulse response (FIR) filter is depicted in Fig. 4.22. The method is not limited to one pickup only. Any number of pickups can be processed in parallel and the resulting correction kick is obtained as a sum of individual pickup contributions. The Transverse Feedback System in the Large Hadron Collider is typically operated in this mode using 4 pickups per beam per plane.

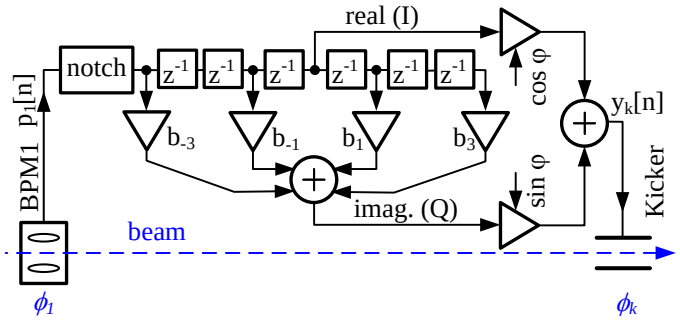

Figure 4.22: Typical signal processing for single pickup feedback using Hilbert phase shifter (7-taps). Sampling is once per turn per bunch passage, the structure is implemented for every individual bunch.

Using the Hilbert transformer coefficients [96] and phase rotation terms, the FIR filter coefficients will be:

$$\begin{aligned} b_n &= \frac{2}{\pi n}\sin\varphi \quad \text{for n odd} \\ &= 0 \quad \text{for n even} \\ &= \cos\varphi \quad \text{for n=0}\,, \end{aligned} \tag{4.79}$$

where φ is the required phase rotation angle between pickup and kicker:

$$\varphi = \phi_k - \phi_1 + Q\left(\tau_{Hilbert} + \tau_{Notch} + \tau_{Other}\right) . \tag{4.80}$$

Q is tune, ϕ_1 and ϕ_k are the betatron phase advances at pick-up and kicker locations with respect to some fixed reference, $\tau_{Hilbert}$ is group delay (in turns) of the used Hilbert filter (in the example of Fig. 4.22, $\tau_{Hilbert} = 3$), τ_{Notch} is group delay (in turns) of the used notch filter (in this example $\tau_{Notch} = 0.5$) and τ_{Other} is other hardware or algorithm specific processing delay (in turns).

The frequency response of the Hilbert phase-shifter must be taken into account when using this method. Short filters exhibit a non-negligible ripple in the response that can be detrimental for certain values of fractional tune. Longer filters have a flatter response, but introduce more delay into the feedback loop. Operating close to integer, or half-integer tunes is practically impossible. As multiple samples from a number of consecutive turns are used for every correction kick calculation, pickup measurement noise is partly reduced.

The longer processing delay of the Hilbert phase-shifter method with respect to the Vector sum method limits the maximum feedback loop gain, the tune acceptance range is also narrower. Nevertheless, the Hilbert phase-shifter method is very popular in modern digital TFBs as it provides flexibility, it is easy to follow machine parameter evolution during the accelerating cycle (tune, optics change) and if multiple pickups are used it also provides an operational redundancy, as such a TFB can run with a single pickup only.

New mathematical models and methods for phase adjustments will be discussed in more detail in section 5.4.

TFB signal processing in the Large Hadron Collider

A simplified block diagram of the digital signal processing of the LHC transverse feedback is shown in Fig. 4.23. The TFBs for each beam (1/2) and each plane (H/V) use four pickups located in the arcs around the former interaction point 4 (IP4), and their tetrode power amplifiers and deflectors are located in the LHC radio-frequency zone at IP4. Due to the TFB complexity, technical functionality is split into two modules. Beam position measurement is realized by a dedicated, very low noise beam position measurement module (BPM) providing a 1 Gbps datastream of one position sample per bunch per pickup passage (one data point every $25\,\mathrm{ns}$) [97]. The BPM module interfaces to the

RF signals from the pickups, adjusts the input gain to optimally measure bunches of all intensities used in LHC (from 1×10^9 to 4×10^{11} charges per bunch) and performs position normalization with respect to bunch intensity.

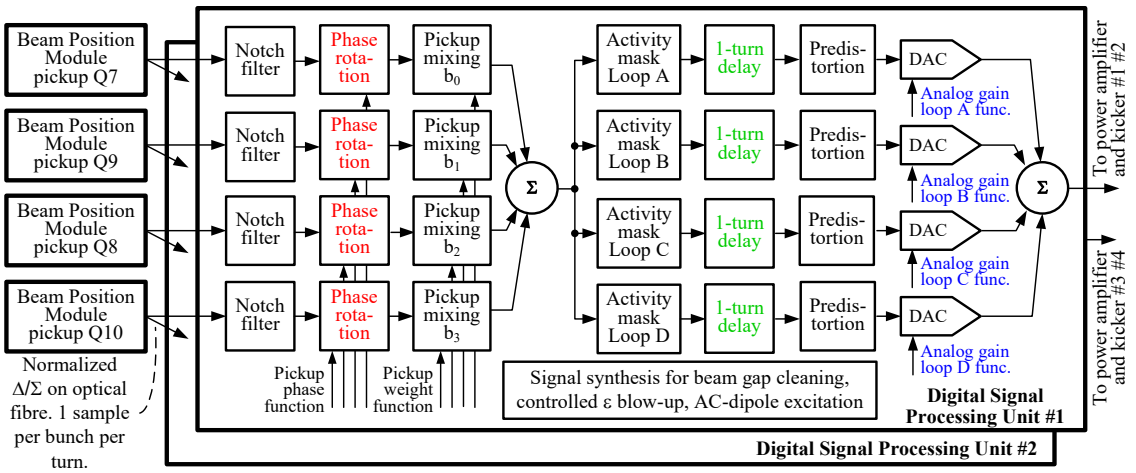

Figure 4.23: Simplified block diagram of the LHC transverse feedback signal processing. Two redundant signal processing units drive four sets of power amplifiers and kickers. Adjustment of parameters shown in color is critical for TFB performance.

Four digital streams of normalized beam positions are sent over fiber optic links to the digital signal processing module. In this module, the streams from all pickups are synchronized, and a notch filter is applied to suppress the closed orbit information. With a beam synchronous sampling clock, the notch filter also suppresses all other static signals, errors and imperfections seen by the beam position module and extracts only the oscillatory component relevant for TFB operation. Therefore, beam synchronous sampling and the notch filter relaxes already very demanding requirements for BPM electronics.

The LHC TFB has both previously mentioned signal processing schemes implemented: one Hilbert phase-shifter for each pickup controlled by a real-time function, Vector sum mode for pairs of pickups controlled by a real-time function, and an FIR filter with programmable coefficients for any other operational mode (e.g. the Komppula filters). The standard mode of LHC TFB operation is phase-shifter mode for each pickup, as it is compatible with fast damping times (10-15 turns) and it can follow the dynamic LHC optics in real time (filter coefficients are recalculated and updated approximately every 12 turns). Four pickups per beam per plane provide quadruple redundancy.

The LHC TFB signal processing supports four independent feedback loops ("activity masks" in Fig. 4.23), where groups of bunches (within one turn) can be in real time

assigned to loops with different dynamics, or other feedback features. Separate loops are used for example to treat the main LHC physics beam differently to the group of non-colliding, so called witness bunches which are needed for accelerator operation. Bunches can have strong damping of injection oscillations and then be handed over to a regular loop with lower gain.

The signal synthesis blocks generate signals for beam cleaning, white, or colored noise for controlled emittance blow-up, or AC-dipole like excitation for optics measurements. Signals can be injected into any of the four feedback channels. Each of the four outputs has individual pre-distortion filters to shape the signals and compensate the power system transfer function. Signals can be generated with a large bandwidth to, for example, manipulate single bunches within a $25\,\mathrm{ns}$ spaced bunch train, or provide an "ideal" bunch by bunch damper. Reduced bandwidth provides high strength kicks e.g. to use the TFB as AC-dipole excitation to probe dynamic aperture, or to generate a sustained $1\,\mathrm{MW}$ beam losses on primary collimators for the purpose of a magnet quench test.

4.2 TFB Parameter Identification

In the field of controls engineering, the relationship between the closed-loop transfer function and the open-loop transfer function is well established. This relationship can be expressed as a function of frequency ω:

$$CL\left(\omega\right) = \frac{OL\left(\omega\right)}{1 + OL\left(\omega\right)}. \tag{4.81}$$

In the context of a transverse feedback system, the open-loop transfer function is defined as:

$$OL\left(s\right) = GH_{\mathrm{S}}(s)\, H_{\mathrm{C}}(s)\, H_{\mathrm{A}}(s)\,. \tag{4.82}$$

Here, $OL\left(s\right)$ represents the combined transfer function of the beam, represented as G, along with the sensor, controller and actuator [98, 99].

For the system to maintain closed-loop stability, it is essential that the denominator of Equation (4.81) does not equal zero. This leads us to the stability criterion, which must be satisfied:

$$GH_{\mathrm{S}}(s)\, H_{\mathrm{C}}(s)\, H_{\mathrm{A}}(s) < (-1). \tag{4.83}$$

To describe the overall feedback system more comprehensively, we can express it in the following form, incorporating findings from Equations (4.48) and(4.73):

$$H_{\mathrm{S}}(s)\, H_{\mathrm{C}}(s)\, H_{\mathrm{A}}(s) = K \cdot e^{j(sT+\phi_{PK})}. \tag{4.84}$$

By substituting Equation (4.84) into the stability criterion outlined in Equation (4.83), we derive the conditions necesarry for stability:

$$|G| \cdot K < 1 \tag{4.85}$$

$$arg\{G\} + \omega T + \phi_{PK} = -\pi \pm \mathrm{tol}. \tag{4.86}$$

The key parameters that significantly influence the gain and phase margins, and consequently the overall stability of the feedback loop, include the loop gain K, the feedback phase ϕ_{PK}, and the total loop delay ωT. Knowing the actual values of these parameters throughout the machine cycle, and making precise adjustments are essential for optimizing the performance of the TFB. In the context of this thesis, these parameters will be systematically evaluated in the following as a part of the objectives #2 and #3.

4.3 Transverse phase space reconstruction

The following section aims in defining signal processing techniques and analysis algorithms which will allow to evaluate and quantify the parameters identified in Objective #2 and #3, from observables available within the transverse feedback system.

The LHC transverse feedback system provides bunch by bunch, turn by turn, normalized and digitized beam position signals from up to four pick-ups per plane and for each beam. Together with already existing powerful computer-based observation systems, this data can be used to reconstruct in real-time the transverse phase space coordinates of the centre-of-charges, for each individual bunch. Such information is extremely valuable for machine operation, or transverse instability diagnostics.

This section introduces methods of combining four position signals for such analysis in the presence of noise and with active transverse feedback.

One considerably useful representation of transverse motion is the use of phase space coordinates, readily described in Ref. [100] as an analytic signal $x[n]$, expressed as,

$$x[n] = y[n] + jy'[n]. \tag{4.87}$$

Here, the transverse normalized phase space coordinates $y[n]$ and $y'[n]$ represent normalized position data respectively the corresponding normalized slope values at turn index n.

For the analytic evaluation, we implicitly assume that the beam is centred in the pick-ups and we observe betatron oscillations, i.e. $(y)^2 + (y')^2 = \text{const}$. Furthermore, for our assessment, we shall use a damped, complex-valued harmonic oscillator as beam model, which provides for the k^{th} beam position monitor at the n^{th} turn the phase space coordinates as follows,

$$x_k[n] = A_0 e^{-j\phi_k} \left(\alpha \cdot e^{-j\omega_0}\right)^n. \tag{4.88}$$

Here, A_0 and ϕ_k are initial conditions, α accounts for an amplitude decay and $\omega_0 = 2\pi Q_f$ represents the angular frequency at the fractional betatron tune Q_f.

In order to satisfy Eq. (4.87), and by acknowledging that the ADT Beam Position Monitors readily provide normalized readings, we are looking for indirect methods to obtain slope samples from beam position measurements.

In the following, we evaluate two methods for combining beam position data of four LHC pick-ups, identified as a *spatial* and a *temporal phase shift* in Section 4.3, Ref. [101]. The first combines the information of several beam position monitors based on their longitudinal distribution in the accelerator, the later relies on processing the history of recorded beam position data using filter kernels.

4.3.1 Spatial method

This method relates the data measured by two or more independent beam position monitors at different longitudinal azimuths. Fig. 4.24 outlines the case for $N = 2$ signal sources. For this method, the beam position monitors should have a betatron phase advance ideally between $60^o < (\phi_2 - \phi_1) < 120^o$.

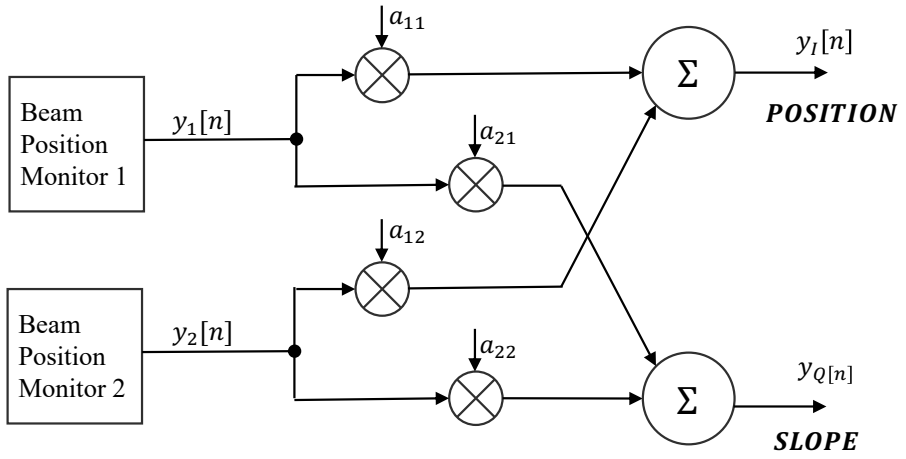

Figure 4.24: Spatial phase space reconstruction: in-phase term $y_I[n]$ and quadrature component $y_Q[n]$ calculated from vectorial rotation and combination of two beam position sequences $x_1[n]$ and $x_2[n]$.

For the case of the LHC ADT, the data provided by individual beam position monitors $y_k[n]$ are meticulously time-aligned during setting-up, with index n corresponding to the same bunch data at the same turn. Therefore, using the "Pick-up Vector Sum" algorithm from Equation (4.76) it can be shown that, choosing appropriate mixing coefficients a_{11} and a_{12}, the position signal $y_I[n]$ in Fig. 4.24 of a virtual beam position monitor can be constructed, such that

$$y_I[n] = a_{11}y_1[n] + a_{12}y_2[n]. \tag{4.89}$$

Equivalently, applying the same approach of pick-up signal mixing, and by taking into account an additional 90^o phase advance compared to the virtual beam position used for Eq. (4.89), we obtain the representation of the slope, $y_Q[n]$, described as

$$y_Q[n] = a_{21}y_1[n] + a_{22}y_2[n]. \tag{4.90}$$

The pair of Eq. (4.89) and (4.90) represent Cartesian coordinates, describing the reconstructed phase space for an arbitrary longitudinal position. It is a convenient practice to chose the ADT kicker position as reference for the phase space reconstruction. By using the same longitudinal reference this technique is further expandable for using multiple beam position monitors – four in the case of the LHC ADT – as shown in Fig. 4.25.

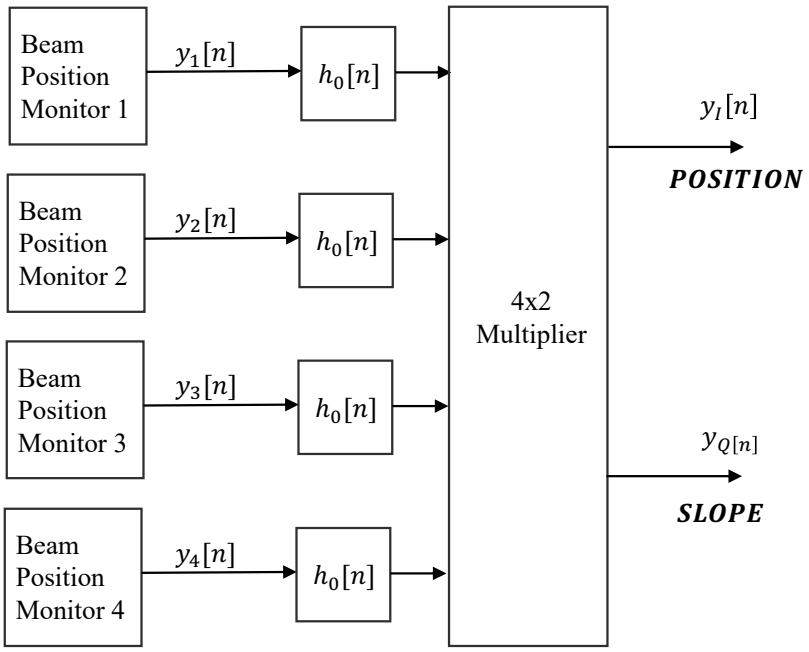

Figure 4.25: Spatial combination of four beam position streams.

We therefore obtain an analytic signal $x_S[n] = y_I[n] + jy_Q[n]$ as the reconstructed normalized transverse phase space based on a scalar combination of real-valued position sequences, $y_k[n]$, using

$$x_S[n] = h_0[n] * \sum_k (a_{1k} + ja_{2k}) \cdot y_k[n]. \tag{4.91}$$

The asterisk operator $(*)$ represents the discrete-time convolution of the weighted BPM signals with an additional finite impulse response (FIR) filter of impulse response $h_0[n]$, allowing shaping of the input noise. When no filter is used, this method has zero group delay and therefore it is suitable for applications requiring low latency.

4.3.2 Temporal method

Referring to Equation (4.78) [100], this reconstruction method obtains the slope signal as the 90^o phase rotated version of the position data utilizing digital filters.

In order to reconstruct the analytic signal in Eq. (4.87) we are looking for a solution that allows to transform a sequence of position samples, $y[n]$, into a sequence of corresponding slope samples, i.e.

$$y'[n] = L\{y[n]\}\ . \tag{4.92}$$

Thereby, the operation denoted by $L\{\cdot\}$ in Eq. (4.92) is commonly known as *Hilbert transform* and is explained for example in Ref. [92].

A more practical approach can be found by noticing that $y'[n]$ is the $90°$ phase-rotated version of $y[n]$. This phase shift can be generated by simple means of digital filtering — as it is already been done in the feedback phase controller [101].

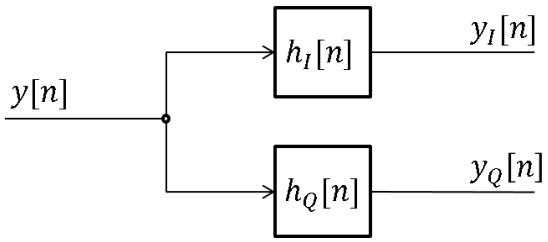

Figure 4.26: Phase space reconstruction using two digital filters.

Figure 4.26 shows how the phase space is reconstructed by means of two individual digital filters. The two branches with filter kernels h_I[n] for the in-phase component, and $h_Q[n]$ for the quadrature component generate two quadrature output signals, named $y_I[n]$ and $y_Q[n]$, which can be combined to a final analytic signal, representing a reconstruction of the transverse phase space,

$$c[n] = y_I[n] + jy_Q[n] = y[n] * (h_I + jh_Q)\,. \tag{4.93}$$

As an intermittent research result, elaborate filter kernels including DC suppression were defined, tuned for the fractional tunes of the particular plane, to attenuate out-of-band signals. Examples of filter kernels for fractional tunes used in the LHC transverse feedback systems are listed in Table 4.1. With only five coefficients these filters are usable with possible damping times of $10\,\mathrm{turns}$ or less.

Table 4.1: Filter kernels LHC.

(a) Horizontal, $Q_f = 0.275$

$h_I[n]$	$h_Q[n]$
-0.1837	+0.0447
-0.1224	-0.4922
+0.6122	+0.0000
-0.1224	+0.4922
-0.1837	-0.0447

(b) Vertical, $Q_f = 0.31$

$h_I[n]$	$h_Q[n]$
-0.1322	+0.1136
-0.1983	-0.4542
+0.6612	+0.0000
-0.1983	+0.4542
-0.1322	-0.1136

As outlined in Fig. 4.27, bunch-by-bunch data $y_k[n]$ provided from individual Beam Position Monitors passes through a pair of matched filter kernels, denoted as $h_I[n]$ as

$h_Q[n]$. The filters' even and odd symmetric impulse responses generate in-phase (I) and quadrature output signals (Q), which can be combined afterwards thanks to an identical group delay.

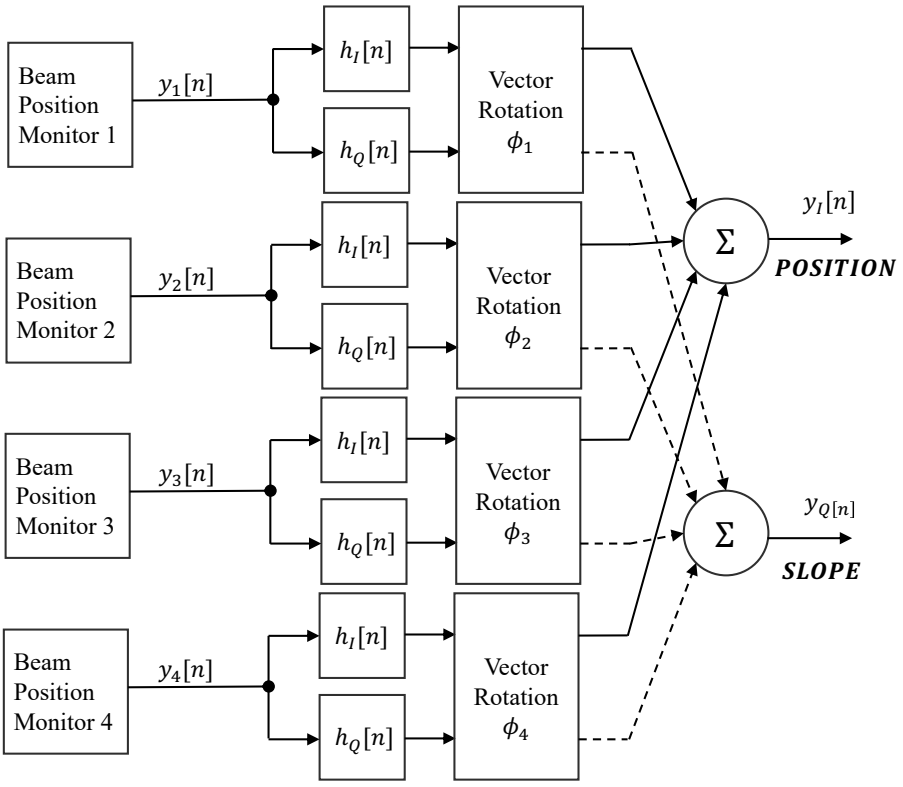

Figure 4.27: Temporal phase space reconstruction using matched digital filters $h_I[n]$ and $h_Q[n]$ on the input data stream $y_k[n]$ of four Beam Position Monitors.

It is worth noting that the calculated FIR filter output pairs readily represent phase space coordinates at the longitudinal position of the corresponding monitor. Therefore, to aggregate four pick-ups to an arbitrary longitudinal reference location, the individual output vectors need to be aligned before summing their contributions. This is done by a vector rotation, ϕ_k, towards a common longitudinal position (e.g. to the location of the ADT kicker).

The analytic signal $x_T[n] = y_I[n] + jy_Q[n]$ obtained from the temporal method can therefore be described as,

$$x_T[n] = \sum_k \left(y_k[n] * \left(h_I[n] + jh_Q[n] \right) e^{j\phi_k} \right). \tag{4.94}$$

With a short 5 taps kernel length, these filters are tuned to exhibit nominal transmission at the fractional tune for the corresponding plane, rendering them applicable for

a tune range exceeding ± 0.02 around the target tune [100].

The suggested methods in Section 4.3 are both valid candidates for reconstructing the transverse phase space in real-time. With the spatial method being attractive for the analysis of fast beam transients, for example during injection transients and with $5\,\mathrm{turns}$ damping time, both methods profit from the suppression of out-of-band noise using filter kernels which improves the SNR (see also Section 4.6).

Potentially, more elaborate filter response functions can be designed to lower the SNR even further, for instance by processing the beam position data of 100 to 1000 turns.

4.4 TFB parameter extraction

We describe a method for feedback parameter extraction, as required by Objective #1. This method is based on transverse excitations generated by the kicker of a TFB. It involves reconstructing the transverse phase space using digital filters for each individual pick-up, as detailed in Section 4.3. The analysis is conducted entirely in the time domain, without any conversion to the frequency domain.

For our analysis we recall 4.87, an analytic signal $x[n]$ which describes the evolution of a particle in normalized transverse phase space coordinates

$$x[n] = A_0\, e^{-j\phi_0} \left(\alpha \cdot e^{-j\omega_0}\right)^n \ . \tag{4.95}$$

For simplicity we assumed that the particle motion is dominated by active damping (see also Ref. [102]), thus reducing the analysis to linear optic effects of the magnetic guidance field and exponential amplitude decay. Equation (4.95) describes a damped harmonic oscillation at turn index n, with angular frequency ω_0 and a decay factor, α, and with initial amplitude and phase denoted as A_0 resp. ϕ_0. Note that the negative exponents preserve the direction of rotation in normalized phase coordinates (positive phase $\mapsto$ clockwise; downstream).

In order to extract essential parameters of a transverse feedback system from bunch-by-bunch beam data we shall consider the case of a beam in a steady state — any transients have settled — which has been excited transversely by the TFB for less than one turn (illustrated in Fig. 4.28).

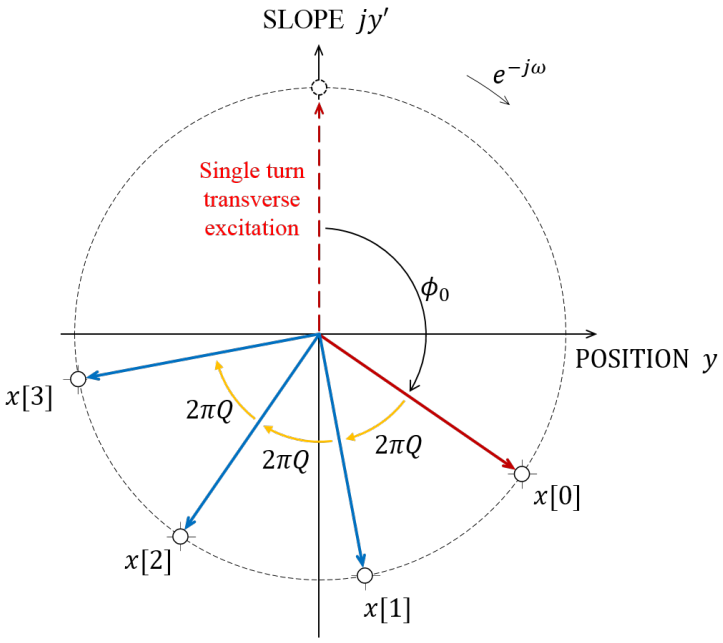

Figure 4.28: Transverse phase space plot (normalized) at the position of a pick-up. A transverse deflection commutes from the location of the kicker to the coordinates of the pick-up by a fixed phase angle (denoted as ϕ_0), with subsequent turns advancing in phase by the fractional tune ($\Delta\varphi = 2\pi Q$).

4.4.1 TFB gain

We define the transverse activity, $A[n]$, as the magnitude of the vector $x[n]$,

$$A[n] = \mathrm{abs}\{x[n]\}\,, \tag{4.96}$$

which is a measure of the instantaneous oscillation amplitude in the normalized transverse phase space.

From Eq. (4.95) it follows that,

$$A[n] = A_0\alpha^n\,, \tag{4.97}$$

with the magnitude A_0 defined by the initial excitation amplitude of the transverse deflection at turn $n = 0$. If $A[n]$ decreases over time then the transverse activity is considered to be damped, whereas growing values provide an indication of transverse instability.

By noting that the change in amplitude per turn in Eq. (4.97) is constant and defined by the decay factor $\alpha \equiv e^{-1/\tau_d}$, we can derive the decay time τ_d from the transverse

activity. This is done by comparing two time instances, n_1 and n_2, using the following equation:

$$\tau_d = (n_2 - n_1) \left(\log \frac{A[n_1]}{A[n_2]} \right)^{-1} . \tag{4.98}$$

In control systems, the damping time τ_d is inversely related to the product of the damping ratio ζ and the natural frequency ω_n, expressed as $\tau_d = \frac{1}{\zeta \omega_n}$. This relationship is fundamental in understanding how feedback influences system dynamics, particularly in terms of response speed and stability [103]. For weak internal damping, this relationship can be further simplified to $\tau_d = \frac{2}{K}$, where K is the feedback gain.

Rearranging this equation allows us to express the feedback gain as a function of damping time:

$$K = \frac{2}{\tau_d}. \tag{4.99}$$

For a detailed analysis of the effect of damping feedback on a second-order system, we refer to Appendix A, where we derive the relationship discussed.

4.4.2 TFB phase

As shown in Fig. 4.28, in the very same turn when the kick ($\pi/2$ or $+j$) has been applied, i.e. $n = 0$, the betatron phase advance between kicker and pick-up effectively transforms the transverse deflection in normalized coordinates, thus leading for the initial condition of Eq. (4.95),

$$\phi_0 = \frac{\pi}{2} - \mathit{arg}\{x[0]\} . \tag{4.100}$$

More generally, according to Eq. (4.108) we notice that any subsequent beam oscillations recorded by the pick-up will advance by the fractional tune. We can therefore determine also for later turns an initial phase, $\psi[n]$, from the argument of the analytic signal by including a linear phase term,

$$\psi[n] \doteq \frac{\pi}{2} - \mathit{arg}\{x[n] \cdot e^{j2\pi Q \cdot n}\} . \tag{4.101}$$

From this we instantly obtain the phase advance between the kicker and the pick-up by averaging over M consecutive turns,

$$\zeta = \frac{1}{M} \sum_{k=0}^{M-1} \psi[k] . \tag{4.102}$$

4.4.3 TFB delay

For the stability of a TFB it is essential that kick signals are well aligned with the time of arrival of the bunches. In the following we derive a method which aims on quantifying the kicker delay offset.

We now consider the case of a kick signal which is modulated in amplitude over one turn. Thereby, a sinusoidal kick waveform with M periods per machine turn is sampled by a bunch with index k depending on the time of arrival at the location of the kicker. The resulting bunch oscillation magnitude, described as,

$$A_k = A_0 \cdot \cos\left(\frac{2\pi M}{h} \cdot k + 2\pi M \cdot \eta\right) , \tag{4.103}$$

is then recorded as betatron oscillation decay at a downstream pick-up. Here, the harmonic number h represents the maximum number of buckets per turn, and a delay offset factor, $\eta = \Delta T / T_{\mathrm{Rev}}$, defined as the ratio between the kicker delay offset, ΔT, and the revolution period, T_{Rev}.

If this kick exercise is repeated with two phase-shifted versions of the modulation signal in quadrature, denoted as A_I and A_Q, we can reconstruct an IQ-footprint of the traversing bunches at the kicker as,

$$\chi[k,n] = A_I[k,n] + jA_Q[k,n] . \tag{4.104}$$

As can be easily verified, bunches are equally distributed around a circle with constant radius. Therefore, unwinding the phase response of Eq. (4.104) by taking into account a linear position-dependent phase term,

$$\rho[n] = \mathit{arg}\left\{\chi[k,n] \cdot e^{-2\pi M k/h}\right\} , \tag{4.105}$$

and averaging over populated bunches and N turns results in,

$$\theta = \frac{1}{N}\sum_{m=0}^{N-1} \rho[m] \doteq 2\pi M \cdot \eta . \tag{4.106}$$

Since $\eta = \Delta T / T_{\mathrm{Rev}}$ it follows for the delay offset:

$$\Delta T = \frac{\theta}{2\pi M} \cdot T_{\mathrm{Rev}} . \tag{4.107}$$

It is worth noting that the offset factor in Eq. (4.103) is weighted by M, thus increasing the sensitivity to delay offsets. Ultimately, if $M = h$ then the resulting phase in Eq. (4.105) depends solely on the delay offset factor.

4.5 Accelerator parameter extraction

Objective #3 calls for investigation and proposal of methods and required signal processing techniques to extract vital accelerator parameters from observables available within the transverse feedback system. The parameters of interest would be bunch-by-bunch machine tune and damping time. The data or results should be preferably available in real time or immediately after injection.

4.5.1 Bunch-by-bunch tune

The single-turn excitation transients described in Section 4.4 provides us sufficiently large oscillation amplitudes for a duration of several of turns (typically 5 - 100, depending on the requested feedback gain), to extract the turn-by-tune.

By rewriting Eq. (4.95) as recurrence formula we obtain the coordinates for consecutive turns by evaluating

$$x[n] = x[n-1] \cdot \alpha e^{-j\omega_0} \,. \tag{4.108}$$

As can be seen, after a turn the sequence has advanced in phase by $\Delta\varphi = \omega_0 \equiv 2\pi Q$. Therefore, by taking the ratio over two consecutive turns we can express the per-turn or instantaneous fractional tune, $Q[n]$, as

$$Q[n] = \frac{1}{2\pi} arg\left\{\frac{x[n-1]}{x[n]}\right\} . \tag{4.109}$$

It is worth noting that Eq. (4.109) allows for correctly characterizing the fractional tune to be below or above the half-integer resonance.

4.5.2 Damping time

Equation 4.98 already describes the bunch-by-bunch damping time, which can be extracted from transverse activity data.

4.6 Sensitivity to noise

In this section we analyse the expected performance of the transverse phase space reconstruction methods introduced in section 4.3 in the presence of noise.

We model the inherent noise from each Beam Position Monitor as an independent additive white Gaussian noise process, $e[n]$ ($\overline{e[n]} = 0$, noise power $\overline{e^2[n]} = \sigma_e^2$), which is added to the desired noise-free position signal, $y_p[n]$,

$$y[n] = y_p[n] + e[n]. \tag{4.110}$$

The convolution in Eq. (4.91) and Eq. (4.94) with selective FIR filters lets signals close to the target tune pass unaltered in amplitude, but shapes the noise power for out-of-band signals. For the example of the in-phase filter (equivalent for the quadrature component), the noise power follows from,

$$\sigma_I^2 = \sigma_e^2 \sum_m |h_I[m]|^2 . \tag{4.111}$$

The overall noise contribution is further reduced by the superposition of $N = 4$ Beam Position Monitors, leading to a final RMS noise amplitude,

$$\sigma_A = \sigma_e \sqrt{\frac{\sigma_I \sigma_Q}{N}}. \tag{4.112}$$

It can be shown that the activity defined in Eq. (4.96) with noise present according to Eq. (4.110) follows the well known Rice probability distribution. The expected RMS amplitude noise follows the RMS input noise, reduced by filtering and by the combination of 4 BPMs. For example, in the case the filter kernels listed in Table 4.1 are used for the temporal method, then the expected total process gain is $9.2\,\mathrm{dB}$.

The measurement noise also affects the observable fractional tune (Eq. (4.109)) from the reconstructed phase space data $x_T[n]$, with the RMS phase noise given as,

$$\varphi_{\mathrm{rms}} = \mathrm{atan}\frac{\sigma_A}{A_0} \tag{4.113}$$

At this point it is worth noting that, for large amplitudes $\overline{A[n]} >> 10\sigma_A$, the reconstructed values for amplitude and phase exhibit measurement noise following the assumed normal distribution (standard deviations σ_A respectively φ_{rms}), however, due to the filtering their spectral density is no longer white.

Furthermore, for $\overline{A[n]} << 10\sigma_A$ the observed phase vector resembles a uniform distribution, with an arbitrary phase value between $[-\pi, \pi]$, providing no useful information on the fractional tune. Numerical simulations using Eq. (4.88) and a BPM noise floor of $\sigma_e = 0.219\,\mu\mathrm{m}$ (taken from [93]) indicate that a minimum signal to noise ratio (SNR) of $20\log_{10}(A[n]/\sigma_e) \geq 30\,\mathrm{dB}$ is required to obtain an RMS tune variation of σ_Q better than 10^{-3}.

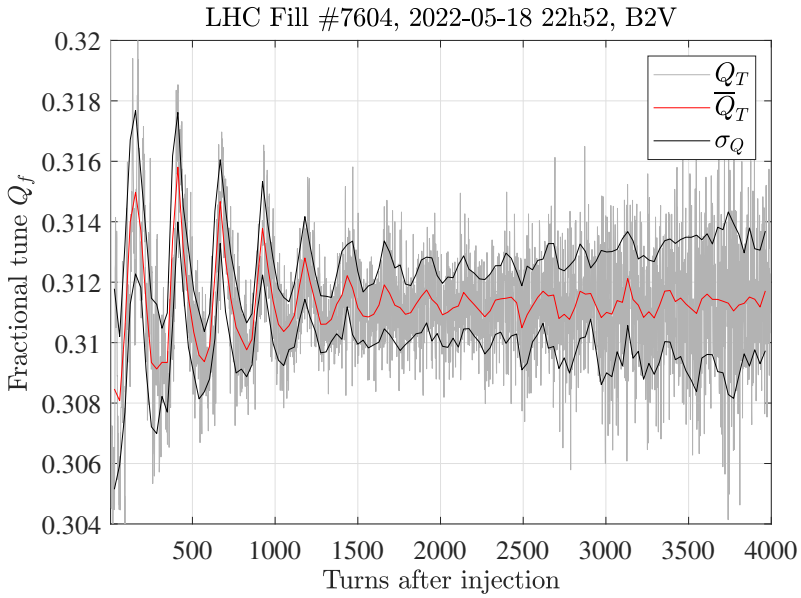

Figure 4.29: Fractional tune from reconstructed transverse phase space using 4 LHC BPMs using the temporal method.

This value is confirmed by measurements of LHC injection transients, shown in Fig. 4.29 as an example, where the turn-by-turn fractional tune of one individual bunch is reconstructed from 4 LHC BPMs using the method described by Eq. (4.94). The red trace indicates the 16-turns moving average of the instantaneous fractional tune $Q_T[n]$ (in gray), and with the RMS tune error depicted in black. Between 2000 and 2500 turns after injection the oscillation amplitude has decayed to an SNR of approx. $30\,\mathrm{dB}$, and the measured RMS tune variation $\sigma_Q = 1.1 \cdot 10^{-3}$, which is in excellent agreement with the numerical prediction.

4.7 Computational complexity

In order to be useful, it is important to investigates the computational complexity of the proposed methods and the signal processing techniques, as laid out in objective #4, with a focus on evaluating how the algorithms could be realized based on real-time processing in Field Programmable Gate Arrays (FPGA), real-time processing in high-performance computing system, or offline processing.

During the LHC Long Shutdown II the LHC transverse feedback system (ADT) [104] was subject to an upgrade of its Beam Position Monitor (BPM) hardware, aiming for an improvement of the system's noise floor [93]. New low-noise beam position hardware is now available for LHC Run III, providing independent processing of 16 dedicated pick-ups. This allows for a total of four beam position streams per plane and per beam, representing the transverse centre-of-charges of each individual bunch.

This data is available in real-time to the LHC Transverse Feedback system for damping and stabilizing the beam, as well as to the computer-based observation system ADTObsBox. The LHC transverse feedback system is powered by Xilinx Artix 7 FPGAs (XC7A200T-1FFG1156C) providing 740, 48-bit DSP blocks and a total of 13140 kB of fast RAM. Apart of the mandatory TFB signal processing, the FPGA allows to implement a simple version of fast transverse instability detection, or few simple FFT algorithms.

The ADTObsBox [105, 106] is a very powerful computer system capable of recording and processing all digital data streams from the 16-available pick-ups and 4 digital signal processing units at full data rate (bunch-by-bunch or $40\,\mathrm{Msps}$, with $16\,\mathrm{bit}$ resolution), totaling to $20\,\mathrm{Gbit/s}$. The system for instance combines the data in real-time and extracts valuable metrics of the ADT performance (e.g. transverse activity) or the beam itself (bunch-by-bunch fractional tune).

The ADTObsBox system deployed in LHC contains three servers - real time processing server, data storage and buffer server, and a development server.

The real time processing machine is optimized for processing data in real time and providing a high level information like transverse instability detection, spectrum analysis for slow ground motion measurements, tune extraction, damping time extraction. The hardware configuration is: up to 96 processing threads (cores), $768\,\mathrm{GB}$ RAM, $0.165\,\mathrm{Tflops/s}$. The system can be extended by installing GPUs, providing additional computing power up to $880\,\mathrm{Tflops/s}$. Current server load is approximately $20\,\%$ continuous.

The data storage and buffer server is optimized for recording data and making them available for on the fly analysis (not real time in terms of machine turns, but also not off-line) and permanently saving the data to a non-volatile storage. Data are catalogued for example as injection transient, post mortem data, or various on-demand data. All are used for long term accelerator performance analysis (e.g. all injection for the last year). Special feature of this system, till now something unheard of, is a 24-hour long, bunch by bunch, turn by turn circular buffer. If anything goes wrong in the machine, users are able to retrieve the full rate position data of the event from all TFB pickups for an analysis. If the algorithm is very computationally intensive, beam data from this server can be used for an offline analysis on a different machine. The hardware configuration is: up to 96 processing threads (cores), 192 GB RAM, 150 TB of disk storage capable of simultaneous read/write and continuous writing at 20 Gbps. Computing power 0.165 Tflops/s. Current server load is approximately 27% continuous.

The third, development server is used to test and evaluate new methods and algorithms. The hardware configuration is: up to 96 processing threads (cores), 384 GB RAM, 0.165 Tflops/s. The system can be extended by installing GPUs, providing additional computing power up to 880 Tflops/s. Current server load is approximately 2% continuous.

Chapter 5

Results

In this chapter, we present the results of our research, which aims to verify and validate the methods outlined in Chapter 4.

To address Objective #1, we implement a brief transverse excitation of a bunch using the TFB kicker, which results in controlled beam oscillations. In the subsequent section, we employ numerical simulations and particle tracking code to assess whether this method is detrimental to the beam.

The Measurements section focuses on analysing results obtained from real beam data collected during the LHC 2024 commissioning. The data, recorded with the assistance of the TFB observation systems, is utilized for a comprehensive verification of the described methods. This is followed by detailed measurements aimed at evaluating the sensitivity of each method to variations in parameters. Objective #2 involves the evaluation of TFB parameters, while Objective #3 pertains to accelerator parameters. Both objectives are thoroughly analysed in the context of the LHC TFB, with results presented from data collected during the regular machine start-up.

The subsequent section addresses Objective #4, demonstrating the practical application of the proposed methods. We detail the real-time extraction of transverse activity for each individual bunch, a metric introduced by this study that has become increasingly significant for machine operation. We also elucidate how the LHC operations group accesses these results in a real-world implementation.

Finally, the concluding section of this chapter is dedicated to advanced signal processing techniques and digital filter design. Here, we present our findings related to Objective #5, which focuses on enhancing the robustness of transverse feedback systems in the context of tune variations.

5.1 Numerical simulations

In Section 4.6 of the Methods chapter we highlighted the need for a minimum oscillation amplitude to effectively analyze and extract transverse feedback and accelerator parameters. To achieve this, it is crucial to excite the beam in a short and controlled manner, which helps to avoid beam losses and maintain beam quality, in particular by minimizing transverse emittance blow-up. In the following, we present the results of numerical simulations conducted to address the objective #1. These simulations investigate the effects of a short tranverse excitation on beam size in the presence of a strong transverse feedback system.

The simplified approach exploited in Section 4.1.1 describes the tracking of the centre of gravity of a bunch. A bunch is represented as a single macro particle that performs betatron oscillations as it travels along the magnetic guidance field. It is assumed that the machine has a linear optic and it's lattice is decoupled, hence, the betatron motion identified by (3.14) essentially describes the particle's trajectory in two degree of freedom.

In a perfectly linear machine, a single particle starting on a trajectory offset from the closed orbit will continue to exercise transverse oscillations, and a distribution of particles injected will maintain its r.m.s. size. The centre of gravity will continue to oscillate with constant amplitude about the closed orbit.

In a real machine, however, any non-linearities in the lattice will eventually lead to decoherence. Using the above macro particle model, in the absence of an active transverse damping term the oscillation amplitude reduction is based on the assumption of an exponential decay of the coherent oscillations, described by

$$\frac{dx}{dt} = -\frac{1}{\tau_{\mathrm{dec}}} x\,(t) \tag{5.1}$$

At this point it is worth noting that, taking into account a tune spread of many particles, the decaying of the oscillation with the spiralling movement of particles in phase space is rather poorly described by an exponential law for the decay of the centre of mass motion. The exponential decay described by (5.1) imposes a maximum reduction in oscillation amplitude at the very first turns, while according to the analytical expressions [3] the dependence with time follows a power law $-(t/T_0)^2$ for the first few turns. $T_0 = 88.9\,\mu\mathrm{s}$ denotes the revolution time. The decoherence becomes only visible when

the outer regions of the bunches have sufficiently drifted away from the centre and start to deform the transverse bunch distribution. This is illustrated in Fig. 5.1.

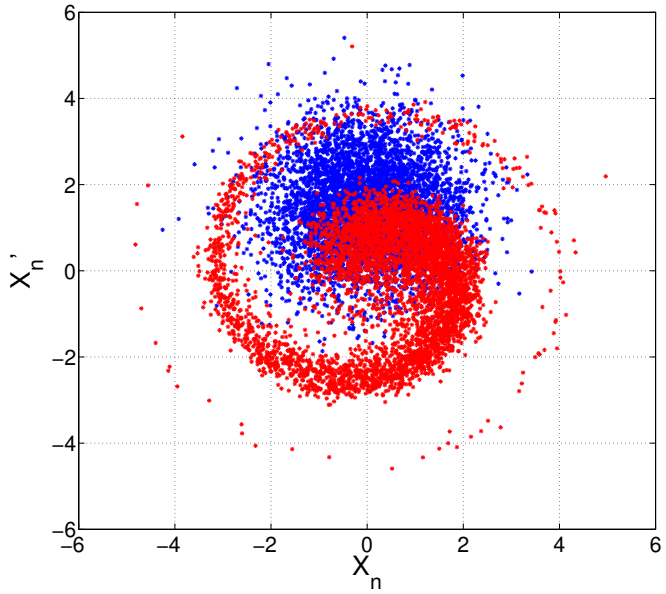

Figure 5.1: An injection error of $\Delta X'_{\mathrm{n}} = 1.5\ \sigma$ leads to a turn by turn filamentation of a bunch (blue, initial beam size ϵ_0); an amplitude dependent tune spread of the individual particles is assumed. Filamentation after 750 turns is shown in red for $\mu = 10^{-4}$, $Q' = 2$, and $(\Delta p/p)_{\mathrm{rms}} = 0.44 \times 10^{-3}$. Without active damping the emittance increases to $\epsilon/\epsilon_0 = 2.125$.

Therefore, in the absence of an active transverse damping term and to evaluate the transverse beam size, a more accurate description needs to take into account the exact nature of the filamentation process and require a multi-particle simulation.

Without feedback, analytical formulas have been derived for the decoherence by chromaticity and octupoles [3, 107]. In the case of chromaticity alone and under the assumption of constant synchrotron frequency, full recoherence occurs after one synchrotron period. In practice, octupoles and the fact that the synchrotron frequency itself depends on momentum prevents complete recoherence.

In general, the dependence of the machine tune Q on amplitude can be expanded into a power series

$$Q = \sum_{k=0}^{\infty} a_k r^k \tag{5.2}$$

with $r > 0$ representing the amplitude of oscillation. $k = 0$ represents the central tune in this model and $k = 2$ the octupolar term with a quadratic dependence of tune

with amplitude. Sextupoles in a location with dispersion provide a change of tune with momentum. However, when the beam is centred, sextupoles do not provide a tune change with betatron amplitude. In the present simulation we combine the decoherence effects caused by octupoles and chromaticity with the active damping by the feedback. Other sources of decoherence are not considered.

When defining the parameters of the LHC transverse feedback system it has been assumed that all oscillations would be damped during the initial decoherence and any effect of re-coherence has not been taken into consideration. Note that the damping time aimed for is of the order of $1/4$ of the synchrotron period.

As in the derivation for the analytical expressions [3] it is assumed that distributions in transverse and longitudinal phase space are not correlated, i.e. particles are initially selected to have randomly distributed transverse and longitudinal phase space coordinates. Gaussian distributions are used for both planes, longitudinal and transverse. Detailed analytical expressions for the decoherence of coherently kicked particles can be found in [3, 107]. The parameters for the tune shift are identify as $a_0 = Q_\beta$, $a_1 = 0$, and $a_2 = \mu$ in (5.2) and the average Q on turn k becomes

$$Q[k] = Q_\beta - \mu(r[k])^2 + Q'\delta[k] \tag{5.3}$$

$\delta[k]$ is the turn dependent longitudinal relative momentum deviation from the synchronous particle.

Fig. 5.2 compares different assumptions for the parameters of Eq. (5.3). The numerical results agree with analytical formulas in [3, 107] for the combined case of decoherence due to a quadratic tune change with amplitude (octupoles) and linear tune change with momentum via chromaticity.

The results presented in Figure 5.2 are promising for our Objective #1. The green curve indicates that, in the absence of active damping, filamentation caused by the tune spread occurs at a relatively slow rate—slower than the damping times for which the LHC TFB is designed. During the first 100 turns, there is almost no slope and minimal decay in the oscillation amplitude. This is advantageous when considering the blue trace, which illustrates the exponential decay described by (5.1). The effect of chromaticity, represented by the red trace, shows a pattern of recoherence after each synchrotron period. With actual damping times of 10 turns, the TFB action will significantly reduce the oscillation amplitude before the first decay modulation due to chromaticity occurs.

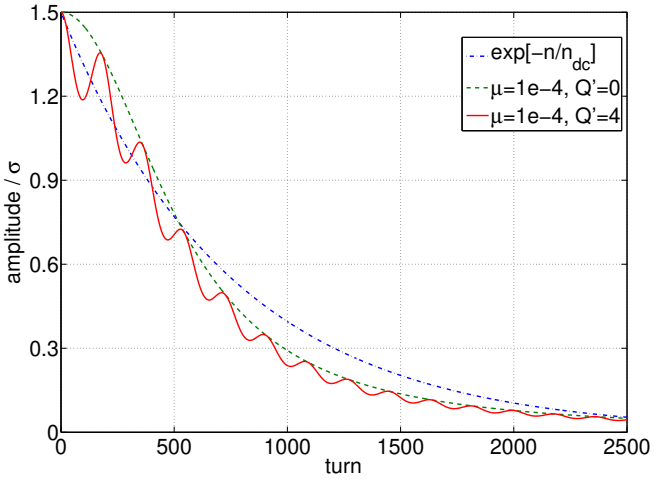

Figure 5.2: The centre of gravity motion (envelope) of a filamenting bunch without active damping shows different decaying characteristics. A first approximation describes an exponential decaying amplitude (blue, dash-dotted) with parameter $\tau_{\mathrm{dc}} = 750$ turns. The green curve (dashed) accounts for a detuning proportional to r^2, e.g. octupolar fields, with $\mu = 10^{-4}$. In case of a non-zero value for the chromaticity and non-vanishing momentum spread the decay is modulated by recoherence (red, solid). Analytical expressions were used [3].

In references [108, 109], we have numerically quantified that the residual emittance increase after a full-scale excitation is indeed very small when active transverse feedback is applied.

5.2 Measurements

In this section, measurements obtained from real beam data during the LHC 2024 run will be utilized to verify and confirm the described methods in Sections 4.3, 4.4 and 4.5, as well as to identify areas for improvement. By comparing the actual data with the expected results, any discrepancies will be highlighted.

5.2.1 Method verification

During the regular machine start-up following the year-end technical stop (YETS 2023/24), the LHC was carefully prepared with circulating beams as part of the transverse feedback commissioning process. This preparation aimed to ensure the proper functioning of all

TFB components and to optimize performance for the upcoming run.

As part of this effort, measurements were taken with both beams filled with 12 witness bunches and two batches of 72 bunches. Witness bunches are strategically placed in specific bucket locations with intentionally reduced TFB gain. This setup is crucial because it allows the LHC tune measurement system (BBQ) to reliably detect the machine's tune, even in the presence of a strong transverse feedback system and its highly sensitive beam position monitors.

The two sets of 72 nominal bunch trains were each configured with standard TFB gain to achieve nominal damping times. Importantly, all TFB settings were carried over from the previous 2023 run, facilitating a seamless transition into the 2024 operational phase. The settings were not guaranteed to be the most optimal nevertheless. By default, the TFB was active during injection and the flat bottom plateau to preserve the beam's transverse emittance.

Phase space reconstruction method

For the analysis, experimental data was collected in April 2024 from the eight ADT processing modules, with two systems per plane and per beam. The dataset includes information from four pick-ups. Figure 5.3 displays the data acquired by the ADT observation system, where each color represents raw data from a single pick-up, labeled Q7 to Q10, corresponding to the quadrupole magnets where they are installed.

The data points indicate the normalized transverse position information recorded by the associated beam position monitor (see Section 4.1.2). At the system's sampling rate of $40\,\mathrm{MSPS}$ (or $25\,\mathrm{ns}$ per sample point), the equivalent record length of the x-axis is approximately $13.1\,\mathrm{ms}$. The y-axis is represented in 16-bit encoded signed binary codes, allowing for a value range of $[-32\,768,\ 32\,767]$, corresponding to a transverse beam movement in the TFB pickups of $\pm 1.5\,\mathrm{mm}$ ($\pm 1.7\,\sigma$ at injection energy and $\pm 6.8\,\sigma$ at flat top).

Notably, based on the data in Figure 5.3, the mean beam position of pick-up Q7 (blue trace) is not well centered, unlike the other three pick-ups. A well-centered beam in the pick-up is crucial to avoid potential saturation issues with the ADCs during large transverse beam excursions, which may occur for example during the setting-up phase of the injection system.

Upon carefully inspecting the raw traces, one can observe a low-amplitude oscillation, or 'wiggle', present during the first 60 turns. This is active short, controlled excitation at the beginning of the record, generated by the ADT controller and applied to the beam using the ADT kicker.

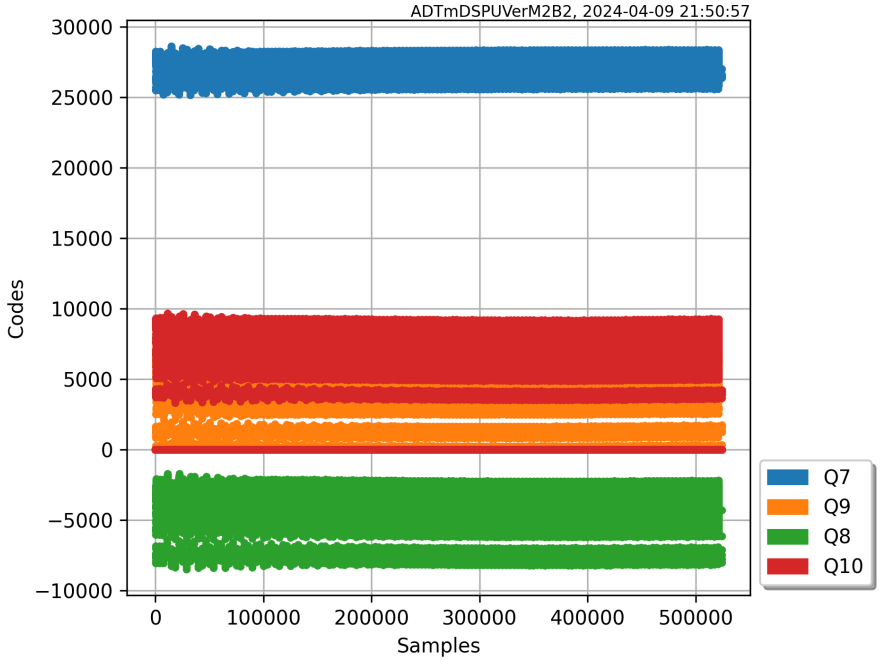

Figure 5.3: Raw data from four pick-ups captured by the ADT observation system, totaling $524\,288$ samples per data stream.

A detailed snapshot of this excitation is shown in Figure 5.4. The green trace represents the transverse positions recorded during the first three turns. At turn number 2, the ADT triggers a precisely timed single turn excitation (orange trace), which lasts exactly one turn, or 3564 samples. As shown, the excitation amplitude drops to zero before the position data of turn 3 is recorded.

Time synchronization with the circulating beam is important, to ensure that the response is truly representing an impulse response function. Additionally, periodic waveforms are intentionally selected, like the cosine excitation pattern shown with $N = 1$ (number of oscillation periods per turn), to ensure that the mean excitation voltage is zero. The applied excitation waveform discharges the kicker to zero voltage within the same turn when applied, thus the AC coupling of the ADT power system does not pose a problem.

In this demonstration, we observe that for the selected cosine excitation with $N = 1$,

the deflection voltage for the circulating bunches in the machine remains nearly at full scale. This is also shown in Figure 5.5.

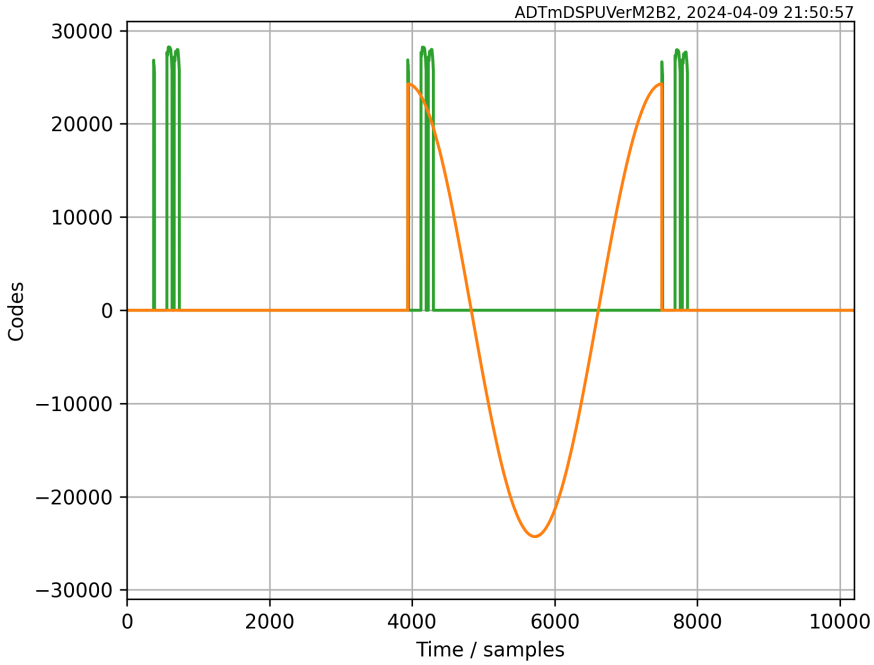

Figure 5.4: First 3 turns of pick-up data with cosine excitation pattern (N=1) applied during the second turn.

Since unpopulated bunches with zero intensity do not provide position readings, the recorded data retrieved from the ADT observation system primarily consists of zero values. Out of 3564 buckets, there are $12 + 2 \times 72 = 156$ populated bunches. This means that less than 5% of the recorded $524\,288$ samples contains actual information.

To better visualize and process the data, we first reorganize the vector of continuous readings into a two-dimensional format with dimensions $\mathrm{turns} \times \mathrm{buckets}$. In our example, this would result in a matrix of size 147×3564, with some unused samples at the end. However, in the current implementation of the ADT observation system, the record does not start with bucket 0, which means we need to drop some samples also at the beginning. As a result, the matrix shape becomes 146×3564.

Next, we focus only on the buckets that contain bunches with an intensity above a preset threshold value. This refinement alters the matrix dimensions to $\mathrm{turns} \times \mathrm{bunches}$, which, for the purpose of this demonstration, evaluates to 146×156 per pick-up. With this setup, we can visualize the time evolution of each individual bunch on a turn-by-turn basis, as illustrated in Figure 5.6 for the data from one pick-up and 156 bunches.

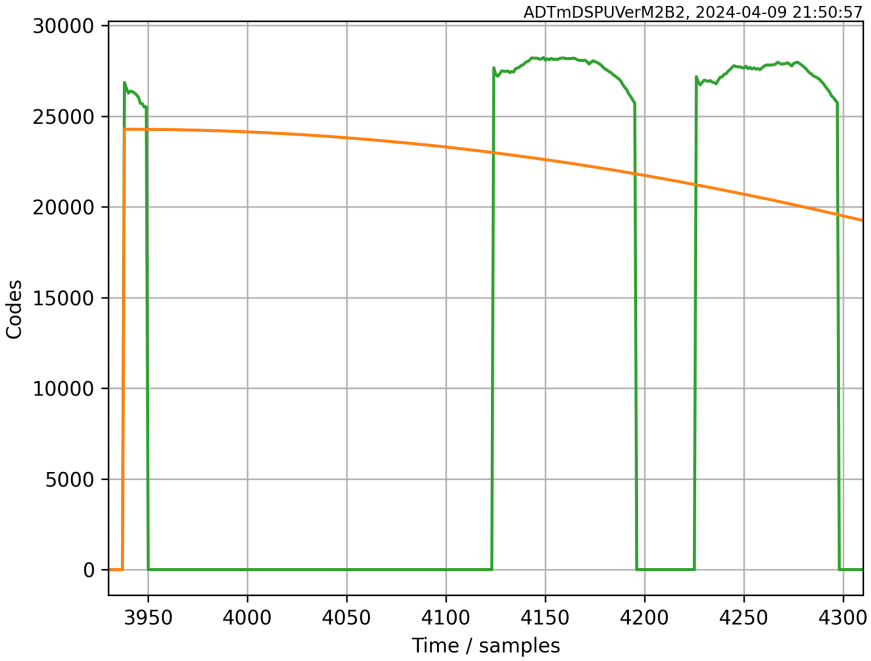

Figure 5.5: Detailed view of bunch pattern during the second turn: first 12 bunches, followed by a gap, then 2x 72 bunches. Excitation frequency N=1 is shown.

As shown, the applied one-turn excitation causes all bunches to oscillate coherently lower than $0.05\ \sigma$, while the TFB action subsequently dampens this oscillation over approximately 20 to 60 turns.

Each of these bunch-by-bunch traces is now analyzed according to Eq. (4.93), and the results are utilized to reconstruct the transverse phase space plots. Figure 5.7 presents the application of the two reconstruction filter kernels detailed in Section 4.3, Table 4.1. Notably, in comparison to Figure 5.6, both traces demonstrate a zero mean position. This outcome is a direct result of the notch filter implemented in the FIR filter kernels, which effectively mitigates unwanted frequency components.

However, during the initial turns, the I and Q components exhibit significant excursions. These excursions can be attributed to transient effects introduced by the FIR filters themselves. To enhance the clarity of the oscillation patterns, we shift the plots to commence after the filter transients have sufficiently decayed. This adjustment is illustrated in Figure 5.8. As a result, we can discern the intricate oscillation patterns of each bunch, with a peak oscillation amplitude reaching approximately 400 codes.

The filtered one-dimensional turn-by-turn input data is now prepared for visualization as a two-dimensional transverse phase space plot, as shown in Figure 5.9. As anticipated,

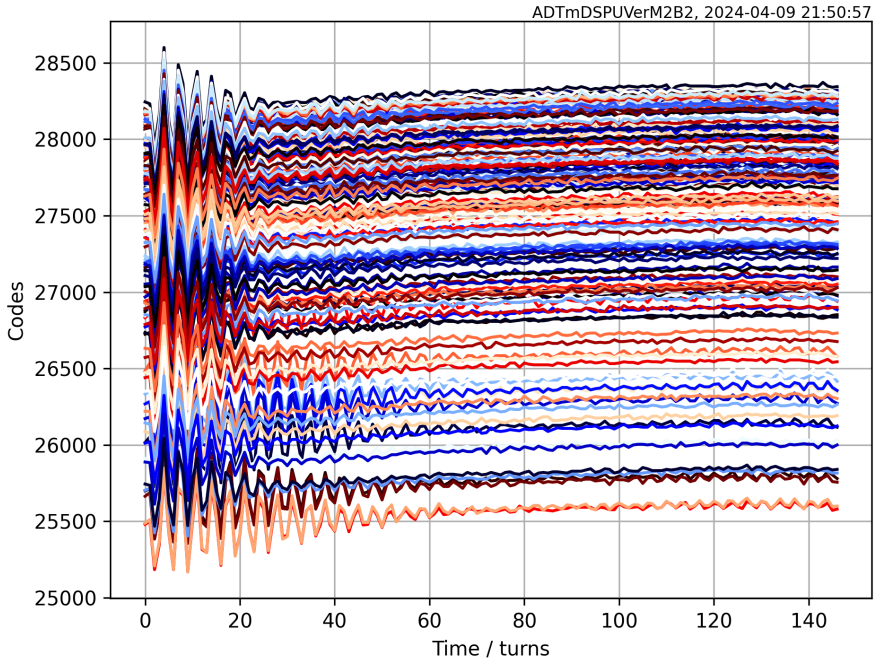

Figure 5.6: Analyzing single pick-up data: Bunch-by-bunch turn-by-turn position over 146 turns. Baseline offset is due to the beam not centered in this pickup and slightly drifting. The excitation amplitude is very low, 1000 codes on vertical axis corresponds to $0.05\,\sigma$ movement.

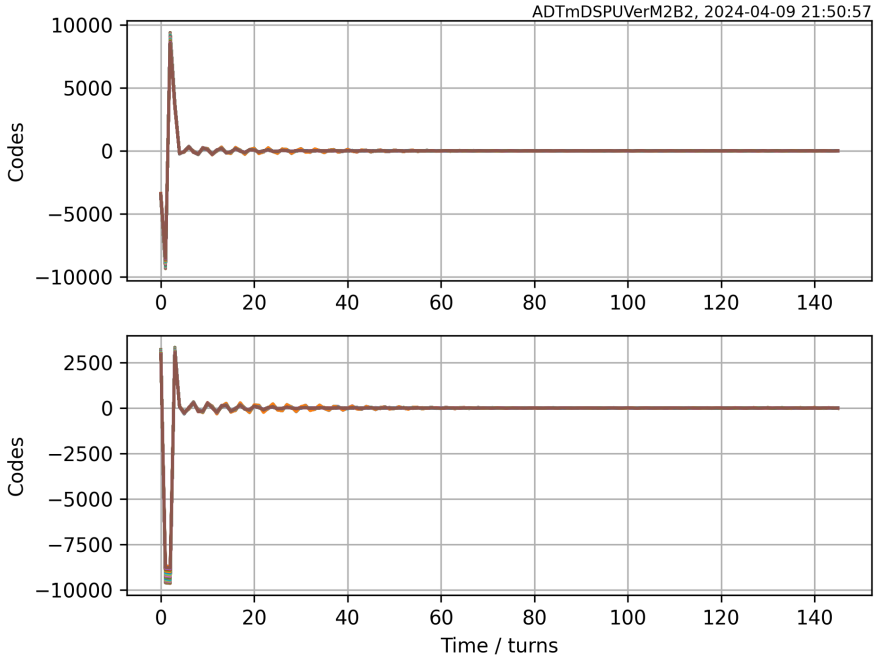

Figure 5.7: Visualizing I and Q components from individually filtered bunch-by-bunch data. Filter filling transient is clearly visible.

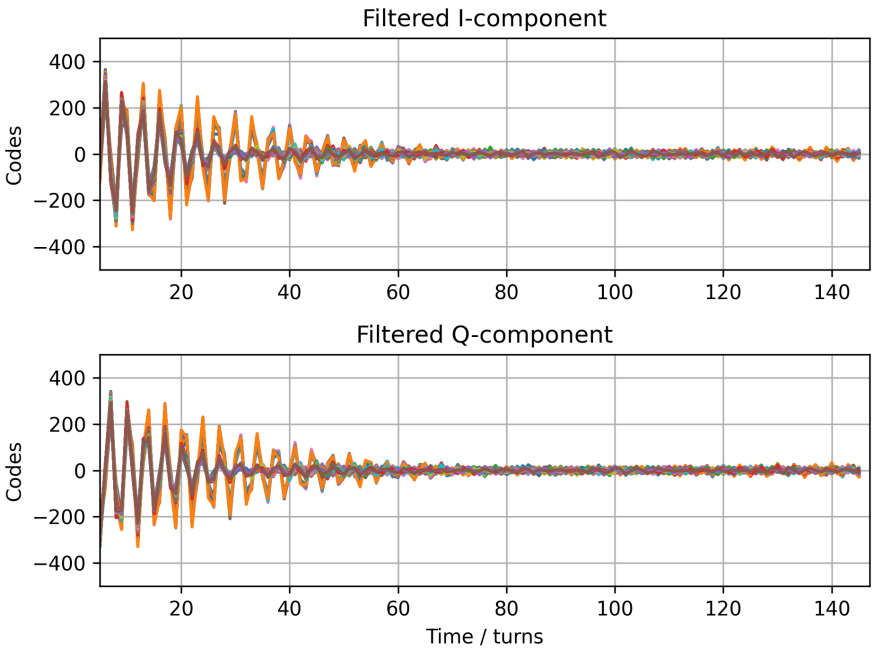

Figure 5.8: Filtered I and Q components plotted after the decay of filter transients.

the feedback action plays a crucial role in the dynamics of the system, resulting in the reconstructed traces exhibiting a pronounced spiraling behaviour toward the center over consecutive turns. This spiraling effect indicates the system's stabilization process, where the feedback effectively reduces deviations from the desired trajectory (closed orbit). We are particularly interested in analyzing these traces, as they contain valuable information about the feedback system, its performance, and specific parameters that influence the accelerator operation.

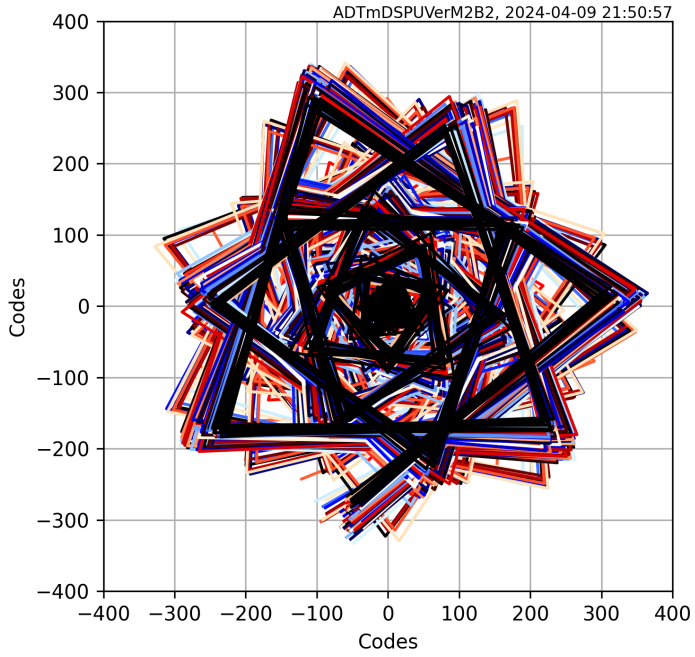

Figure 5.9: Transverse phase space plot reconstructed using single pick-up data and I/Q filtering.

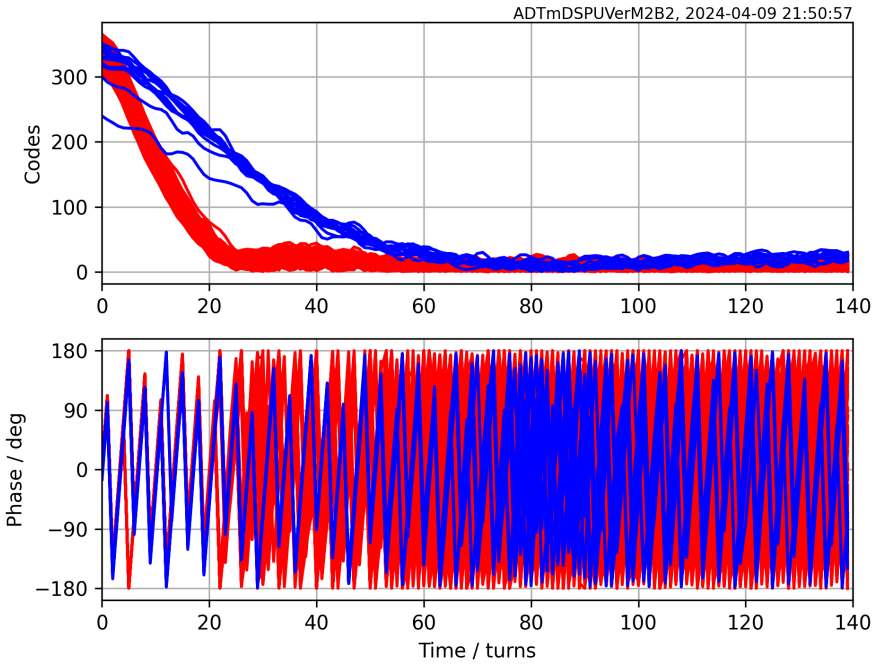

Figure 5.10: Transverse phase space analysis: amplitude (top) and corresponding phase plots (bottom).

Transverse Activity and Damping Time

Figure 5.11 illustrates exemplary how a single bunch oscillates over time after a single-turn transverse excitation is applied (shown by the green trace). By using the reconstructed phase space as input data, Equation (4.96) quantifies the transverse activity in terms of instantaneous oscillation amplitude, or envelope (represented by the blue and orange traces). The shape of the oscillation envelope is a key indicator of how well the TFB system is controlling the oscillations. It directly reflects the effectiveness of the feedback action, providing important information about the system's performance. An optimally designed and well-configured TFB system should quickly dampen oscillations, resulting in a rapid decay of amplitude. On the other hand, if the transverse activity shows prolonged oscillations or a slow decay, it may indicate that the TFB system is not functioning as intended.

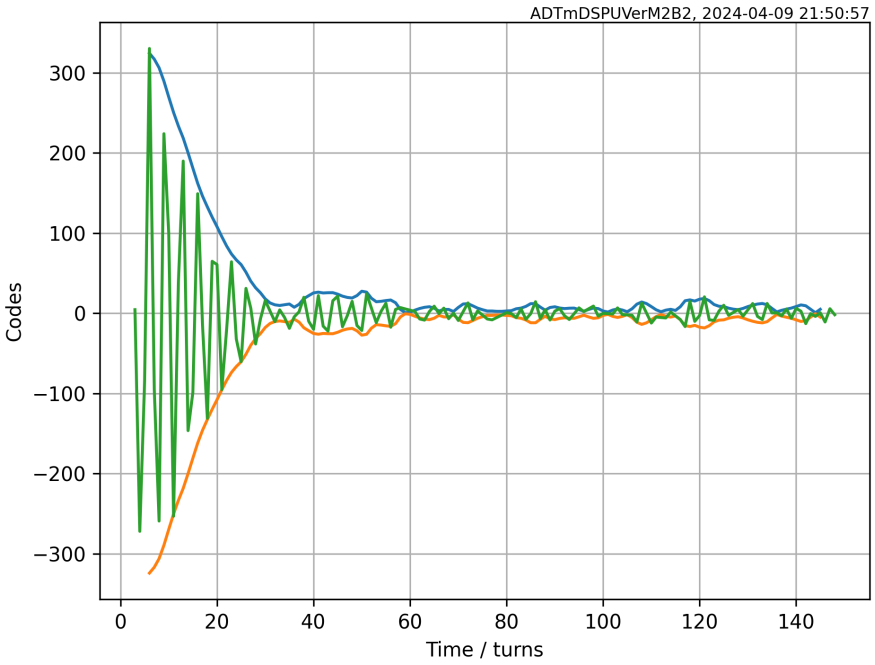

Figure 5.11: Transverse betatron oscillation decay post excitation kick, with envelope signals from digital signal processing.

We further extend our analysis to include all 156 bunches. The left plot of Figure 5.12 evaluates the transverse activity over time for Witness bunches (blue traces) and Main bunches (red traces). A visual inspection of this figure reveals two clearly separated clusters, indicating different damping regimes. This behaviour is expected, as we have Witness bunches experiencing a lower TFB gain compared to Main bunches. While the

red traces overlap well, the blue traces exhibit some scatter. This variation results from the initial oscillation amplitude, as can been seen in the right-hand plot of Figure 5.12. Despite the cosine excitation function with $N = 1$ being requested to start at bunch position 0, the effective kick voltage seen by the beam cannot respond instantaneously due to power and bandwidth limitations in the actuator component. Consequently, the first 12 bunches display the charging behaviour of the kicker and amplifier system, with bunch 0 receiving the lowest deflection kick.

To mitigate this issue, one could adjust the synchronization window of the excitation pattern to start before bucket 0, allowing sufficient time for the kicker to charge up to the nominal voltage. However, this adjustment must not affect the mean voltage sent to the power system, and each bunch must be kicked only once.

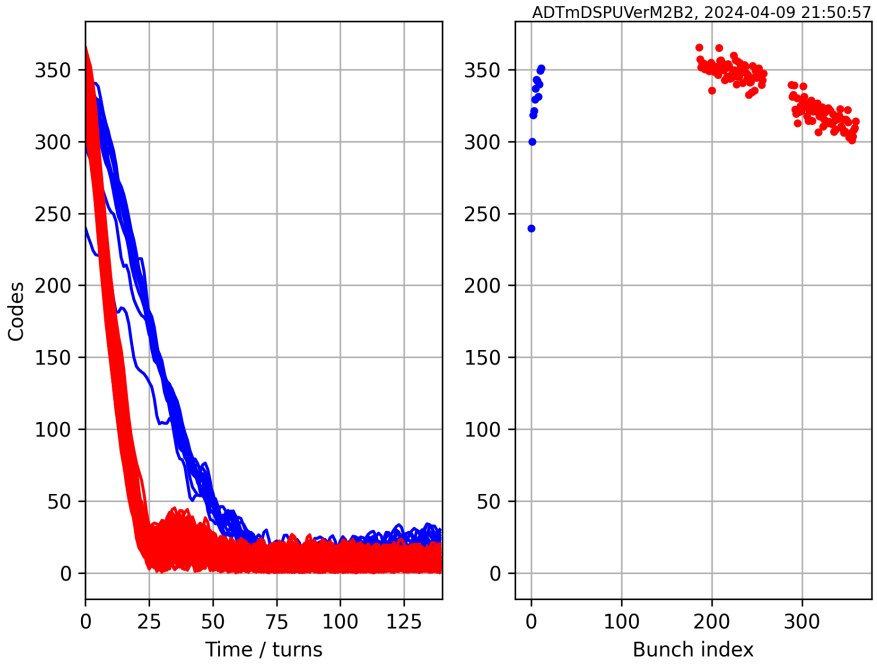

Figure 5.12: Comparison of oscillation amplitude decay over time (left plot) and peak oscillation amplitudes per bunch at turn 6 (right plot) for bunches 1 to 12 (blue traces) and two trains of 72 bunches (red traces). Movement of 400 codes corresponds to 0.02σ.

Using the previously derived transverse activity per bunch, Equation (4.98) defines the decay factor, also known as the damping time. Figure 5.13 displays two black dashed curves overlaid on the left plot, representing the estimated damping times for bunches 10 and 200, based on an exponential decay model. The decay time constant for all bunches can be obtained from the right graph.

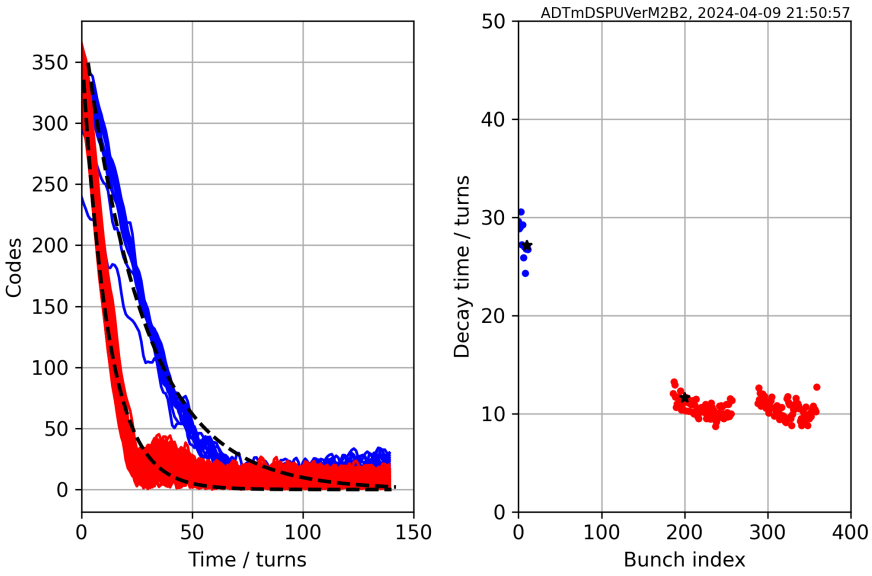

Figure 5.13: Oscillation amplitude decay over time (left plot) and exponential decay time estimation per bunch (right plot). The black dashed lines represent exponential decay curves for bunches 10 and 200, with time constants and peak amplitudes derived from the estimates.

The estimation model clearly distinguishes between the two damping regimes, with damping times for the Witness region estimated to be between 25 and 30 turns, while the Main bunches are damped at approximately 10 turns.

Referring to the first-order difference equation (4.18) in Section 4.1.1, we have:

$$x[n] = \alpha x[n-1] \qquad n > 0.$$

This recursion formula defines the observed beam position at turn n in relation to the position at the preceding turn. From this equation, one can readily deduce that for any non-zero value of α, the sequence will either grow or decay exponentially[1]. This behaviour aligns with our expectations for a pure P-controller, where the corrective action is proportional to the error input.

Regular monitoring of system performance is essential to proactively identify feedback issues. This capability is now achievable, thanks to the signal processing method introduced in this thesis.

It is important to note that proper selection of samples from the excitation transient is critical to obtain correct results. Digital filters used to reconstruct the phase space

[1] An exception occurs when $\alpha = 1$, which results in a steady oscillation that preserves the amplitude.

need a certain number of samples to fill, until the result is valid and these need to be discarded. Equally at the decay side, only samples with sufficient signal to noise ratio should be used for reconstruction. Typically, two time constants worth of good data is necessary to measure the damping time with useful accuracy. If the damping time is very short (for example 10 turns like in LHC) we need either an ultra-low noise BPM, or increased excitation amplitude. Alternatively, where available, multiple pickups at $\pi/2$ phase advance can be used to reconstruct the phase space (section 4.3.1) without losing precious samples in the filter filling transient.

Tune Estimation

In this section, we continue to utilize the reconstructed phase space as input data, as was done in the previous section, and shift our focus to the evaluation of the argument of the phase space. Figure 5.10 provides a comparative analysis: the upper graph depicts the previously described transverse activity, while the lower graph presents the corresponding phase.

As outlined in Section 4.6, the comparison of the two graphs underlines that, in the presence of noise, the extracted phase data deteriorates as the initial oscillation amplitude decays. When the amplitude of a complex-valued sequence drops below the noise floor, the phase reading becomes unreliable and susceptible to distortion. In this regime, noise dominates the measurement, resulting in phase jitter and random fluctuations that do no longer accurately represent the original signal's phase. Consequently, any phase information extracted may be incorrect, which compromises the quality of parameter extraction.

For Main bunches (indicated by red traces), an oscillation amplitude of 100 codes or higher (out of a full scale $\pm 32\,768$ codes, i.e. 0.005σ) yields a satisfactory phase reading just before turn number 15. A similar observation holds true for the Witness bunches (blue traces). The slower decay in oscillation amplitude until approximately turn 40 implies a better SNR for an extended time, during which the quality of the phase reading is also higher.

In our quest to extract accelerator parameters from the pre-processed beam position data, we focus on the delta phase value between consecutive turns. This relationship is derived in Section 4.5.1, where we introduced the instantaneous fractional tune in Equation (4.109). The results of our analysis are presented Figure 5.14, which illustrates the evolution of the bunch-by-bunch fractional tune for each individual bunch. Calculating

the difference between two phase readings can amplify the effects of measurement noise at certain frequencies. As noted earlier, the fractional tune readings for red traces are quite reliable before turn number 15, while the blue traces provide good quality readings up to turn 40.

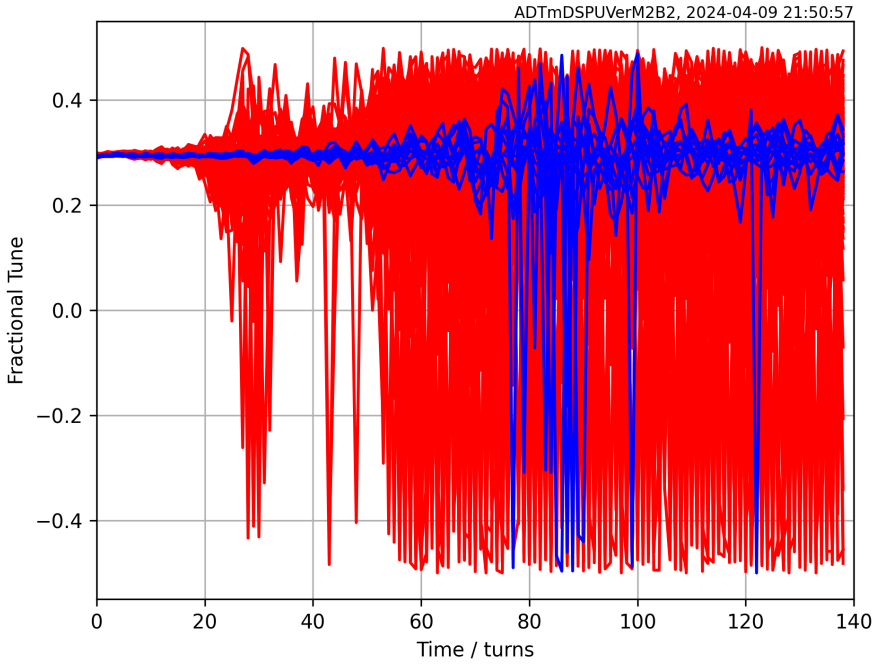

Figure 5.14: Bunch-by-bunch tune estimation from reconstructed transverse phase space. In presence of measurement noise and 0.02σ excitation, 15 and 40 turns of usable data are available for main (red) and witness (blue) bunches.

We can take advantage of this by averaging multiple readings over consecutive turns. This approach further minimizes the impact of random noise, leading to a more reliable estimate with enhanced precision for the resulting parameter reading. In the following Figure 5.15, the fractional tune for each bunch is plotted based on data averaged over 10 turns using the arithmetic mean.

Maintaining the same color coding, the blue dots represent the estimated fractional tune calculated for the Witness bunches. As a reminder, these bunches are intentionally treated by the TFB with a lower feedback gain, allowing the LHC's tune feedback system to effectively extract the fractional tune for the entire machine from these 12 bunches. As can be seen in the figure, the accelerator's tune has been well adjusted to the nominal operation value in the vertical plane, which is 0.295 at injection.

The method proposed in this thesis significantly enhances the ability to extract the fractional tune, which is now possible also for the 2×72 Main bunches (represented by

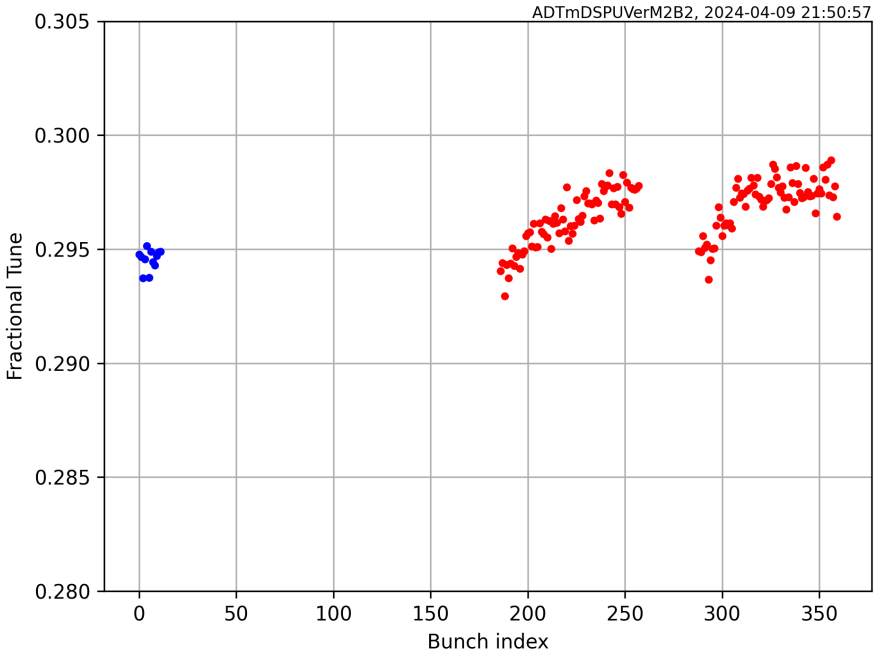

Figure 5.15: Bunch-by-bunch tune data plotted with turn-by-turn data averaged over 10 turns.

red dots). The new signal processing algorithm allows accelerator physicists to visualize features along the bunch trains in a fast, simple and non-destructive manner. Notably, the initial bunches of each 72-bunch train are observed to be close to the set-point value of 0.295, while the bunches located at the end of the train exhibit a tune shift of approximately 0.002. In the context of the LHC, the high beam intensity leads to substantial collective effects, such as impedance and wakefields, which influence beam dynamics (see Section 3.4). As a result, the position of the bunches within the train starts playing a role, with the dynamics of the initial bunches differing from those of the final bunches, thereby causing variations in the fractional tune.

Recommended Feedback Phase

In Figure 5.10, we examine the phase space, where the phase is wrapped within the range $[180°, 180°]$. The beam oscillations recorded by the pick-up advance the phase by the fractional tune with each turn, as shown in Figure 5.14. To account for this effect, we apply a compensation, the results of which are illustrated in the left plot of Figure 5.16. This compensation is described by Equation (4.101) in Section 4.4.2, and we also incorporate the bunch-by-bunch fractional tunes identified in Figure 5.15.

By averaging multiple readings over consecutive turns we enhance the precision of

our measurements. The phase advance between kicker and pick-up, measured for each bunch, is shown in the left graph of Figure 5.15. This data was averaged choosing $M = 10$ turns in Equation (4.102). The color coding is consistent with previous graphs, where blue denotes Witness bunches and red is used for Main bunches.

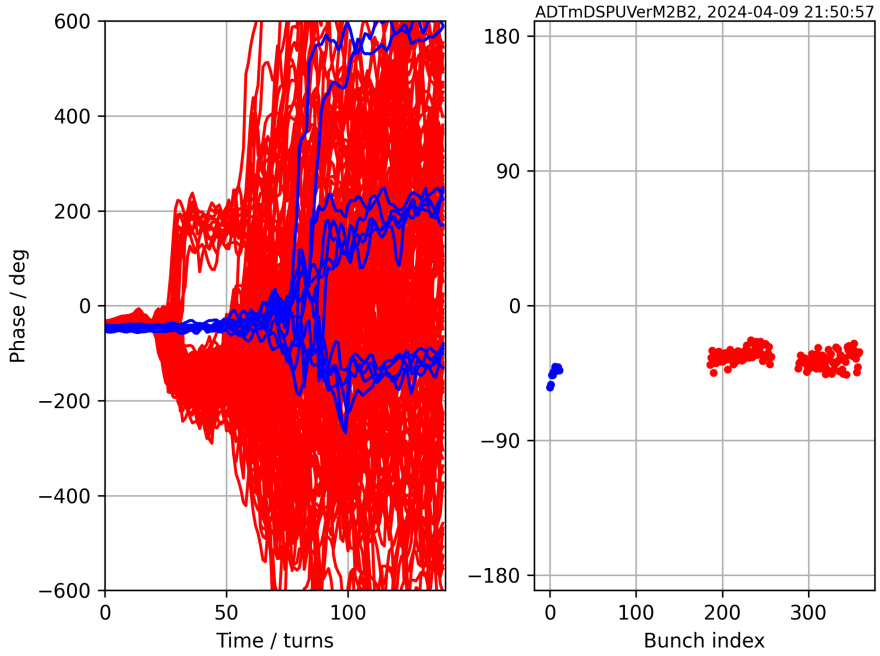

Figure 5.16: Unfolded phase from reconstructed transverse phase space on the left, with phase advance between kicker and pick-up shown on the right using averaged turn-by-turn data over 10 turns.

With the phase advance between the kicker and pick-up extracted from our measurements, we can now determine the recommended TFB phase setting for the pick-up that recorded this measurement. The feedback phase is influenced by both processing delay and group delay, each expressed in terms of the number of turns.

The processing delay refers to the time required for the system to process the signal, which is typically equivalent to a one-turn delay. In contrast, the group delay is defined by the phase rotation algorithm, specifically the time in turns needed to compute the correction based on data from previous turns. Additionally, we must take into account the phase shift introduced by the notch filter, the phase rotation necessary to convert position data to slope, and a $180°$ phase shift to generate a damping correction signal.

By accounting for all these factors in the context of the LHC TFB, we derive the recommended transverse feedback phase, which is the optimal setting for using this

pick-up, as illustrated in Figure 5.17. In this graph, the black horizontal dashed line represents the current phase setting, which aligns closely with the recommended phase for this system.

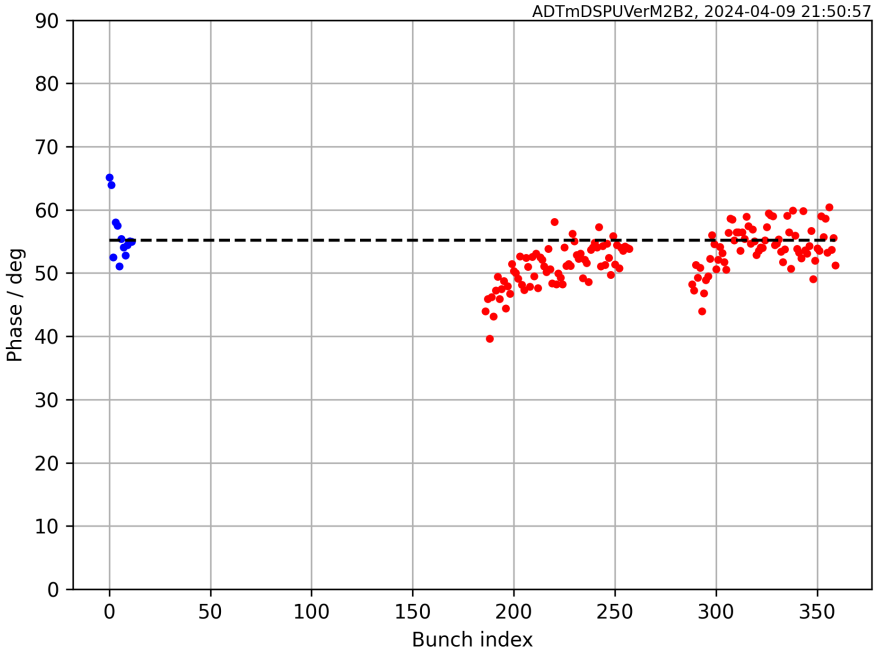

Figure 5.17: Recommended transverse feedback phase using single-turn excitation and beam position data of one pick-up.

In a later step, we can profit from having several bunches generating phase readings, allowing us to derive additional statistics from this data.

A careful examination of the graph presented in Figure 5.17 reveals that the derived recommended phase is not entirely constant; rather, it varies with the the position of the bunches in the trains. This variability is not unexpected, as our investigations have shown that collective effects cause fluctuations in the fractional tune, and therefore would require a slightly different feedback phase. In light of this, it would be beneficial to consider integrating this tune dependence into the signal processing hardware as part of an upgrade scenario. This integration would involve modulating the feedback phase within a turn based on the bucket position of the bunches. This idea seems feasible, as it builds on extending the existing FPGA gateware with the proposed functionality.

Furthermore, it is essential that this feature is adjustable to accurately reflect the actual bunch intensity and filling pattern. To automate this in a practical application, a parameterized model could be employed to calculate the expected tune shift for each

bunch based on its intensity—a variable that is recorded by every beam position monitor and made available as an output signal (see Section 4.1.2).

Building on this concept, if the TFB signal processing allows for modulation of the bunch-by-bunch feedback phase, and if a parameterized model of expected tune shift per bunch intensity is developed, then the TFB could be utilized to actively counteract this tune dependence by deliberately adding a reactive component to the feedback phase. If successfully, this approach could lead to improved performance in accelerators, potentially enabling accelerator physicists to establish a constant tune that remains independent of collective effects. This proposal opens avenues for further research, such as exploring the specifics of the parameterized model, testing its effectiveness in real-world scenarios, and analyzing the implications of the findings.

Multiple Excitations, All Pick-Ups

To verify the signal processing methods introduced in Chapter 4, we evaluated a dataset generated by a single-turn transverse cosine excitation with $N = 1$. As demonstrated, the oscillation amplitude produced by this excitation pattern aligns well with the given filling pattern of 12 Witness bunches followed by two trains of 72 Main bunches. The harmonic wavelet used has no DC component, and its low frequency is advantageous for the LHC's tube-based power amplifier and its capacitive deflector load (see Section 4.1.3). This configuration generates a sufficiently large beam deflection angle during a one-turn excitation.

In order to ensure the effectiveness of our parameter extraction method across various filling patterns, including those with distributed single bunches or multiple batches, we anticipate the need for different excitation patterns. We utilize both sinusiodal and cosine excitation functions, which are DC neutral, and their crest values are phase-align with the zero-crossing of their trigonometric counterpart. By conducting two independent measurements using sinusoidal and cosine excitations, we can generate sufficiently large beam oscillation amplitudes for any given filling pattern.

In Figure 5.18, we compare raw pick-up position data (top row) for the two excitation patterns (bottom row). The graphs illustrate that the waveforms are synchronized, meaning the phases of the two excitation signals are time-aligned to begin at the start of a new turn (the asterisk marks the start of a new turn).

Each measurement is conducted over a duration of $13.1\,\mathrm{ms}$, during which position data from all four pick-ups are recorded simultaneously. From the two excitation mea-

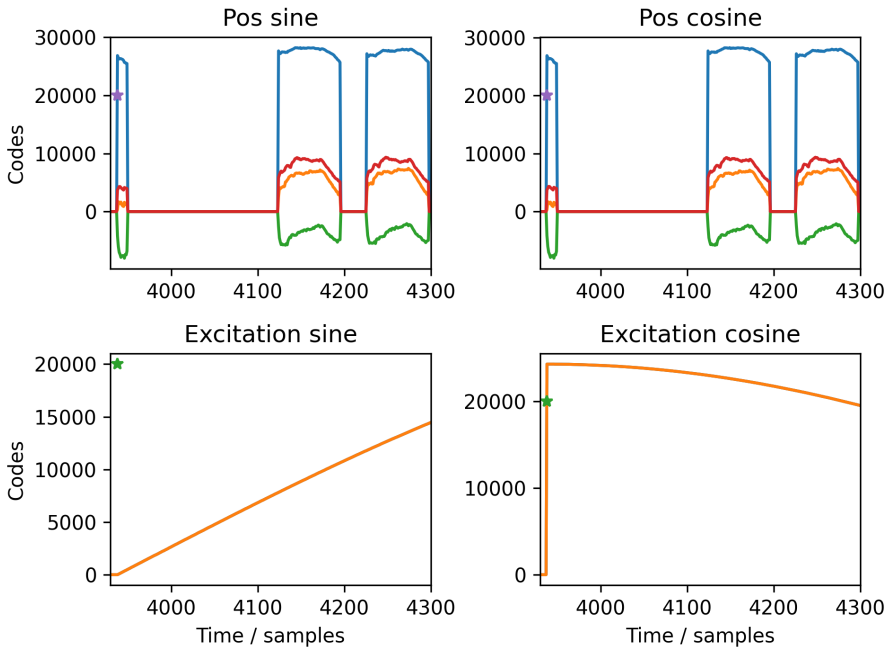

Figure 5.18: Comparison of position data and excitation waveforms.

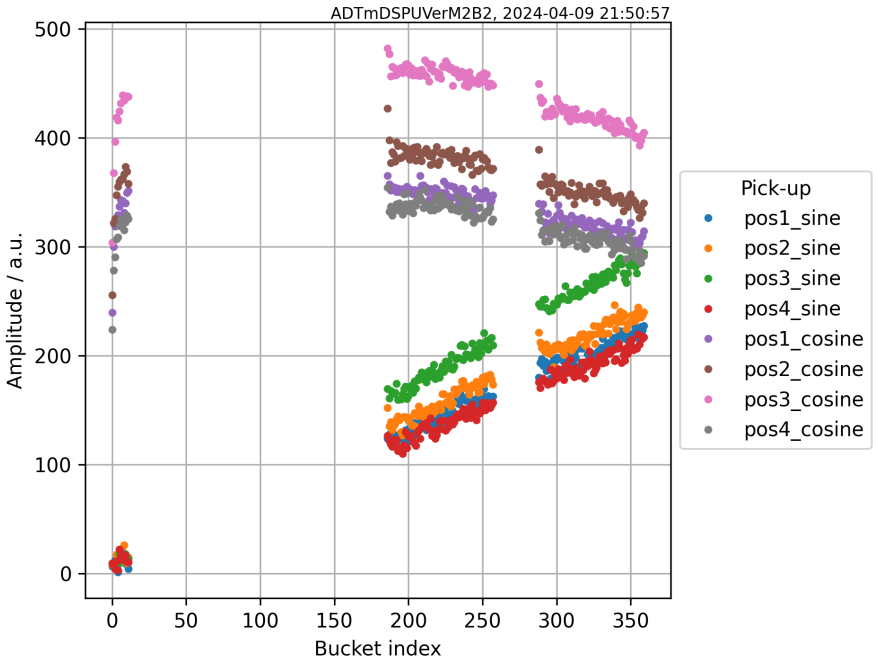

Figure 5.19: Reconstructed oscillation amplitudes per bunch.

surements, we obtain a total of eight datasets (two for each pick-up), which are utilized to reconstruct the transverse phase space. This reconstruction enables us to extract and compare the peak oscillation amplitudes for each bunch, as illustrated in Figure 5.19. It is evident that the sinusoidal excitation does not provide additional insights into the first 12 Witness bunches, as reflected by the observed low oscillation amplitudes. For the later trains, the deflection voltage increases rapidly, resulting in peak oscillation amplitudes that exceeding 100 codes. This amplitude threshold was identified empirically as providing useful data for phase and fractional tune evaluations (see Figure 5.10 on page 98).

By utilizing the additional data obtained from two distinct measurements, we are now able to integrate these datasets to extract the target parameters. The results of our data analysis are presented in Figures 5.20, 5.21, and 5.22. In these figures, each dot represents the estimated value for an individual bunch, with colors corresponding to an specific pick-ups.

The tune estimations for most pick-ups are generally consistent (see Figure 5.20); however, pick-up Q8 (green) appears to slightly overestimate its value.

Figure 5.21 illustrates the recommended feedback phase, with the dashed lines representing the current TFB phase set-points for comparison. The results show a notable degree of agreement with the reference data.

The bunch-by-bunch damping time is presented in Figure 5.22. A comparison of the data from each pick-up indicates a strong agreement across the measurements.

Loop delay measurement method

Ensuring the stability of a Transverse Feedback system requires precise alignment of the kick signal with the arrival times of the bunches. In this section, we will outline the method introduced in Section 4.4.3, which was developed to quantify the kicker delay offset using TFB measurement data.

In Figure 5.18, we introduced multiple excitation signals that exhibit trigonometric properties, forming quadrature signals. We exploit this to construct an IQ-footprint of the traversing bunches at the kicker, as described in Equation (4.104).

The sketch in Figure 5.23 illustrates the relationship between the measured bunch positions at turn n (blue dots), generated by the two excitation patterns with period

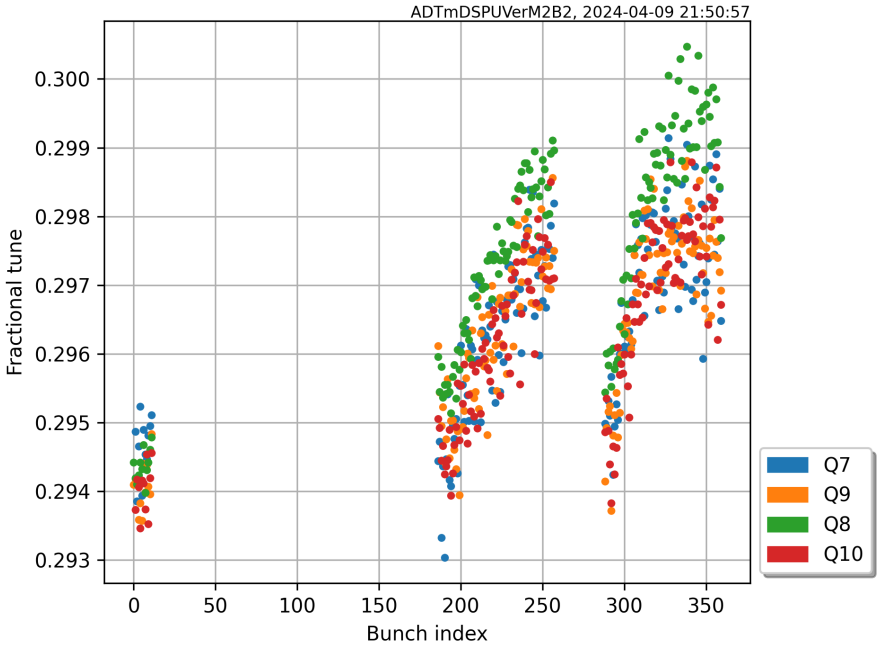

Figure 5.20: Extracted fractional tune per pick-up per bunch.

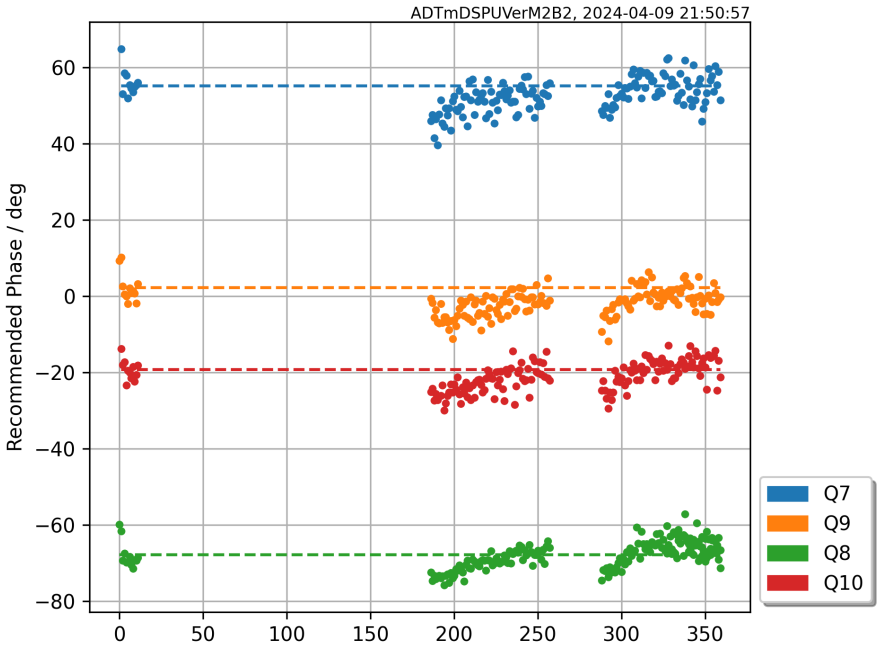

Figure 5.21: Recommended feedback phase per pick-up.

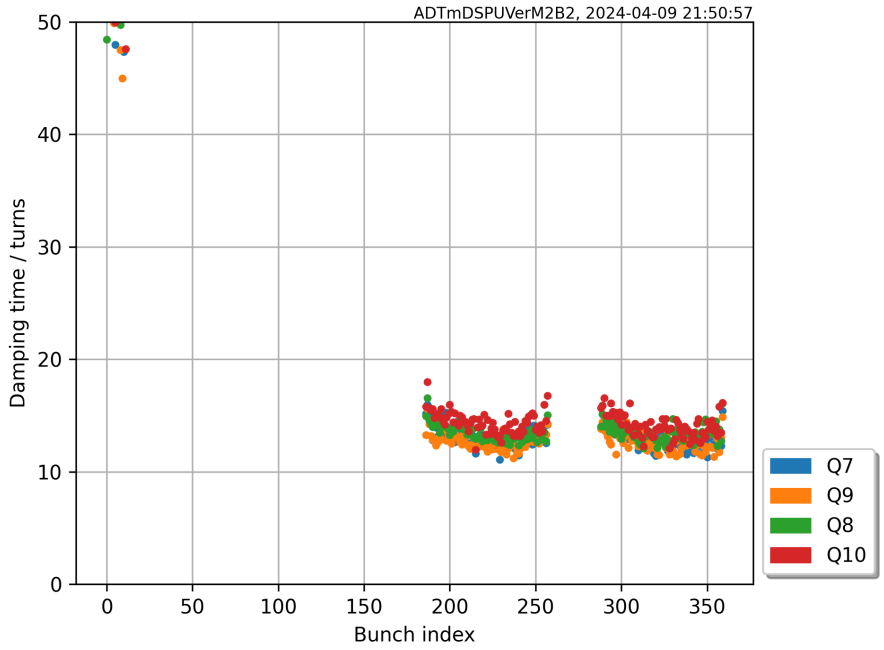

Figure 5.22: Estimated damping time per pick-up per bunch.

$M = 1$ (dashed lines), in Cartesian coordinates. The top graph represents cosine excitation data, the right graph shows sine excitation data, and the central plot displays the projected outcomes.

As shown, the projection of these two signals encodes the time-dependence of each bunch index k as an angular position in the new coordinate system. This relationship becomes even clearer when visualized on a polar grid, as illustrated in Figure 5.24. In this plot, each dot represents the result for one bunch based on two orthogonal excitation measurements. Dots of the same colour indicate data obtained from the same turn, and it is evident that these data points have approximately the same distance from the center.

Equation (4.105) suggests incorporating a linear bunch-index-dependent phase term, which allows us to unwind this phase response and align the results. As shown in Figure 5.25, this alignment produces a straight line. The parameter of interest, the delay offset ΔT, is defined by the orientation, or the phase θ, of this line (see Equation 4.106).

In Figure 5.26, we demonstrate the process of averaging over populated bunches. The dots in this figure represent the mean values of bunch position data at turn n, with colours indicating different pick-ups. To estimate the delay offsets, we fit straight lines through these data points. Additionally, the black dashed rays illustrate the delay error

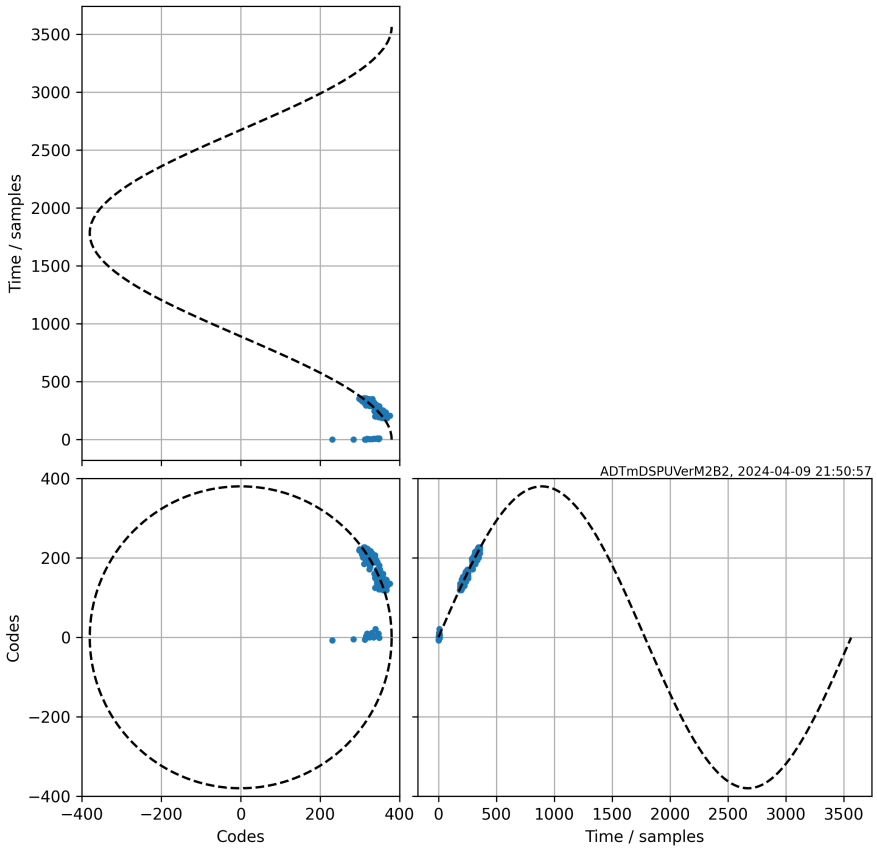

Figure 5.23: Projection of measured bunch position signals.

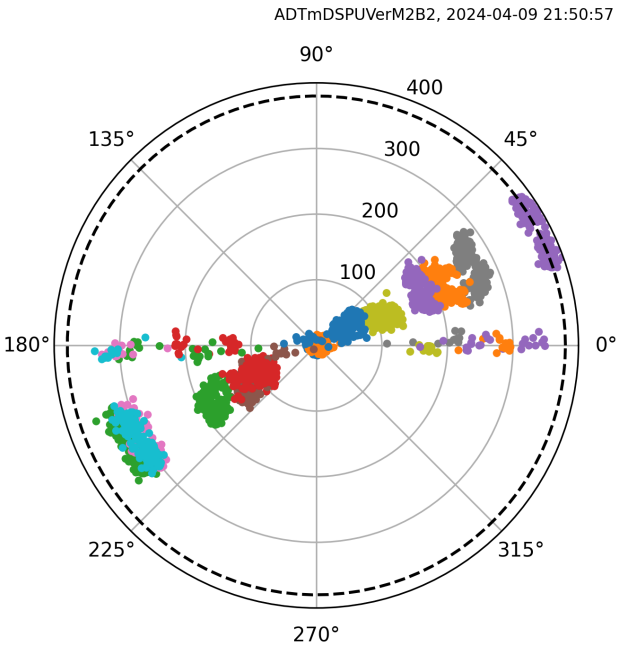

Figure 5.24: Polar grid project of bunch position signals.

associated with the TFB coarse delay, expressed in terms of the number of buckets.

Figure 5.26 identifies two key issues with this analysis. First, the straight lines produced by the fits do not align with the center of the graph, which is a significant concern, as the model does not predict such an offset term. Second, although less obvious, the mean values of the bunch position data are scattered around these straight lines. These observations highlight the need for a careful examination of the recorded input data, as shown in Figure 5.27.

This figure demonstrates that while the mean position has been successfully subtracted, a slow baseline trend has caused the entire curve to appear offset. As a result, the pre-excitation position, which is at code 100, does not align with the horizontal axis. In examining the outcomes of this graph, the incorrect pre-excitation position contributes to the first issue, while the slow baseline trend accounts for the second issue.

It is essential to address these discrepancies by making adjustments to the baseline trend. The blue curve in Figure 5.26 includes a padding of 50 values at the beginning, which allows for the use of a configurable algorithm to estimate the baseline trend estimation, represented by the red curve.

Figure 5.28 illustrates the difference between the recorded position data (shown as a dashed blue trace without padding) and detrended data, which is obtained by subtracting

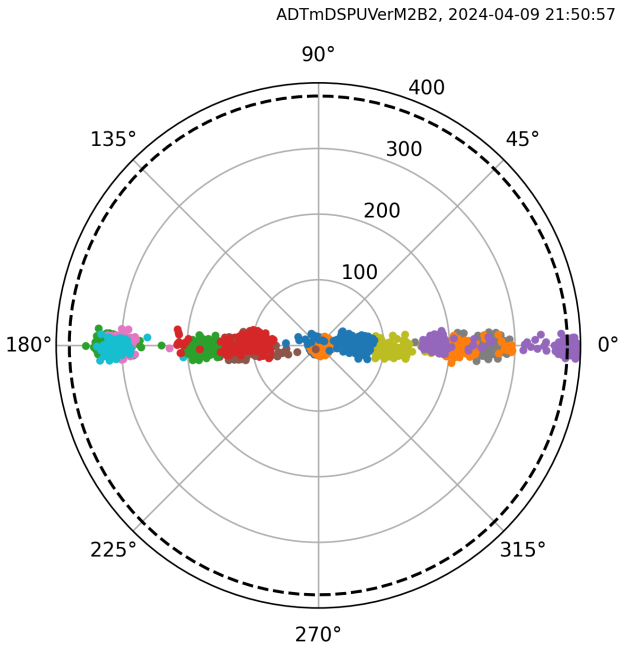

Figure 5.25: Polar grid projection of bunch position signals with bunch-index dependent phase subtraction aligning results as a line.

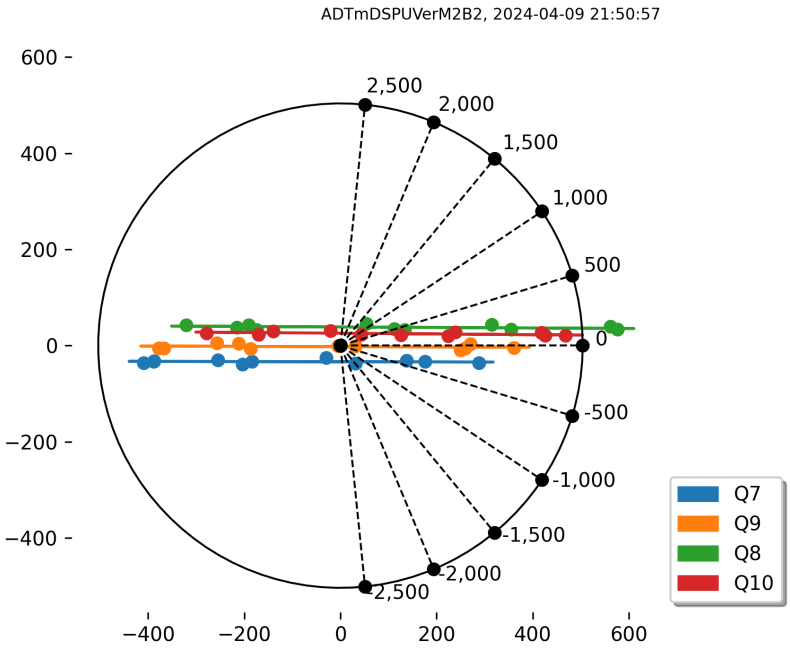

Figure 5.26: Delay data analysis.

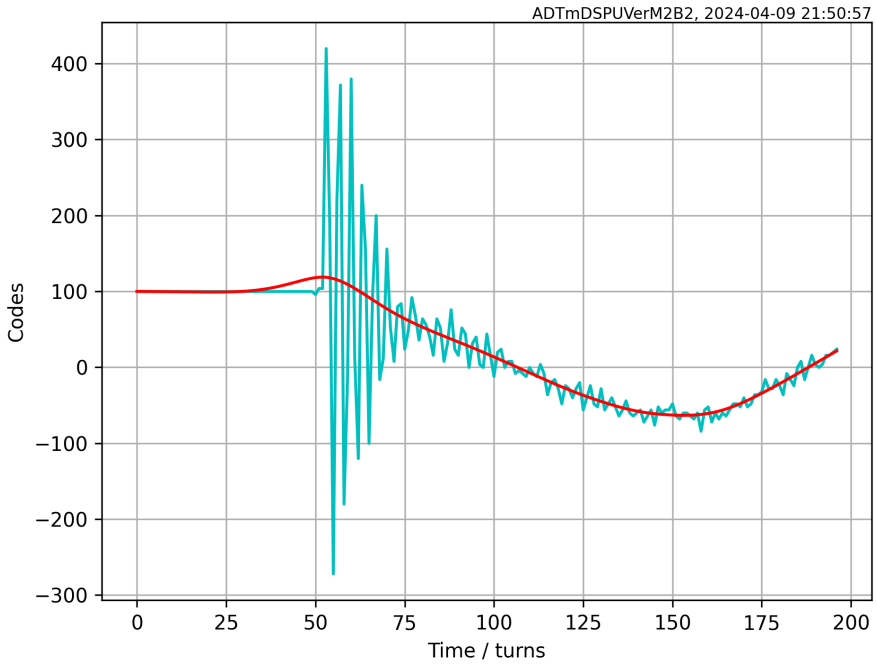

Figure 5.27: Position data with excitation. Average subtracted; 50 values padded. Red curve indicates baseline trend.

the estimated baseline (represented by the black trace).

With this additional processing step, the data for Figure 5.26 can now be adjusted for baseline trends, and the corrected results are plotted in Figure 5.29. The data fits calculated for all pick-ups now align, and based on the obtained phase, we can conclude that the TFB system analysed during this demonstration does not have a significant error in its coarse delay setting.

The coarse delay serves as a fundamental parameter in the TFB's digital signal processing, enabling the storage of per-bunch correction data for retrieval after a specified time interval, referred to as the one-turn delay. This functionality is realized through a First-in First-Out (FIFO) architecture implemented in the FPGA, which operates at three times the bunch rate, specifically at $120\,\mathrm{MSPS}$. Consequently, each increment in the coarse delay setting corresponds to a discrete time delay change of $8.33\,\mathrm{ns}$. The FIFO is designed to be sufficiently large to store an entire turn of data, amounting to $3564 \times 3 = 10\,692$ values.

To further enhance measurement resolution—illustrated by the grid spacing in Figure 5.29, which is defined as $500\,\mathrm{ticks}$—we can manipulate the excitation parameter M. This adjustment leads to an increased sensitivity to delay offsets, a relationship that is

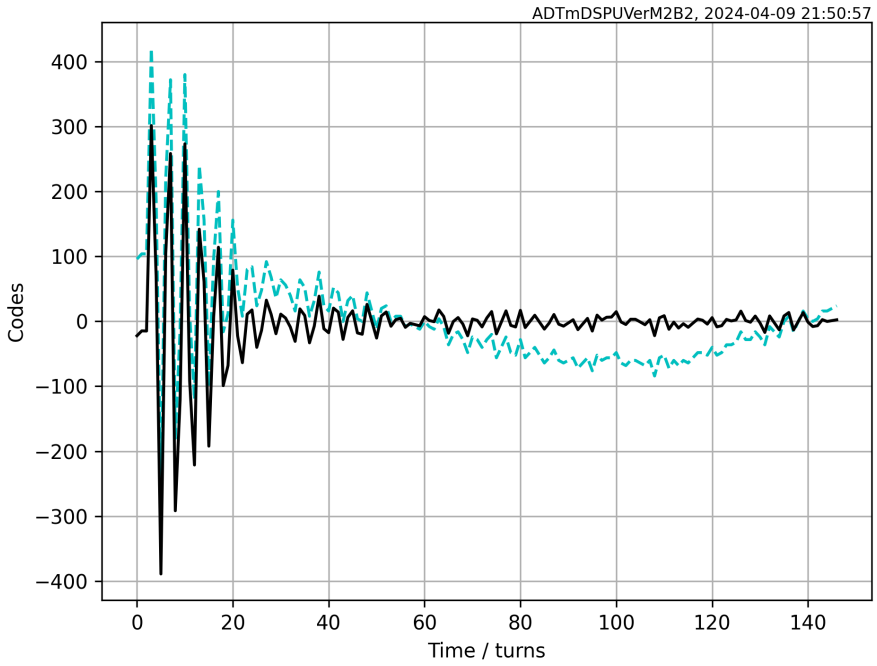

Figure 5.28: Comparison between recorded position data (without padding) and detrended data after subtracting the estimated baseline.

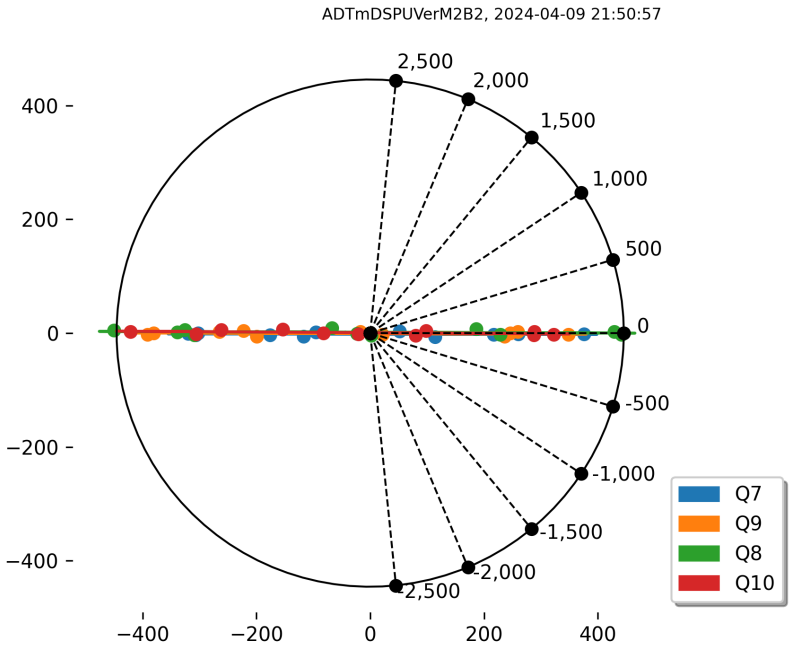

Figure 5.29: Delay analysis after data baseline correction.

formally expressed in Equation (4.107).

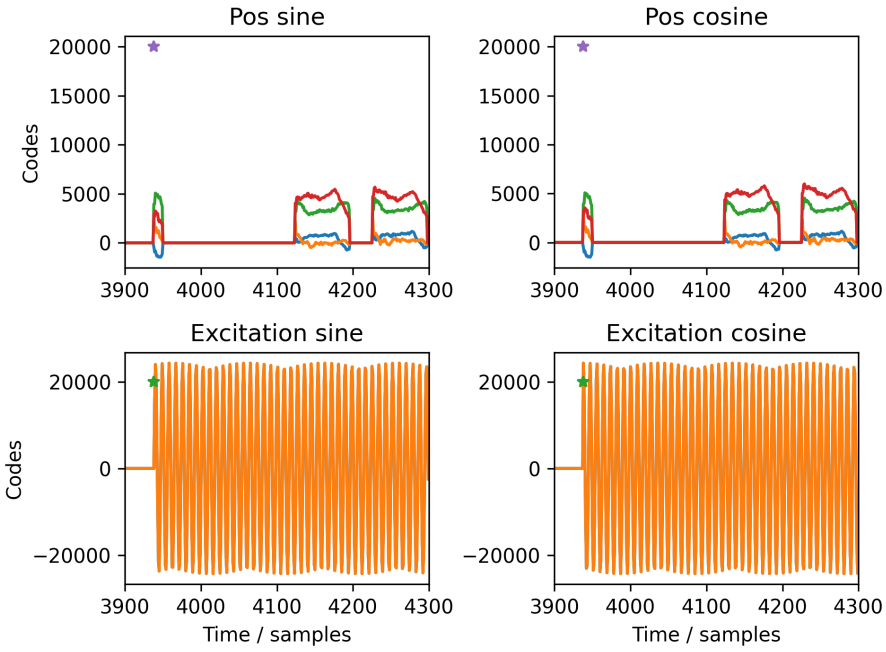

Figure 5.30: Comparison of position data and excitation waveforms for $M = 400$. The asterisk denotes the start of a new turn.

In Figure 5.30, we compare the sampled position data for the witness bunches and two trains from four pick-ups, along with two excitation waveforms for $N = 400$. At this frequency $f_{\mathrm{Exc}} = M/T_{\mathrm{Rev}} \approx 4.5\,\mathrm{MHz}$, the crest values of the sinusoidal and cosine deflections signals alternate within the trains, allowing for increased temporal resolution with the presented algorithm.

The value for $M = 400$ was selected for practical reasons. In contrast, the theoretical maximum value of $M = 3564$ would require the system to generate a waveform at $40\,\mathrm{MHz}$, a frequency that exceeds the design specification of the power system. A Transverse Feedback system must be designed to operate at frequencies up to half the bunch spacing, which is $20\,\mathrm{MHz}$ for the LHC TFB. This choice $M = 3564/2$ would enable a properly time-aligned system to deflect every bunch in an alternating pattern during the cosine excitation, while leaving all bunches unaffected during the sinusiodal excitation, owing to zero crossings of the waveform. A clear disadvantage of this choice would be that, by design, half of the measurements would not provide any additional data - the new information is the absence of data.

When considering the applied kick pattern, a more reasonable value for M would be

$M = 3564/4 = 891$. This choice would enable a properly time-aligned system to deflect two out of four bunches while leaving every other bunch unaffected.

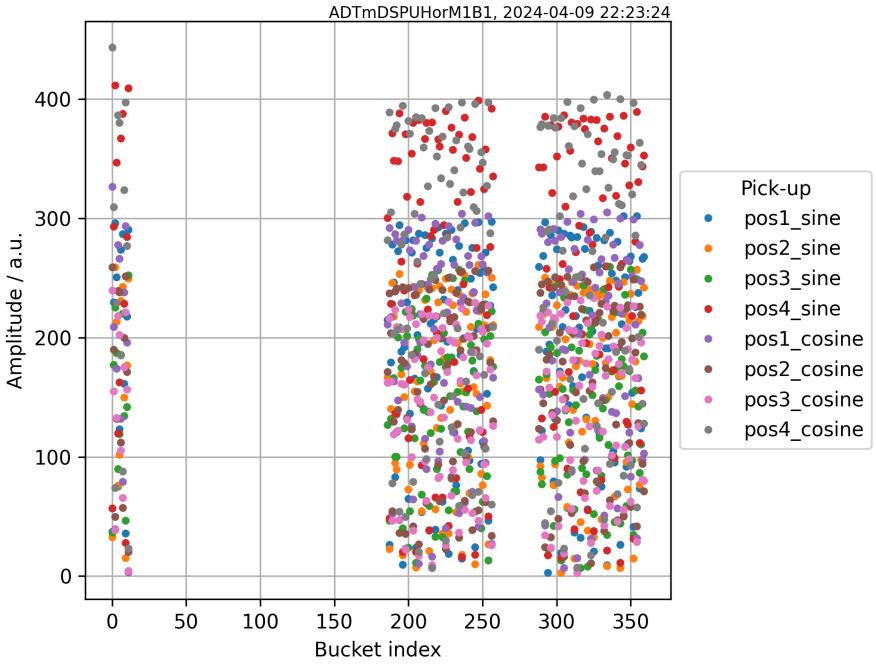

Figure 5.31: Reconstructed oscillation amplitudes per bunch for $M = 400$, with each dot representing data from one pick-up for two excitations, totaling eight amplitude readings per bunch.

The selection of $M = 400$ represents a trade-off between the previously mentioned value of $M = 891$ and the first-order low-pass characteristics of the power system, which exhibits a $3\,\mathrm{dB}$ roll-off at $1\,\mathrm{MHz}$. With the resulting excitation frequency set at $5\,\mathrm{MHz}$, this configuration allows for a suitably effective kick. The performance of this setup is further illustrated by the reconstructed peak oscillation amplitudes shown in Figure 5.31, which indicate that peak oscillations amplitudes exceeding $100\,\mathrm{codes}$ are achieved, while certain bunches within the trains remain close to zero excitation. These results demonstrate that the chosen value of $M = 400$ effectively balances the need for selective bunch deflection while remaining within the operational limits of the power system.

For the delay analysis, each of the two recorded datasets is first baseline-corrected and the results are subsequently plotted in Figure 5.32.

As illustrated in the graph, the grid spacing is now defined as $1\,\mathrm{tick}$, which aligns with our expectation, given that we have refined our measurement sensitivity by a factor

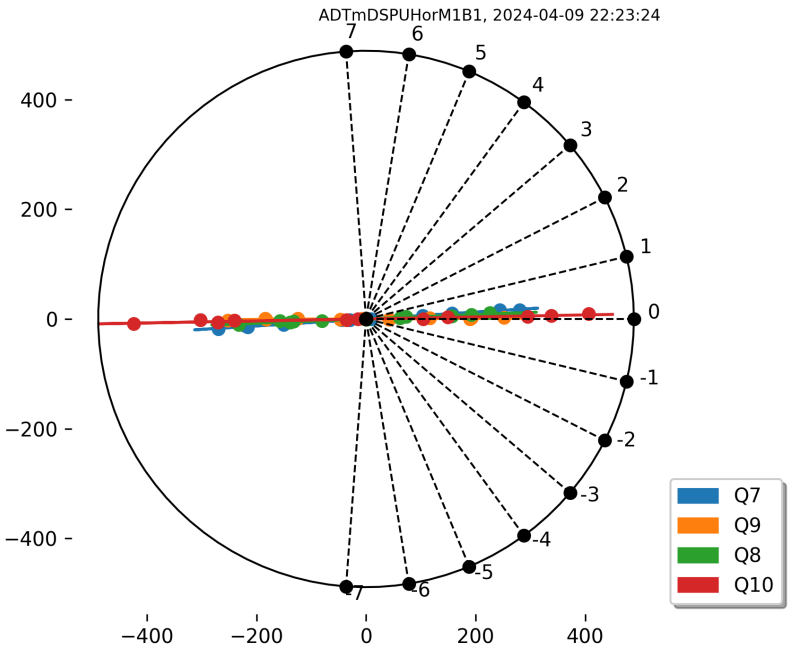

Figure 5.32: Delay analysis for $M = 400$, with rays indicating the delay error in the TFB coarse delay.

of $M = 400$ compared to Figure 5.29, where $M = 1$. This enhanced resolution facilitates straightforward determination of the correct coarse delay setting. For example, in Figure 5.33, the coarse delay was deliberately reduced by $5\,\mathrm{ticks}$, a change that is accurately captured by the signal processing results.

Furthermore, with additional refinement of the graphical representation of the grid spacing, the fine-delay parameter can be adjusted with sub-nanosecond precision. The analysis results presented in Figure 5.34 reflect the modified fine delay setting for this measurement.

5.2.2 Sensitivity analysis of the proposed methods

In the preceding sections, the working principles of the newly introduced methods have been evaluated and demonstrated through comprehensive step-by-step analysis of the measurement results. Build on this foundation, the next critical step is to assess the sensitivity of these methods to variations in key parameters. This section presents a series of detailed measurements in which various parameter settings have been systematically scanned. The objective is to confirm the robustness and reliability of the analysis method, ensuring effective performance under different conditions. By highlighting the sensitivity

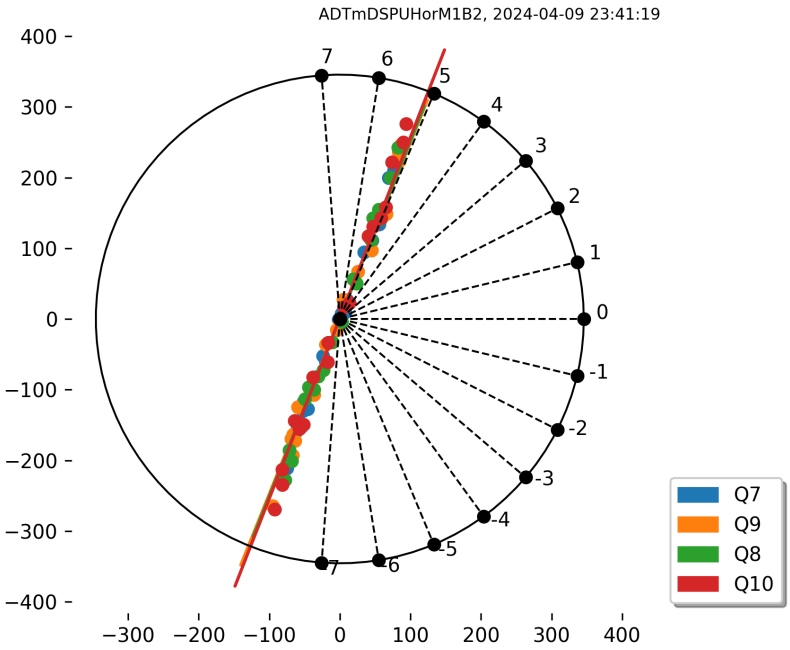

Figure 5.33: TFB coarse delay setting reduced from nominal $10\,490$ to $10\,485$; $M = 400$.

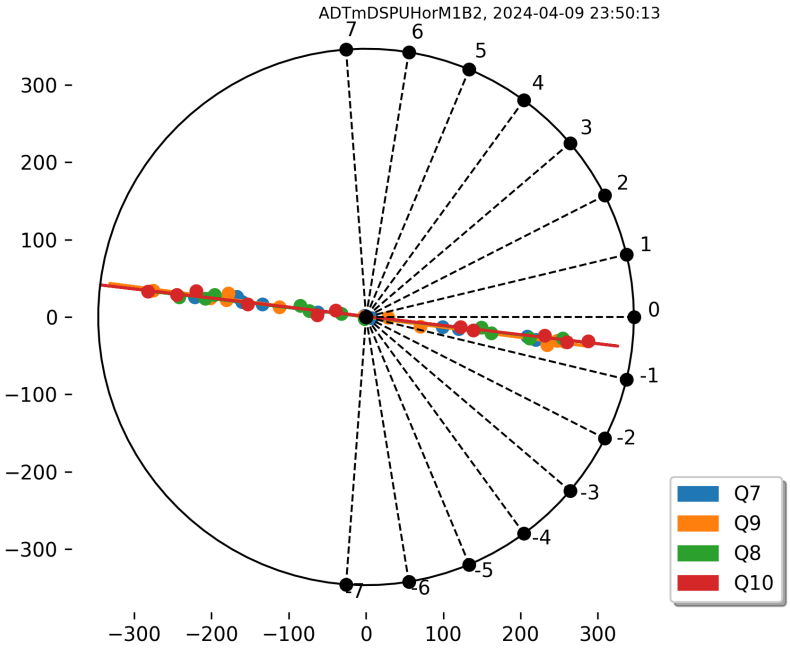

Figure 5.34: TFB fine delay setting increased by $6\,8$ns; $M = 400$.

of the proposed methods, this analysis will provide valuable insights into their practical applicability and potential limitations.

The Transverse Feedback phase scan of a single DSPU, as depicted in Figure 5.35, utilizes the novel parameter extraction method to indirectly measure and extract the recommended TFB phase. The graph presents a comparison between the delta phase and the recommended phase, with both parameters adjusted to the same setpoint value. This analysis is conducted across four different pick-up locations, facilitating a thorough examination of the phase characteristics within the system. By employing this extraction method, the necessary TFB phase information can be derived from straightforward, rapid, and non-destructive measurements. The results illustrated in the figure demonstrate a strong correlation between the parameter scan and the outcomes obtained from the novel extraction method. This alignment indicates that the proposed method accurately reflects the parameter scan, effectively capturing the underlying phase characteristics. Such consistency not only validates the reliability of the extraction technique but also reinforces its potential for accurately measuring and analyzing TFB phase information in practical applications.

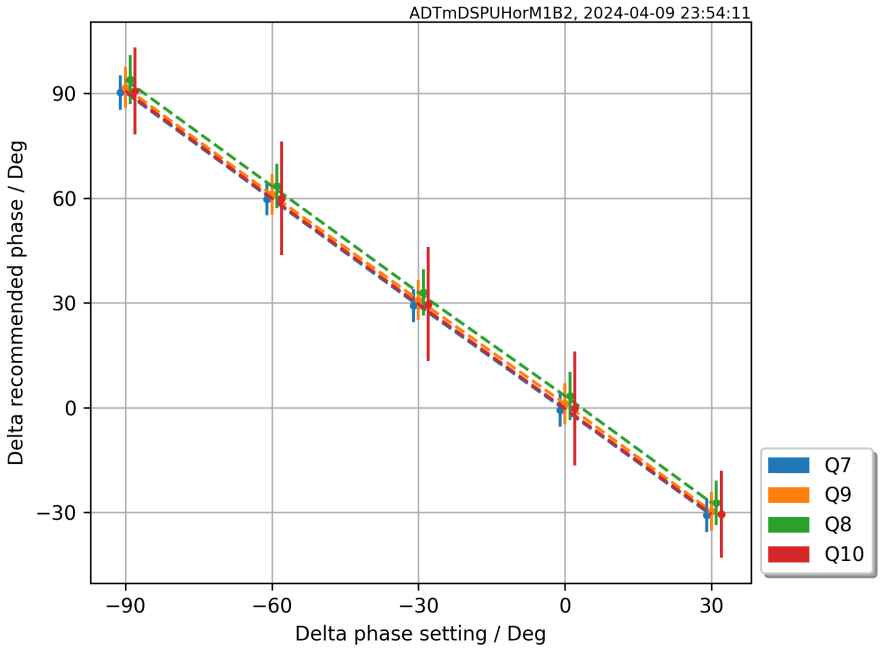

Figure 5.35: TFB phase scan of a single DSPU: Delta phase compared to recommended feedback phase, both adjusted by the same setpoint value, for four pick-ups.

For the study illustrated in Figure 5.36, we conducted a coarse delay scan of a single Digital Signal Processing Unit to evaluate the novel delay extraction method. This scan

involved adjusting the delay settings by ±5 slots around the designated setpoint, allowing for a comprehensive assessment of the method's response. The results were analyzed for algorithm-derived delay changes at the four pick-up locations. By comparing the adjusted delay settings with the changes evaluated by the algorithm, we aimed to validate the effectiveness of the extraction method and its capability to accurately capture the dynamics of the delay adjustments. The proposed method effectively captured the delay changes, as evidenced by the results presented in Figure 5.36. This alignment confirms that the method accurately measures and reflects the underlying delay characteristics.

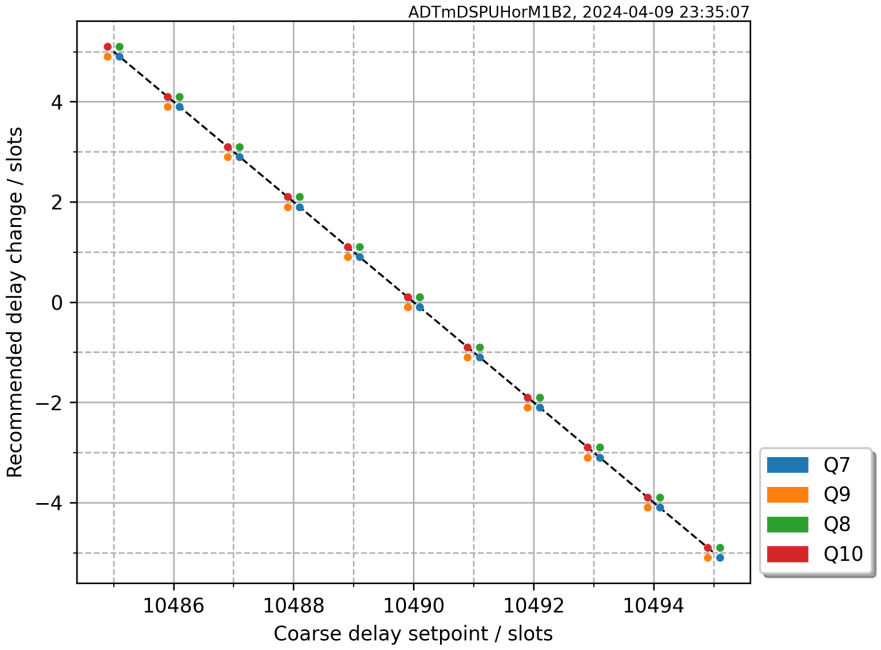

Figure 5.36: Coarse delay scan of a single DSPU: Delay settings adjusted by +/- 5 slots around the setpoint vs the algorithm-evaluated delay changes for four pick-ups.

In the fine delay scan of a single DSPU shown in Figure 5.37, the delay chip setting was systematically adjusted from 0 to 10 nanoseconds in increments of 1 nanosecond. This approach allowed for a detailed examination of the relationship between the applied delay settings and the corresponding algorithm-derived recommended delay values. In the graph, the results of this scan for each pick-up are visually represented by colored dots, with a straight black dashed line indicating the targeted linear relationship between the delay settings in nanoseconds and the recommended values provided by the algorithm.

The results obtained from the fine delay scan demonstrate a linear relationship that correlates well with the manually adjusted delay values. This linearity indicates that

the delay extraction method effectively captures the intended adjustments made to the delay chip. However, a notable discrepancy in the slope of the relationship suggests that there may be imperfections inherent in the delay chip itself. These imperfections could arise from various factors, such as manufacturing tolerances, component aging, or environmental influences, which may affect the precision of the delay settings. As a result, while the overall trend remains linear, the deviation in slope highlights the need for further investigation into the characteristics of the delay chip.

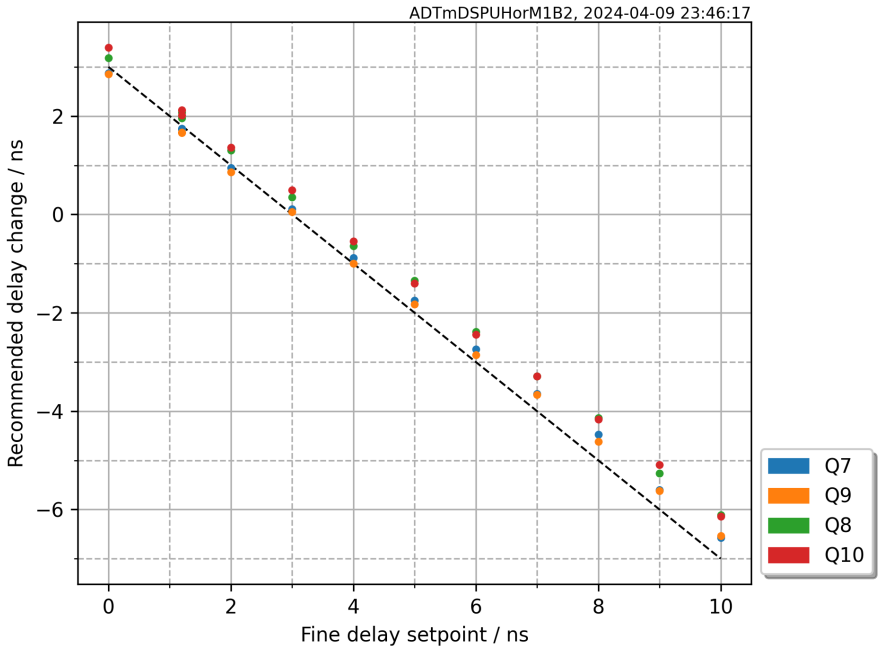

Figure 5.37: Fine delay scan of a single DSPU: Delay chip stepped from 0 to 10 ns in 1 ns increments, compared to algorithm-derived recommended delay settings. The straight black dashed line outlines the linear relationship between the delay chip in nanoseconds and the recommended settings.

Figure 5.38 presents an adjusted plot that incorporates the delay chip correction factor, derived from the specifications outlined in the manufacturer's data sheet. This correction factor is essential for refining the accuracy of the delay settings, as it accounts for known deviations and imperfections associated with the delay chip. By applying this correction, we aim to enhance the alignment between the measured delay values and the recommended settings provided by the algorithm. The adjusted plot not only illustrates the impact of the correction factor on the overall delay response but also serves to validate the effectiveness of the delay extraction method in capturing the true dynamics of the system.

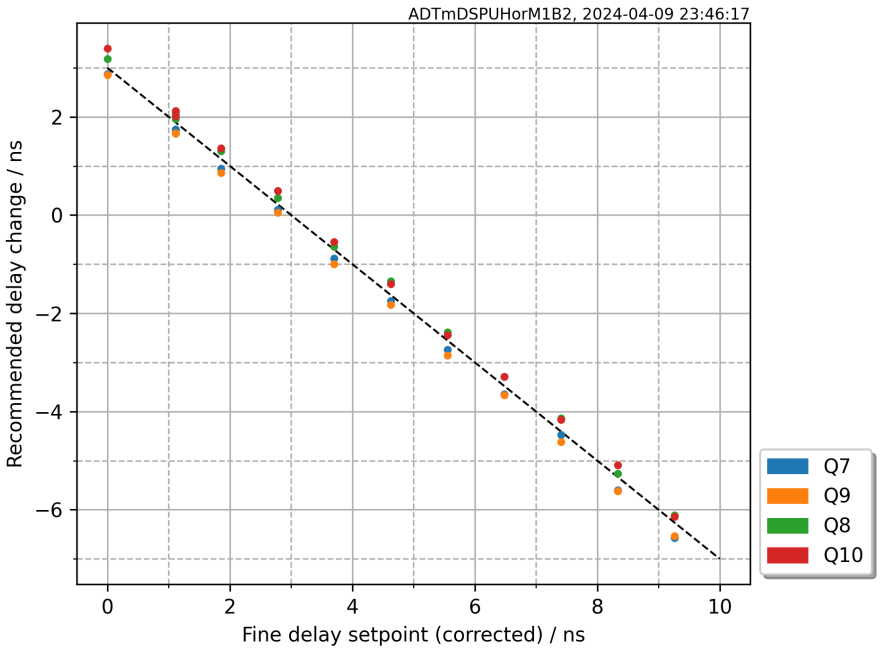

Figure 5.38: Adjusted plot with delay chip correction factor based on specifications from the manufacturers data sheet.

5.2.3 TFB parameter measurement results

Following our detailed examination of the analysis algorithm and its sensitivity to parameter variations, this section applies the novel methods introduced for extracting essential TFB to evaluate the current performance of the system and identify potential areas for optimization. Specifically, we will analyse closed loop gain, feedback phase, and loop delay across the two distinct TFB gain regions, referred to as Main gain and Witness gain, as previously described.

Each plot presents a comparative analysis of results obtained for each pick-up, beam, module, and plane, with data from each each pick-up distinctly color-coded for clarity. In every graph, we present the mean value derived from a series of measurements, accompanied with the corresponding Root Mean Square (RMS) values, which are also color-coded to align with the respective pick-ups. The black lines indicate the minimum and maximum values of the data samples, providing insights into the measurement spread and highlighting any outliers. Through this analysis, we will discuss the performance of each DSPU system, explore potential causes for deviations from nominal behavior, and identify opportunities for optimization. In all graphs the first module of Beam 2, vertical plane was offline and could not be used for data evaluations.

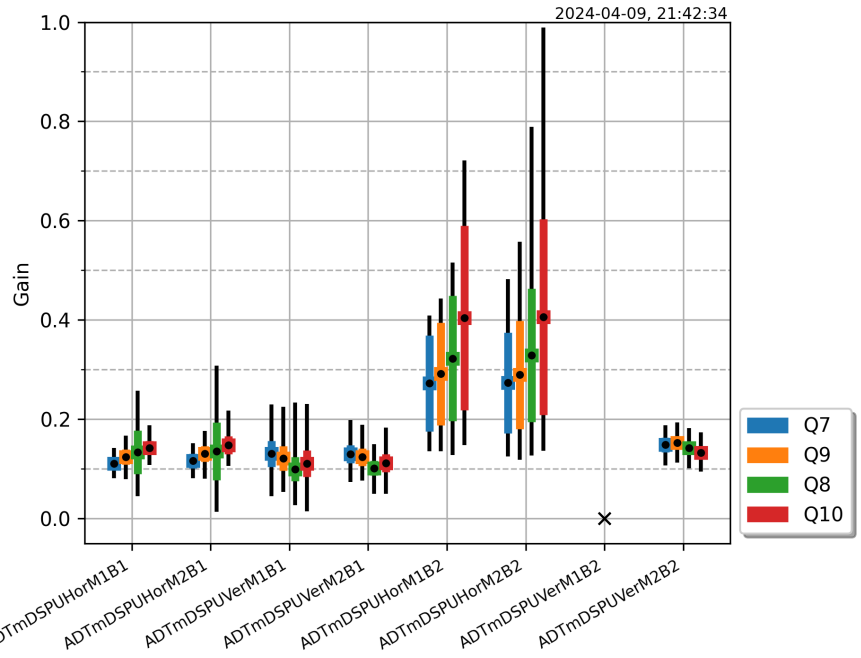

Figure 5.39: Comparison of ADT closed loop feedback gain, measured for Main Gain bunches and excitation M=1.

Figure 5.39 presents a comparison of the closed-loop feedback gain measured for Main bunches with excitation set to $M = 1$. The plots indicate that all modules for Beam 1 are operating within a gain range of 0.1 to 0.2, which is consistent with the performance observed for the second DSPU module for Beam 2 in the vertical plane. Notably, the majority of the pick-ups exhibit relatively small scatter in the Root Mean Square (RMS) values and peak excursions, suggesting that the obtained results are close to the true values. However, an outlier is observed in the horizontal pick-up Q8 for Beam 1, which displays a significantly larger RMS scatter and substantial peak excursions in the measurements. Given that data from this pick-up is shared between the two concerned DSPUs, the similar results observed in these measurements imply that the issue may be related to the Beam Position Module of this pick-up or its settings.

Furthermore, a clear deviation from the nominal gain parameter is evident for both horizontal modules of Beam 2, with mean values approximately in the range of 0.3 to 0.4, accompanied by a considerably larger scatter as indicated by the RMS values. A careful examination reveals that both modules exhibit similar measurement data for the same pick-ups. It is important to note that these data are obtained through independent measurements conducted by each DSPU individually, suggesting that the observed phenomena may be related to a common factor affecting both modules.

Additionally, it is noteworthy that the loop gain is typically set by the operations group to achieve a target damping time. This indicates that these value were intentionally configured to a higher-than-usual setting. Further analysis is required to fully understand the underlying causes of these deviations and their implications for system performance.

Figure 5.40 illustrates the closed-loop feedback gain measured for Witness Gain bunches with excitation set to $M = 1$. Overall, the loop gain for these bunches is lower, typically in the order of 0.05, with the exception of Beam 2 horizontal, where the measured gain ranges between 0.07 and 0.08. Notably, the horizontal pick-up Q8 for Beam 1 exhibits a similar signature to that observed in the Main Gain analysis, characterized by large peak excursions and a comparably increased RMS spread. This consistency in behavior across different gain settings raises concerns regarding the performance of this pick-up.

Further investigations are warranted for both the Q8 pick-up in Beam 1 and the horizontal module of Beam 2 to determine the underlying causes of these anomalies and to assess their impact on overall system performance.

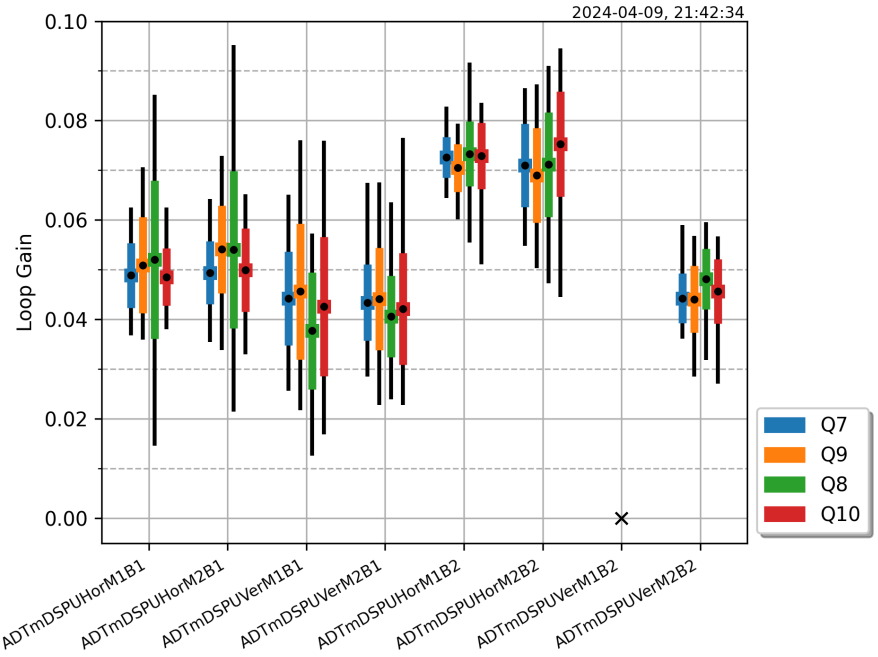

Figure 5.40: Comparison of ADT closed loop feedback gain, measured for Witness Gain bunches and excitation M=1.

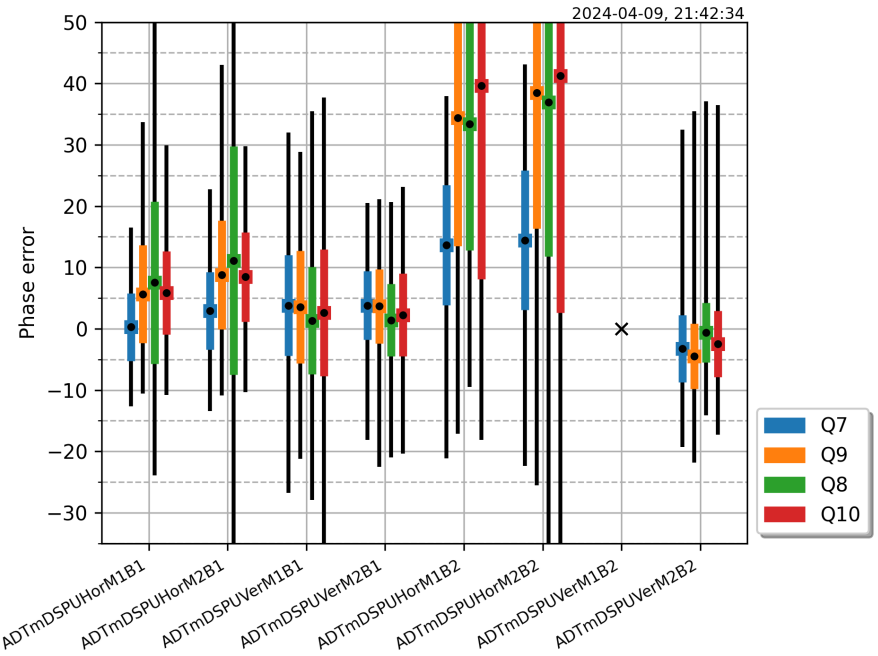

Figure 5.41: ADT feedback phase error analysis, measured for excitation M=1.

Figure 5.41 presents the analysis of the ADT feedback phase error measured for excitation set to $M = 1$. The graphs illustrate the phase error for each pick-up, comparing the current set point to the recommended phase setting determined by the signal processing algorithm. For the TFB systems operating Beam 1, there is overall very good agreement, with phase errors not exceeding 10 degrees and an RMS spread of only 5 degrees. However, an exception is noted for the horizontal pick-up Q8 of Beam 1, which exhibits a significant RMS spread of nearly 20 degrees and a phase error exceeding 10 degrees for module 2.

In the case of Beam 2, the typical candidates for concern are both horizontal modules. The data for pick-up Q7 indicates a phase error of 15 degrees, while the other three pick-ups show phase errors closer to 40 degrees. The latter measurements display an RMS spread of more than 20 degrees, suggesting potential issues with the data quality of the measured input.

Conversely, DSPU Ver2M2B2 demonstrates satisfactory phase settings, with all four pick-ups exhibiting phase errors of less than 5 degrees, and a standard deviation of around 5 degrees.

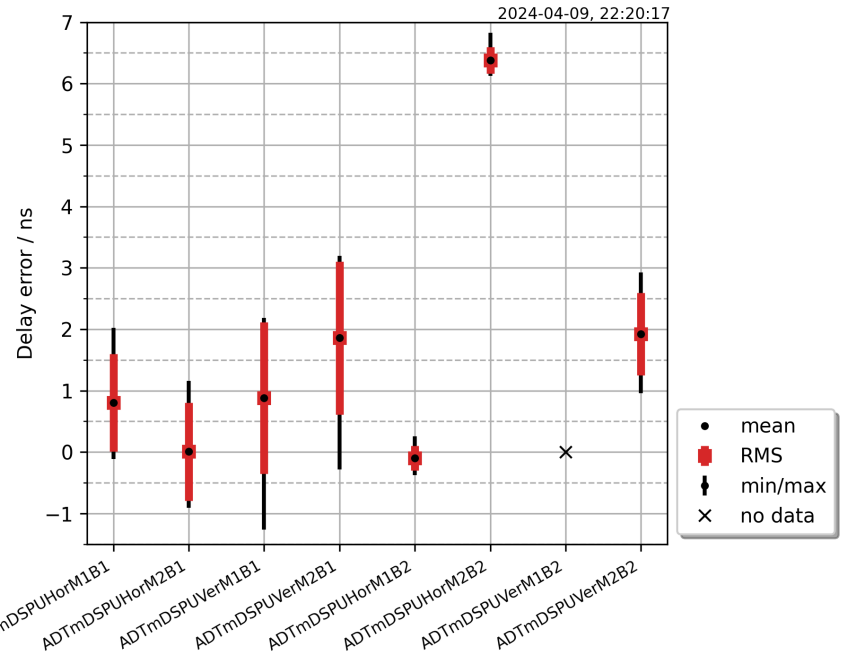

Figure 5.42: ADT fine delay error. Excitation pattern M=400.

Figure 5.42 illustrates the fine delay error in nanoseconds for each TFB system, with the excitation pattern set to $M = 400$. It is important to note that the delay error is

related to the kicker timing, so individual measurements for each pick-up are combined to form the overall result.

for Beam 1, the delay errors are within acceptable limits, not exceeding $2\,\mathrm{ns}$. Three out of four pick-ups show errors better than $1\,\mathrm{ns}$, and one pick-up has nearly zero delay error. However, the standard deviation, as well as the minimum and maximum errors, are around $1\,\mathrm{ns}$, indicating that the measurement distribution may not conform a Gaussian profile.

Interestingly, both modules in Beam 2 Horizontal show remarkably high data quality, with RMS values well below $0.25\,\mathrm{ns}$. The delay setting for DSPU HorM1B2 is nearly optimal, while HorM2B2 has a delay error of $6.3\,\mathrm{ns}$, which is significantly off target. It is important to remember that a delay error leads to a phase error. For the highest coupled bunch mode of $20\,\mathrm{MHz}$ in the LHC, this corresponds to $360^\circ \times 20\,\mathrm{MHz} \times 1\,\mathrm{ns}$, or 7.2 degrees per nanosecond. Consequently, the delay error for HorM2B2 results in a phase error of 45 degrees at $20\,\mathrm{MHz}$. This significant phase error could lead to challenges, particularly when the TFB is required to counteract coupled bunch oscillations. If one module is not properly adjusted, it will attempt to dampen these oscillations but may divide its action into two components: resistive and reactive. The reactive component could inadvertently shift the fractional tune of the already oscillating bunches

In this context, we have two redundant TFB modules operating on the same beam, both aiming to stabilize it. However, with differing system settings and parameters, these modules may compete with one another. Ideally, the performance of a well-adjusted module could help compensate for some imperfections in the other module. Overall, while the combined function of both modules may still provide damping, it is likely to be less effective than a system configured with optimal settings.

5.2.4 Accelerator parameter measurement results

In this section, we extend the analysis of TFB parameters previously conducted by employing the signal processing techniques outlined in the methods chapter to extract vital accelerator parameters from measurements. The focus will be on two key parameters: bunch-by-bunch damping time and bunch-by-bunch fractional tune, both of which are vital for assessing the performance and stability of the accelerator.

In line with the previous section, we will provide a detailed analysis for both Witness bunches and Main bunches, adhering to the same formatting conventions to ensure clarity and coherence throughout the measurement results.

It is important to note that data for the DSPU Beam 2 Vertical Module 1 is unavailable, as this module was offline during the measurement period and could not be utilized. The subsequent discussion will present the extracted parameters and explore their implications for the overall performance and stability of the accelerator system.

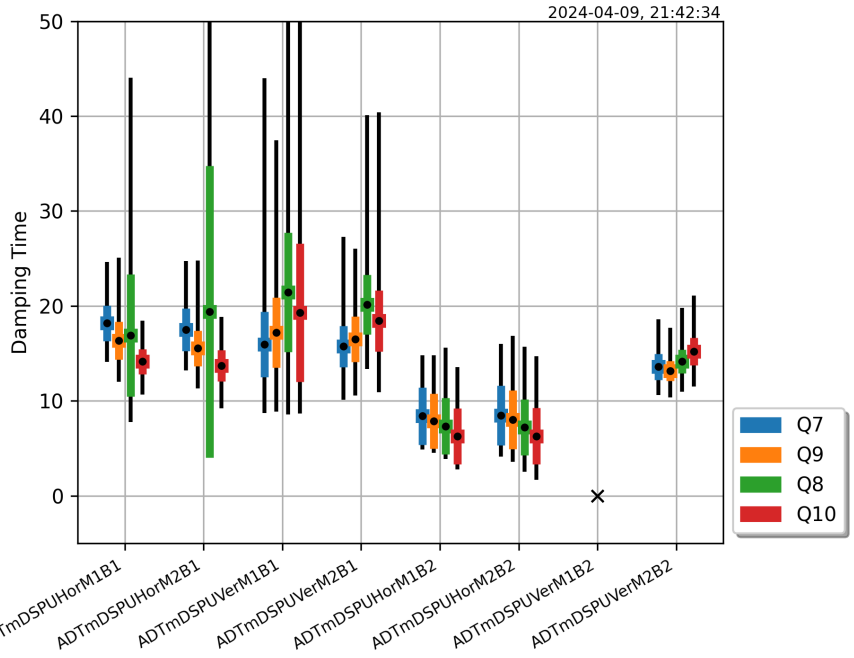

Figure 5.43: Comparison of damping time parameter for Main bunches, excitation M=1.

Figure 5.43 presents a comparison of the damping time parameter for Main bunches with excitation set to $N = 1$. The data for Beam 1 indicates that the Main bunches are consistently damped within approximately 15 to 20 turns, based on the assumption that the oscillation amplitude follows an exponential decay. The damping time measurements

for all modules were conducted with one module operating in open loop and the other in closed loop mode.

Among the recorded measurement samples, pick-up Q8 of Beam 1 in the horizontal plane exhibits a siginficantly larger standard deviation compared to the other pick-ups. This is consistent with our previous observations, suggesting that the greater variability may be due to data quality issues of the Beam Position Module.

In contrast, the two horizontal modules of Beam 2 demonstrate notably higher performance, achieving damping times below 10 turns. In this regime, the TFB exerts a strong influence on the beam; however, it is important to note that such strong damping can lead to overdamping, which is generally undesirable. Overdamping may adversely affect beam stability and overall performance, making it imperative to evaluate the time evolution of the oscillation amplitude.

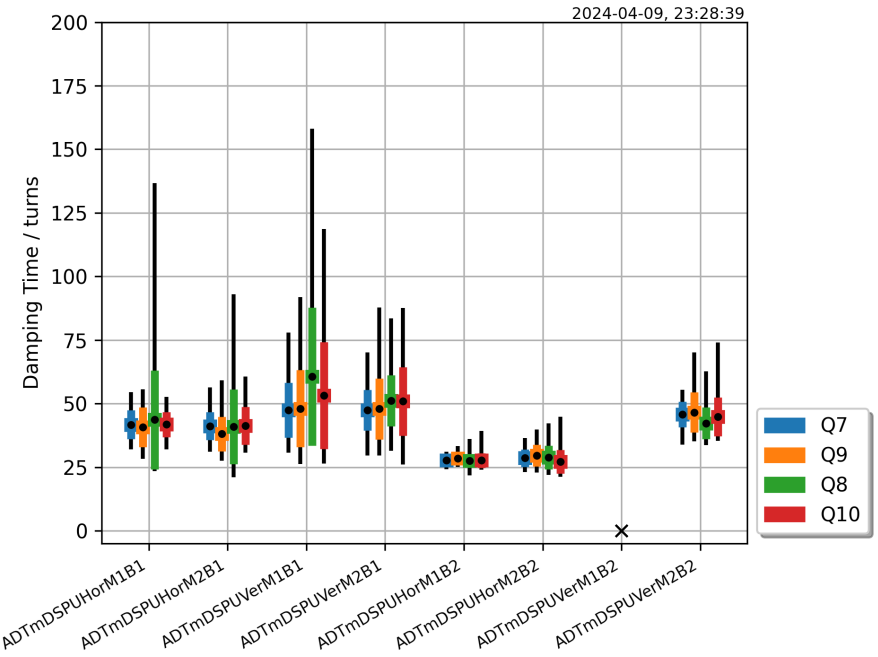

Figure 5.44: Comparison of accelerator damping time parameter for Witness bunches, excitation N=1.

Figure 5.44 presents a comparison of the accelerator damping time parameter for Witness bunches with excitation set to $M = 1$. The damping times for the Witness bunches are observed to be in the range of approximately 40 to 50 turns. This analysis indicates that the damping times for Witness bunches are notably longer compared to those of the Main bunches, which is an expected and intentional behavior. This extended

damping time facilitates the LHC's BBQ system in accurately detecting the fractional tune in the presence of a strong transverse feedback system.

However, an exception is noted in the horizontal plane of Beam 2, where both modules exhibit significantly shorter damping times, close to 25 turns.

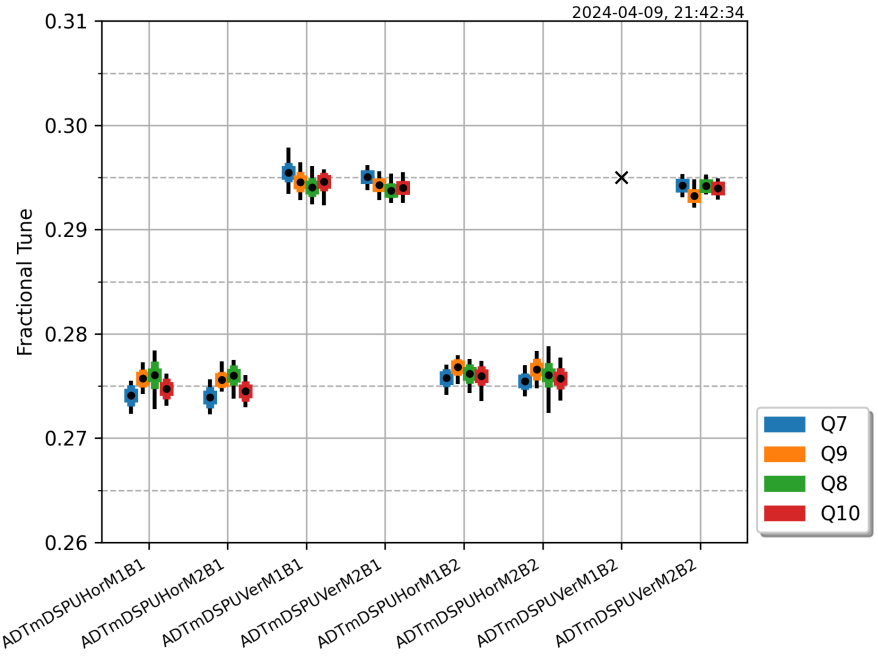

Figure 5.45: Evaluation of accelerator fractional tune parameter for Witness bunches (excitation M=1).

Figure 5.45 presents the evaluation of the accelerator fractional tune parameter for Witness bunches with excitation set to $N = 1$. The results obtained from this analysis highlight the effectiveness of the novel algorithm employed to measure the fractional tune using only a limited number of turns of observation data. Notably, the measurements exhibit very little scatter, with RMS values well below 0.001, demonstrating remarkable precision in detecting the fractional tune.

The reduced TFB gain for these bunches further enhances the measurement results, allowing for more accurate readings. The machine appears to be correctly adjusted for the nominal fractional tune values, which are 0.275 in the horizontal plane and 0.295 in the vertical plane. This alignment with the expected values underscores the algorithm's capability to accurately capture the fractional tune.

Figure 5.46 presents the evaluation of the accelerator fractional tune parameter for Main bunches with excitation set to $M = 1$. Consistent with the results obtained for

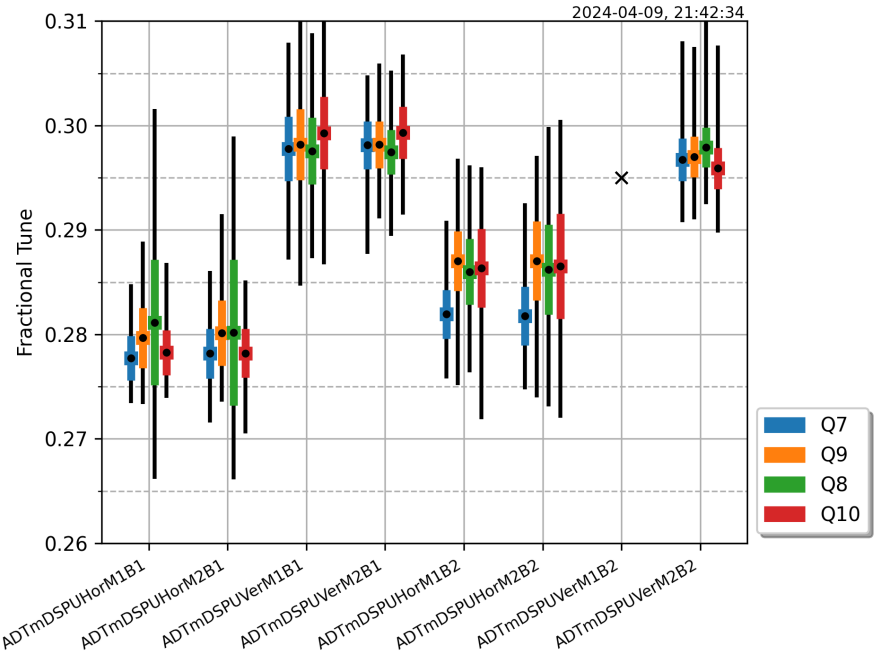

Figure 5.46: Evaluation of accelerator fractional tune parameter for Main bunches (excitation M=1).

the Witness bunches, a distinct separation between the horizontal and vertical tunes is observed. The measured tune values for these high-intensity trains indicate a positive tune shift of approximately 0.005 when compared to the values recorded in the low gain region. Furthermore, the RMS values of 2.5×10^{-3} confirm the good resolution of the measurements.

The mean fractional tune values extracted from four different pick-up datasets per DSPU are closely aligned, which is desirable since these pick-ups are intended to measure the same property of the beam independently and at different locations within the machine. However, an exception is noted in Beam 2 in the horizontal plane, where three out of four pick-ups report similar mean values, with a significant tune shift to 0.287, while the expected value, as indicated by the Witness bunches, is 0.275. The fourth pick-up, Q7, displays a notable deviation, with a delta value of -0.005, leading to a tune estimation closer to 0.282. This atypical data raises concerns, as all pick-up acquisitions are triggered by the same excitation pulse, and the betatron tune oscillations (the number of oscillations per turn) for this beam are expected to be consistent across measurements.

The irregularity observed in pick-up Q7 of Beam 2 in the horizontal plane is supported

by two independent measurements from DSPU module 1 and DSPU module 2. One possible explanation for this discrepancy may be a misconfiguration of the corresponding beam position module. Therefore, further investigations into the DSPUs for Beam 2 and their associated Beam Position Modules in horizontal are recommended to address these anomalies.

5.3 Extraction of vital accelerator parameters in real time

The reconstructed phase space of the circulating beam allows to extract in real time the transverse activity of each individual bunch. Of large interest for the machine operation is the oscillation amplitude and its evolution over time. After the method was introduced [100] a very primitive proof of principle application (shown in Figure 5.47) was presented to the LHC operations group.

The demonstrator quickly became an operational tool, where a detailed transverse activity of the beam can be observed through the whole cycle. This method and the resulting tool actually changed the view on how the LHC should be operated. Some of the transverse instabilities at particular points in the machine cycle, which were originally expected by the accelerator and beam physics group have not developed. And at the same time, an increased transverse activity had been observed where it was not expected at all, triggering investigation on the possible sources and mitigations.

Figure 5.48 shows a detail of transverse activity for one 48-bunch train circulating in the slots 1570 to 1618. The actual transverse oscillation amplitude is in order of $1\,\mu\mathrm{m}$, but an excess of $40\,\mu\mathrm{m}$ was recorded as a consequence of the injection kicker waveform leakage to the turn.

Figure 5.49 shows a peak activity of all bunches during one full LHC machine cycle. The injection started at around 8:20, the energy ramp around 8:50, the top energy was reached shortly after 9:00. The two beams were put into collisions shortly after, this is where the transverse activity diminishes due to the stabilizing effect of the colliding beams.

Figure 5.50 shows another application, used operationally in the LHC control centre. The plots show bunch by bunch damping time and tune, extracted from the injection

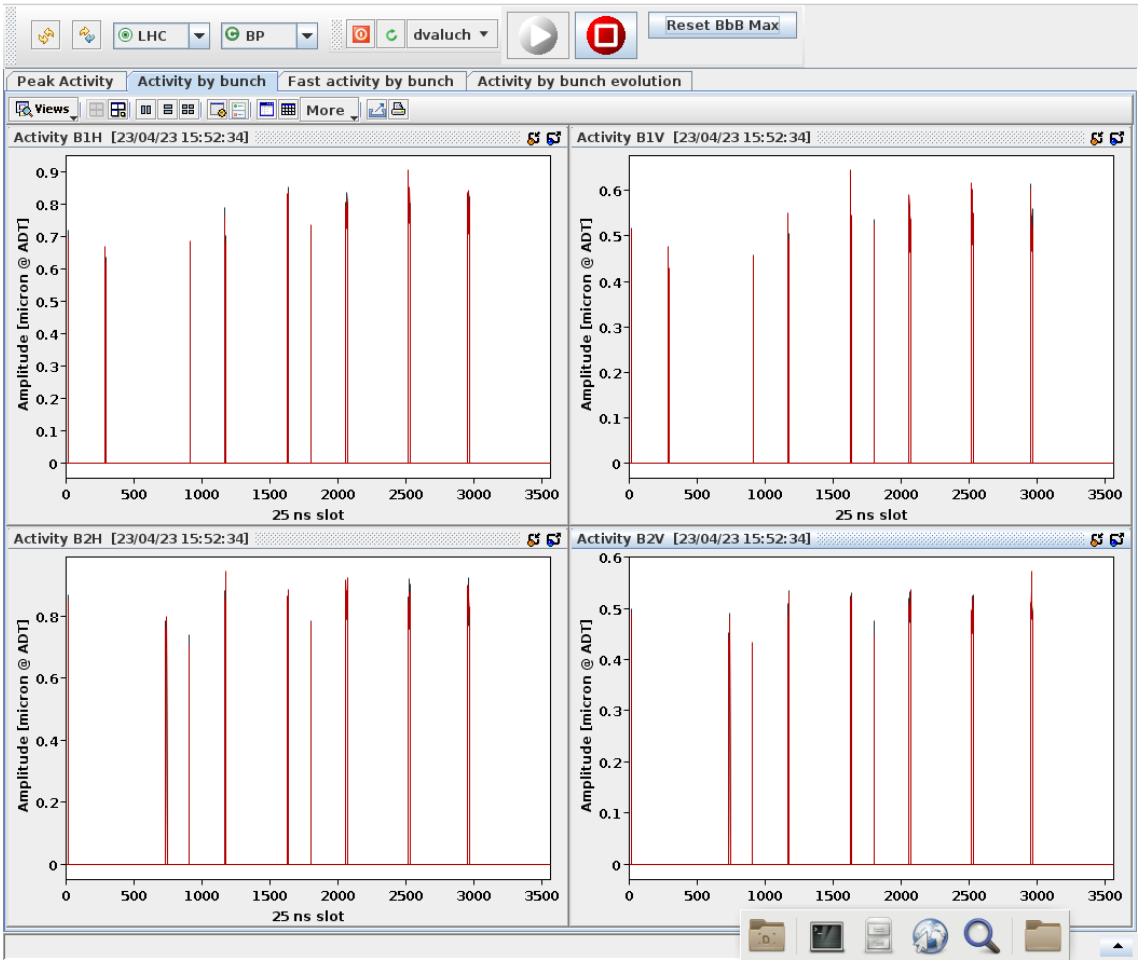

Figure 5.47: Display application for real time transverse activity monitor used in LHC

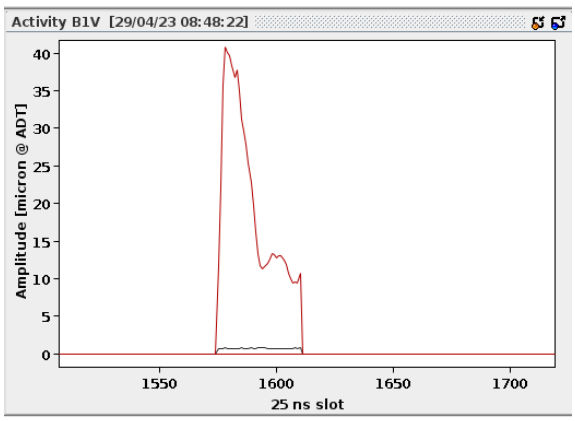

Figure 5.48: Detail of a real time transverse activity for one 48-bunch long bunch train

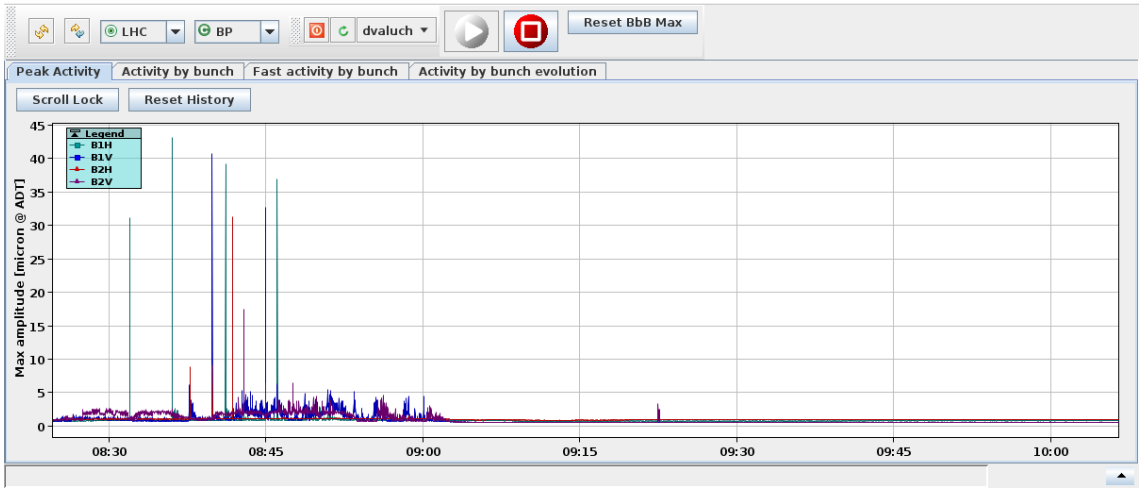

Figure 5.49: Overall transverse activity through one LHC fill.

oscillation transient. It provides a quick check if the TFB is operating properly (Is the damper damping? question). The application is extremely useful at the LHC restart after a long technical stop, or a shutdown. Provided the LHC TFB pickups are properly set-up, what is usually the case, the operators will instantly get the tune value of the virgin machine which was just powered up, from the very first few turns the beam will make in the LHC. The beam does not even need to be captured yet, it is sufficient if it makes as few, as 3-5 turns before it debunches and the tune value can be measured by the TFB. The operators immediately have the initial tune value and quickly calculate and apply the tune correction. The next injection is already very close to the nominal. This saves hours of precious machine time at every start up.

5.4 Digital filter design to reduce tune dependence

In this section, we present the findings related to Objective #5, which focuses on the development of advanced signal processing techniques aimed at enhancing the robustness of transverse feedback systems in the context of tune variations. Our emphasis is on Finite Impulse Response methods, specifically tailored to address the challenges posed by frequency-dependent phase variations.

As any regulation loop, the TFB signal processing chain is constrained by the accuracy of external parameters like the phase margin, gain margin, and stability of the loop delay. In an accelerator, those parameters are often changing with the machine parameters, like

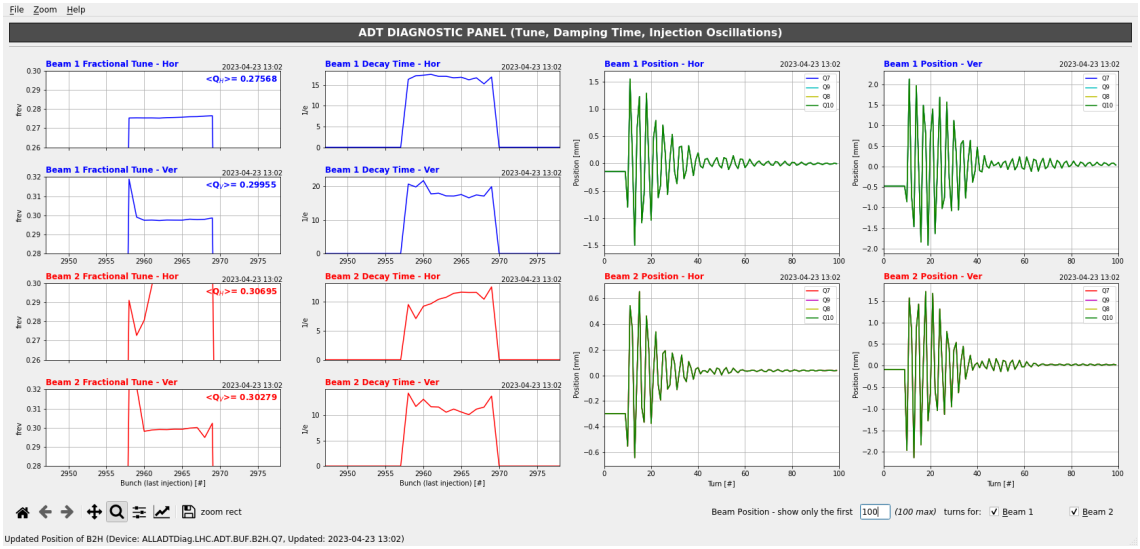

Figure 5.50: Display application showing extracted machine parameters (tune) and transverse feedback parameters (damping time) in LHC

tune variation or hardware changes like tetrode burn out and aging. Aim of the objective #5 is to design a new signal processing scheme, or filters, which will reduce dependence of the TFB performance on external parameters variations. The priority is to relax the tune dependence. The LHC, when in collisions, is operated with a large bunch by bunch tune spread. The feedback must be able to treat all bunches equally to prevent unwanted selective emittance growth, or trigger an onset of transverse instability for certain bunches.

As presented in [101], the introduced beam model of transverse oscillations in equation (4.25) allows numerical evaluation of the analytic expressions for the described phase adjustment possibilities. We use root locus plots to study the evolution of the beam's closed-loop poles at selected frequencies, $\omega_0 = 2\pi Q_f$, and as a function of the feedback gain.

Considering equation (4.78) for the use with arbitrary fractional tunes: the same Pick-up Vector Sum algorithm 4.76 as for the two pick-up case can be applied for a single pick-up at subsequent turns, as outlined in Fig. 5.51. In this case we define $\phi_1 = 0$ and $\phi_2 = 2\pi Q_f$, to be used with Eq. (4.76) respectively Eq. (4.77).

Figure 5.51 suggests that by considering a notch filter using $h[n] = [1, -1]$ the phase shift between $y_k[n]$ and $p[n]$ can be carried out by a short FIR, with the filter coefficients resulting from

$$y_k[n] = b_1 p[n] + (b_2 - b_1)p[n-1] - b_2 p[n-2]\,. \tag{5.4}$$

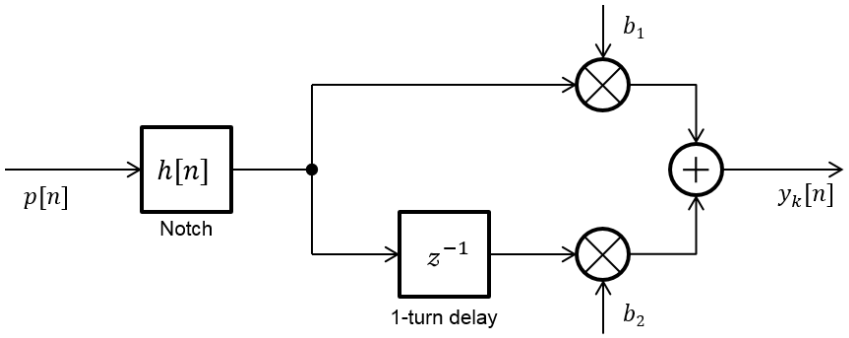

Figure 5.51: Block diagram of temporal phase shift.

With only three taps and including a notch for DC-orbit suppression Eq. (5.4) describes the shortest possible digital filter. The design has two parameters, the fractional tune Q_f and a free parameter ϕ_k which allows for direct phase adjustment.

Optionally, improved noise suppression can be achieved with zeros added at $z = \pm 1$, which can be absorbed into the notch filter, $h[n]$, including an extra phase term, $\Delta\vartheta = -\pi Q_f$ into Eq. (4.77) for every additional tap the notch filter is extended.

The three plots in Fig. 5.52 detail a portion of the upper right quarter of the complex z-plane. As an example closed-loop pole trajectories for the SPS vertical plane are shown, assuming a fractional tune of $Q_f = 0.18$ and variations of up to ± 0.04 (blue,solid). Their origin is at the unit circle (black, bold solid) for zero loop gain (corresponding to the undamped open loop response). By increasing the feedback gain the damping time reduces gradually until the trajectories cross the circle at $|z| = 0.95$ (red, dashed) which is the design value of the SPS TFB corresponding to 20 turns. For as long as a trajectory points towards the origin of the z-plane (black, dash-dotted lines) it will follow the desired closed loop negative feedback of $-180°$.

Figure 5.52(a) shows the beam response for a standard FIR Hilbert phase filter, using seven taps for the case of the SPS TFB. As can be seen this filter is working perfectly fine at the target tune of 0.18, however, the feedback phase appears to be sensitive to tune variations, with the active feedback adversely pushing the tune further away the more its value deviates from the desired value. This effect is attributed to the constant group delay of the FIR filter causing the feedback phase to be optimum only for a single frequency and to roll off quickly for long filters.

The shortest possible digital filter including a notch for DC-orbit suppression will only include three taps. The design has two parameters, the fractional tune Q_f and a free parameter ϕ_k which allows for direct phase adjustment. Shortening the FIR filter length

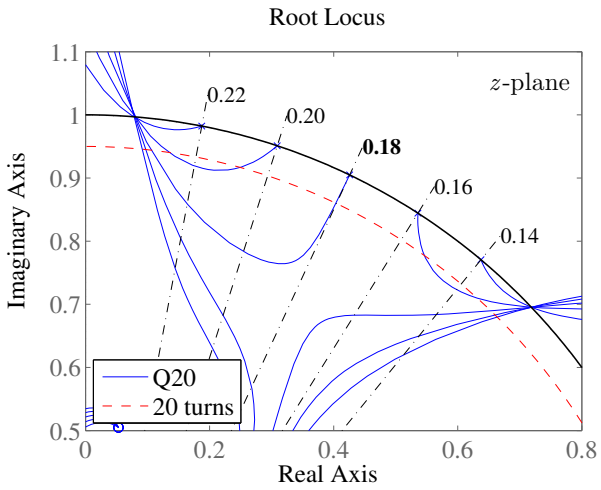

(a) Standard Hilbert phase shifter.

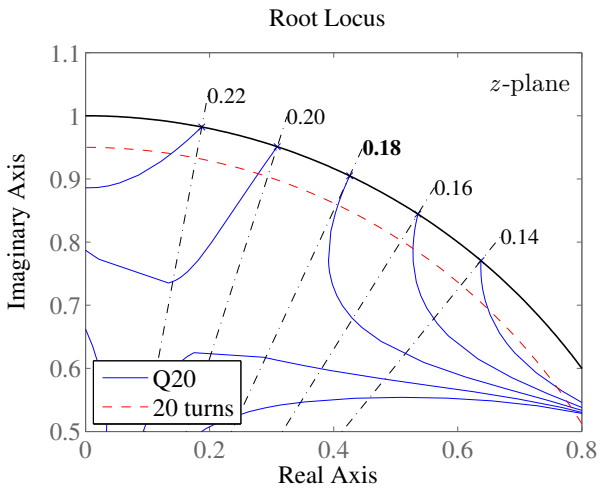

(b) Short 3-tap FIR filter.

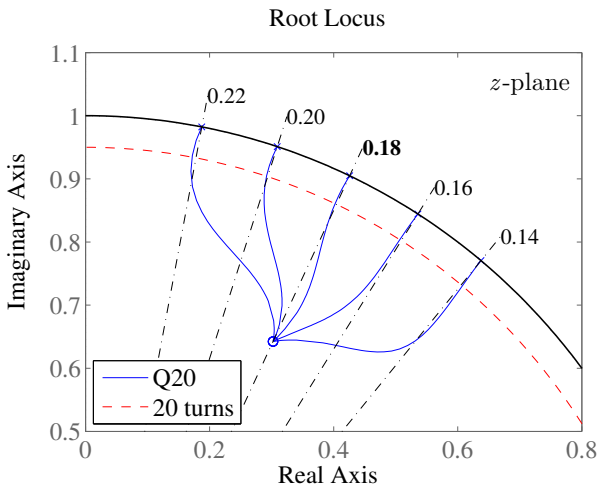

(c) Group delay compensated.

Figure 5.52: Root locus plots, fractional tune $Q_f = 0.18 \pm 0.04$

to only 3 taps, has a positive effect on tune variations, as can be seen by inspecting Fig. 5.52(b), with the closed loop response remaining stable over a larger range of tune values.

By anticipating that the group delay — a measure for linearity of the phase — introduced by a filter lowers the stable phase margin of a closed loop system we made an attempt to compensate this effect by introducing an additional pair of conjugate complex zeros, $c_{1,2} = \zeta e^{\pm j\omega_d}$, at the desired tune frequency, $\omega_d = 2\pi Q_f$, which adds negative group delay as a function of the magnitude, ζ. The group delay as specified in Ref. [92] follows for a direct-form FIR transfer function as

$$\tau(\omega) = -\sum_{k=1}^{M} \frac{|c_k|^2 - \Re\{c_k e^{-j\omega}\}}{1 + |c_k|^2 - 2\Re\{c_k e^{-j\omega}\}} \,. \tag{5.5}$$

By taking into account the secondary phase term resulting from these zeros the overall group delay was compensated to $\tau(\omega) = 0$ at the design tune, $\omega = \omega_d$. Note that a system having zero group delay is able to transmit the signal's envelop without delay. Figure 5.52(c) shows that the loop stability is ultimately improved by carefully compensating the group delay of the digital filter. With its flat phase response around the design tune this filter is robust against changes of the fractional tune in the order of $\pm 22\%$. This filter was tested in the SPS TFB by changing the machine's fractional tune and performing beam transfer function measurements. The results listed in Table 5.1 confirm the theory of negative feedback over the same range of fractional tunes.

Table 5.1: Measured loop response vs. tune.

Tune	0.14	0.16	**0.18**	0.20	0.22
Phase	$-167°$	$-179°$	$-182°$	$-182°$	$-187°$

New FIR phase shift filters have been designed and analysed for the SPS TFB based on a simple beam model in z-domain and with root locus plots, to assess their closed loop performance with beam and in presence of active feedback. The obtained results were found to be in good agreement with measurements carried out in the SPS. Limitations on system gain [110], the performance in the presence of noise [111, 112], and the ability to reject disturbances are subject of further studies.

The shortest digital filter described has only 3-taps, including DC suppression by a notch filter (for other realisations of short phase shift filters see for example [113–118]). Moreover, the tune sensitivity was further compensated with an additional pair

of conjugate complex zeros, effectively lowering the filter's group delay to zero at the fractional tune. Compensation of tune-dependent phase variations were reported also in Ref. [119].

The described digital filters are reasonable candidates for replacing the Hilbert phase shifter currently in use in the transverse feedback system of the SPS, mostly due to their favourable response over a larger range of tune values.

Chapter 6

Discussion and Conclusion

This chapter summarizes the main findings of the study on signal processing techniques for transverse feedback systems in hadron accelerators. It interprets their significance, discusses implications, acknowledges limitations, and offers concluding considerations on the overall impact of the study.

6.1 Introduction

The effective operation of transverse feedback (TFB) systems is critical for maintaining the stability and performance of particle accelerators. A recurring inquiry from the operations group has been: *Does the TFB work as intended?* This study aims to provide means to quickly answer this question by defining methodologies to extract important TFB and the accelerator parameters using exclusively the observables available in the TFB system.

By developing robust signal processing techniques and analysis algorithms, this research aims to create a comprehensive theoretical framework, supported by experimental data, that accurately evaluates the performance of TFBs. The goal is to develop practical methods that enable real-time measurement of TFB parameters during accelerator operations.

Traditional feedback parameters extraction techniques often rely on external instruments, which can be time-consuming and compromise beam stability or accuracy. In

contrast, this research explores the potential for feedback parameter extraction and performance optimization through active beam manipulation using only the TFB system. The study examines various factors that affect TFB performance, including loop gain, feedback phase, delay, and processing noise, and proposes methods for quantifying these parameters to enhance real-time verification of TFB performance.

Furthermore, the research investigates the extraction of key accelerator parameters, such as bunch-by-bunch machine tune and damping time, from observable quantities within the TFB system. This approach addresses operational concerns while contributing to a deeper understanding of the TFB's impact on the overall accelerator performance.

The following sections discuss the implications of these findings and highlight their importance for the operations group and the further development of TFB systems in particle accelerators.

6.2 Key findings

This study provided several important insights into signal processing techniques for transverse feedback systems in hadron accelerators. The advances made in this research are summarized below and divided into individual findings that improve the verification and optimization of TFB performance:

Finding #1: *The simplified z-domain beam model enables the application of digital signal processing methods in beam dynamics.*

This research demonstrates that the development of a simplified beam model in the z-domain represents a significant advance in the application of digital signal processing methods within this area. This model simplifies the analysis of beam dynamics and improves the applicability of sophisticated signal processing techniques, thereby facilitating real-time performance verification of TFB systems.

Finding #2: *The analytical sensor model enables the practical implementation of realistic LHC TFB behaviour in particle tracking code.*

This research demonstrates the significant importance of developing an analytical model that describes the relationship between the transverse beam position and the

generated output. It enables the realistic implementation of the transverse feedback behavior of the LHC and SPS in particle tracking codes. This is crucial for investigating beam stability and ensuring low emittance bunches in high-energy physics experiments.

Finding #3: *Analytical modeling of the sensor and actuator confirmed their ability to process bunches independently.*

This research demonstrates that a thorough analysis of the beam position sensor and actuator provides important insights into their performance. The hardware implementation has demonstrated its ability to treat bunches independently, thereby minimizing inter-symbol interference and ensuring accurate measurement and control of individual bunches.

Finding #4: *Novel methods for real-time reconstruction of transverse phase space coordinates for individual bunches.*

This research demonstrates advances in the understanding and application of phase adjustments in beam position signal processing. The proposed interpretations of spatial and temporal phase shifts create a robust framework for converting beam position signals into transverse phase space coordinates, thus enabling effective real-time performance monitoring.

Finding #5: *Definition of new signal processing methods for measuring key feedback parameters.*

This research demonstrates the development of a comprehensive method for extracting feedback parameters, thus fulfilling the need for practical measurement techniques in accelerator operation. By exploiting single-turn transverse excitations generated by the kicker of a transverse feedback system, real-time monitoring and adjustments become possible.

Finding #6: *Advanced signal processing techniques for extracting vital accelerator parameters.*

This research demonstrates that innovative methods for extracting vital accelerator parameters from observables within the transverse feedback system have been established. The ability to measure machine tune and damping time in real-time, bunch-by-

bunch, significantly improves operational capability and contributes to a deeper understanding of the TFB's impact on accelerator performance.

Finding #7: *Transverse phase space reconstruction methods require signal-to-noise ratio (SNR) of at least* $30\,\mathrm{dB}$ *to resolve tune variations of better than* 10^{-3}*.*

This research demonstrates that noise management is critical for accurate measurements and real-time performance verification, as the effectiveness of transverse phase space reconstruction methods decreases in noisy environments.

Finding #8: *The ADTObsBox system is equipped with advanced computational capabilities and efficient algorithms to support real-time data processing and high-performance analysis.*

This research demonstrates the need to implement efficient algorithms that can operate in real-time processing environments to improve the verification of TFB performance.

Finding #9: *The influence of short transverse excitations on beam size is negligible when a strong transverse feedback system is present.*

This research demonstrates that numerical simulations indicate minimal to no increase in transverse emittance at the current damping time of the LHC TFB. This enables routine measurements without compromising beam quality.

Overall, these results represent a significant contribution to the understanding and performance of transverse feedback systems in particle accelerators. They highlight both methodological advances and their practical implications for improving accelerator operations in real-world environments.

6.3 Interpretation of findings and significance of obtained results

The results of this study have important implications for the field of transverse feedback systems in particle accelerators. A key advance is the introduction of a simplified

beam model in the z-domain. This model improves the application of digital signal processing methods and facilitates access to advanced techniques for real-time performance verification of TFB systems. By more efficiently analyzing beam dynamics, it facilitates the use of sophisticated control engineering tools.

Another important insight comes from the development of an analytical model for LHC and SPS transverse feedback behavior. This model enables realistic implementations in particle tracking codes, which are crucial for studying beam stability and maintaining low emittance bunches. The ability of the sensor and actuator to treat bunches independently with minimal interference ensures accurate measurement and control, a vital achievement for high-energy accelerators.

Furthermore, the novel methods for real-time reconstruction of transverse phase space coordinates provide immediate insights into beam behavior. This enables operators to make informed decisions for performance optimization and mitigation of potential instabilities, thus significantly increasing the operational efficiency of particle accelerators.

A significant contribution of this study is the introduction of the concept of transverse activity, a novel metric that measures the instantaneous oscillation amplitude of the beam. This quantity not only facilitates the derivation of decay rates and TFB gain from transverse activity but also provides immediate diagnostics for transverse instabilities. Such instabilities can significantly impact the performance and safety of accelerator operations, making this diagnostic capability particularly valuable.

Based on this, we have introduced a method for calculating the TFB phase advance between the kicker and the pick-up following a single transverse kick. This method allows for immediate and non-destructive analysis of TFB phase settings, which is crucial for real-time monitoring and optimization of transverse feedbacks in accelerator environments.

Furthermore, we have presented a new technique for quantifying the kicker delay offset using TFB measurement data. By employing modulated kick data in quadrature, we constructed an IQ-footprint of the traversing bunches, allowing for the extraction of the delay offset. Our findings demonstrate accurate measurements of the TFB delay with sub-nanosecond precision. This level of accuracy is essential for fine-tuning TFB systems and ensuring optimal performance.

Furthermore, the ability to measure machine tune and damping time in real time on a bunch-by-bunch basis represents a significant advance in accelerator technology. This

granularity enables a more detailed understanding of accelerator performance and can lead to improved stability through adaptive control mechanisms.

Of particular note are insights into the signal-to-noise ratio requirements for capturing a transverse oscillation amplitude. The requirement of a minimum SNR of $30\,\mathrm{dB}$ to resolve tune variations underscores the importance of noise management in beam diagnostics. These findings are crucial for the development of future measurement systems and emphasizes the need for robust signal processing techniques that operate effectively even in challenging environments.

The conclusion that short transverse excitations in the presence of a strong TFB system have a negligible impact on beam size suggests that routine measurements can be performed without compromising beam quality. This finding supports the integration of regular evaluations into operational protocols and enables proactive monitoring of TFB performance.

Using these novel techniques, a full set of measurements to characterize the TFB system in CERN's LHC, comprising of 16 pick-ups and 8 signal processing units, takes less than a minute. The proposed techniques allow us not only to shorten the TFB commissioning time from several shifts to less than a minute but also regular, fully automated checks of TFB system can now be performed in case of suspected suboptimal performance, saving significant amounts of precious machine time.

In summary, these results underscore the potential for significant advances in the development and operation of transverse feedback systems. They pave the way for future research and improvements in this technology and contribute to improved performance and stability of particle accelerators.

6.4 Limitations of the study

Although this study presents significant advances in signal processing for transverse feedback systems in hadron accelerators, several limitations must be noted. A key limitation concerns the beam model simplifications. While advantageous for the application of digital signal processing methods, the simplified z-domain beam model may not fully capture the complexities of real beam dynamics. Certain nonlinear effects and interactions that occur in high-energy environments may not be fully captured, limiting the model's applicability in all operational scenarios.

Furthermore, the analytical sensor model is based on specific assumptions regarding the behavior of the LHC and SPS transverse feedback systems. Variations in operating conditions or hardware configurations may affect the model's accuracy and applicability in different scenarios. While the study identifies a minimum signal-to-noise ratio requirement for effective phase space reconstruction, it does not comprehensively analyze the influence of other noise sources or the resulting noise density function. Future studies should consider a wider range of noise factors to increase the robustness of the results.

The scope of experimental validation represents another important limitation. Although numerical simulations were performed to support the results, further experimental studies are needed to confirm the applicability of the proposed methods in different accelerator environments. This will allow a more comprehensive evaluation of their performance under different operating conditions. The results are primarily based on the LHC and SPS systems. While the techniques may be applicable to other accelerators, their effectiveness in different contexts or configurations still needs to be thoroughly investigated. Future research should investigate the generalizability of these methods to different accelerator types. The methods developed in this study may also face challenges when scaling up to larger or more complex accelerator systems with distributed TFB systems, necessitating further research to evaluate their scalability and adaptability for future projects.

In summary, while the study provides valuable insights into signal processing techniques for transverse feedback systems, these limitations underscore the need for continued research and validation to improve the applicability and robustness of the results.

6.5 Future research directions

Based on the results and limitations of this study, several research approaches can be identified to further development of signal processing techniques for transverse feedback systems in hadron accelerators:

An important focus is on improving modeling techniques. Future research should focus on developing more comprehensive beam models that account for nonlinear effects and complex interactions within the beam dynamics. The inclusion of advanced simulation techniques, such as machine learning algorithms or Kalman filters [120], could

improve the accuracy of predictions and enhance the understanding of beam-feedback interactions under different conditions.

In this study, we investigated and developed methods and signal processing techniques for extracting important accelerator parameters from observables within the transverse feedback system. Relevant parameters were the bunch-by-bunch machine tune and damping time, both of which are critical for optimizing accelerator performance and stability.

We successfully developed and implemented a novel method for measuring the fractional tune on a bunch-by-bunch basis within the LHC's transverse feedback system. This represents a significant advance, as previous implementations were limited to measuring the machine tune without considering the granularity of individual bunches.

The current LHC tune detection system (BBQ) primarily relies on witness bunches to perform machine tune measurements. Our method improves on individual bunch measurements by enabling real-time monitoring of the fractional tune of all bunches, thus enabling a more detailed understanding of the accelerator's performance in real-time.

The ability to measure machine tune and damping time of individual bunches in real time has important implications for optimizing of accelerator operations. By applying signal processing techniques, we identified patterns in the transverse feedback phase that correlate with changes in the machine's fractional tune. We proposed integration of an adjustable bunch-by-bunch tune into the signal processing hardware, representing a promising upgrade scenario for the current TFB system. By modulating the feedback phase based on the bucket position, the system can adapt to real-time conditions, potentially leading to improved stability and performance.

Particularly significant is the proposal to use a parameterized model to calculate expected tune shifts based on bunch intensity. This approach not only automates the process but also ensures that the feedback system responds to fluctuations in beam conditions, which is crucial for maintaining optimal accelerator performance. The proposed integration of feedback phase modulation based on bunch intensity and filling patterns has the potential to revolutionize accelerator operations. By actively counteracting tune dependency, accelerator physicists could achieve a more stable and consistent operating environment.

The results of this study open up diverse possibilities for future research. Investigating the potential for real-time adjustments of the feedback phase, refining the specifics of

the parameterized model, testing its effectiveness in real-world scenarios, and analyzing the broader implications of these findings for accelerator physics are crucial next steps toward significant advances in accelerator technology.

Another important area for future research is experimental validation. Comprehensive experimental validation of the proposed methods is essential to ensure their applicability. Future studies should aim to implement the developed techniques in real-world accelerator environments such as the LHC or other facilities to evaluate their performance and reliability in practice. These practical tests will provide valuable feedback and strengthen the credibility of the results. Investigating the applicability of the developed methods in different accelerator environments, such as the PS or PSB, will broaden the impact of this research. Comparative studies could provide insights into the versatility and adaptability of the techniques across various systems. The development of adaptive control mechanisms could utilize real-time data from the proposed signal processing methods to implement feedback loops that adjust system parameters based on instantaneous measurements, thus improving the stability and performance of particle accelerators.

The establishment of long-term monitoring systems leveraging the results of this study could improve operational protocols in particle accelerators. Research could focus on developing diagnostic tools that enable continuous assessment of beam stability and TFB performance, thus enabling proactive maintenance and optimization. Finally, fostering interdisciplinary collaboration between physicists, engineers, and data scientists will be vital for advancing the field. Joint efforts can lead to innovative solutions and the development of cutting-edge technologies that enhance the performance and capabilites of transverse feedback systems.

In summary, these future research directions highlight the opportunities for further advances in signal processing techniques for transverse feedback systems. By addressing the identified areas, researchers can contribute to the continuous improvement of particle accelerator technology and its applications in high-energy physics.

6.6 Conclusions

This study made significant contributions to the field of transverse feedback systems in particle accelerators, particularly in the context of hadron accelerators. By developing innovative signal processing techniques and analytical models, we have improved the

understanding and application of transverse feedback systems. This research addresses critical questions about their performance and functionality, paving the way for improved accelerator operation.

One of the most important findings of this study is the introduction of a simplified beam model in the z-domain, which facilitates the application of digital signal processing methods in beam dynamics. This advance not only simplifies the analysis of beam behavior but also improves the integration of sophisticated techniques into real-time systems, thus increasing operational efficiency.

Furthermore, the development of an analytical sensor model enabled the realistic implementation of transverse feedback behavior in particle tracking codes, which is essential for investigating beam stability in high-energy physics experiments. The ability to treat bunches independently, as confirmed by our analytical modeling of sensors and actuators, underscores the robustness of the TFB system and its optimization potential.

The novel methods for real-time reconstruction of transverse phase-space coordinates represent a significant advance in operational capabilities. By enabling immediate diagnostics and adjustments, these methods enable operators to increase performance and effectively minimize instabilities.

Furthermore, the comprehensive approach to measuring key feedback parameters and vital accelerator parameters opens new avenues for research and operational improvements. The results suggest that real-time monitoring and adaptive control mechanisms can be implemented to optimize accelerator performance, thus ensuring stability and efficient operation. The focus of the work is on finding a simple, well-defined parameter or method that provides clear answers to operational questions, such as: *Is the damper damping?* The research presented here contributes to this goal by developing methods that provide the positive answer, *Yes, the TFB is functioning properly and the damper is damping.* These practical insight are crucial for the operations group, enabling informed decision-making and ensuring optimal performance in complex accelerator environments.

In summary, this research not only addresses the operational aspects of TFB systems but also contributes to a deeper understanding of their impact on accelerator performance. The presented methods and insights lay the foundation for future advances in TFB technology and its applications in particle accelerators. Future research should focus on the broader applicability of the developed models and techniques in different accelerator environments. Investigating the integration of these methods into existing feedback systems, as well as exploring their potential for real-time adjustments, will be crucial for

the further development of this research area. By further refining and expanding these insights, we can further improve the performance and reliability of particle accelerators and ultimately contribute to the advancement of high-energy physics research.

Author's publications journals

[1] G. Kotzian, X. Buffat, J. Komppula, V. Stopjakova, and D. Valuch, "Modern signal processing techniques for efficient transverse feedback systems operation in hadron accelerators," *Phys. Rev. Accel. Beams*, pp. –, Sep 2025.

[2] G. Kotzian, M. Söderén, P. Solvang, D. Valuch, and V. Stopjakova, "Reconstruction of transverse phase space from transverse feedback data for real time extraction of vital lhc machine parameters," *Journal of Physics: Conference Series*, vol. 2420, p. 012077, 01 2023.

[3] G. Kotzian, "Possibilities for transverse feedback phase adjustment by means of digital filters," *Journal of Physics: Conference Series*, vol. 874, p. 012089, 07 2017.

Author's publications proceedings

[1] M. Carlà, H. Bartosik, M. Beck, L. Carver, V. Kain, G. Kotzian, K. Li, G. Rumolo, and C. Zannini, "Transverse Beam Dynamics Studies With High Intensity LHC Beams in the SPS," in *Proc. IPAC'19*, pp. 1062–1065, JACoW Publishing, Geneva, Switzerland, 2019.

[2] G. P. D. Giovanni, F. Antoniou, F. Blas, Y. Brischetto, A. Findlay, G. Kotzian, B. Mikulec, and G. Sterbini, "Commissioning of a New Digital Transverse Damper System at the PSB," in *Proc. IPAC'19*, pp. 1050–1053, JACoW Publishing, Geneva, Switzerland, 2019.

[3] A. Blas and G. Kotzian, "Upgraded Transverse Feedback for the CERN PS Booster," in *Proc. HB'18*, pp. 256–259, JACoW Publishing, Geneva, Switzerland, 2018.

[4] K. Li, H. Bartosik, M. Beck, E. R. Bjørsvik, J. E. Dusatko, J. D. Fox, W. Höfle, G. Kotzian, T. Levens, C. H. Rivetta, M. Schenk, and O. Turgut, "Recent Results from the Wideband Feedback System Tests at the SPS and Future Plans," in *Proc. HB'18*, pp. 38–42, JACoW Publishing, Geneva, Switzerland, 2018.

[5] J. D. Fox, J. Dusatko, H. Bartosik, E. Bjorsvik, W. Höfle, G. Kotzian, K. Li, E. Metral, C. Rivetta, B. Salvant, O. Turgut, and U. Wehrle, "Control of Intra-Bunch Vertical Motion in the SPS with GHz Bandwidth Feedback," in *Proc. IPAC'18*, pp. 2365–2368, JACoW Publishing, Geneva, Switzerland, 2018.

[6] W. Höfle, J. Komppula, G. Kotzian, K. S. B. Li, and D. Valuch, "Transverse Feedback System for the CERN FCC-hh Collider," in *Proc. IPAC'18*, pp. 1997–2000, JACoW Publishing, Geneva, Switzerland, 2018.

[7] W. Höfle, H. Bartosik, E. Bjørsvik, J. Dusatko, J. Fox, G. Kotzian, T. Levens, K. Li, C. Rivetta, and O. Turgut, "Impact of a Wideband Feedback Prototype System on

TMCI in the SPS," in *Proc. IPAC'18*, pp. 1208–1211, JACoW Publishing, Geneva, Switzerland, 2018.

[8] B. Salvant, S. Antipov, G. Arduini, N. Biancacci, X. Buffat, L. Carver, P. Collier, A. Gorzawski, W. Höfle, G. Iadarola, G. Kotzian, A. Lechner, T. Levens, E. Métral, D. Mirarchi, G. Rumolo, D. Valuch, and L. Mether, "Experimental Characterisation of a Fast Instability Linked to Losses in the 16L2 Cryogenic Half-Cell in the CERN LHC," in *Proc. IPAC'18*, pp. 3103–3106, JACoW Publishing, Geneva, Switzerland, 2018.

[9] J. M. Jimenez, D. Amorim, S. Antipov, G. Arduini, A. Bertarelli, N. Biancacci, B. Bradu, E. Bravin, G. Bregliozzi, K. Brodzinski, R. Bruce, X. Buffat, L. Carver, P. Chiggiato, S. Claudet, P. Collier, R. Alia, M. Giovannozzi, A. Gorzawski, L. Grob, W. Höfle, E. Holzer, G. Iadarola, G. Kotzian, A. Lechner, T. Levens, B. Lindstrom, T. Medvedeva, L. Mether, E. Métral, A. Milanese, D. Mirarchi, D. Perini, S. Redaelli, G. Rumolo, B. Salvant, R. Schmidt, M. Valette, D. Valuch, J. Wenninger, D. Wollmann, C. Vallgren, C. Zamantzas, and M. Zerlauth, "Observations, Analysis and Mitigation of Recurrent LHC Beam Dumps Caused by Fast Losses in Arc Half-Cell 16L2," in *Proc. IPAC'18*, pp. 228–231, JACoW Publishing, Geneva, Switzerland, 2018.

[10] G. Kotzian, "Transverse Feedback Parameter Extraction from Excitation Data," in *Proc. IPAC'17*, pp. 1920–1923, JACoW Publishing, Geneva, Switzerland, 2017.

[11] G. Kotzian, W. Höfle, and D. Valuch, "Sensitivity of the LHC Transverse Feedback System to Intra-Bunch Motion," in *Proc. IPAC'17*, pp. 1916–1919, JACoW Publishing, Geneva, Switzerland, 2017.

[12] M. Söderén, G. Kotzian, M. O. Sandonis, and D. Valuch, "Online Bunch by Bunch Transverse Instability Detection in LHC," in *Proc. IPAC'17*, pp. 397–399, JACoW Publishing, Geneva, Switzerland, 2017.

[13] L. R. Carver, X. Buffat, A. Butterworth, W. Höfle, G. Iadarola, G. Kotzian, K. Li, E. Métral, M. Ojeda-Sandonis, M. Söderén, and D. Valuch, "Usage of the Transverse Damper Observation Box for High Sampling Rate Transverse Position Data in the LHC," in *Proc. IPAC'17*, pp. 389–392, JACoW Publishing, Geneva, Switzerland, 2017.

[14] W. Bartmann, M. Barnes, J. Boyd, E. Carlier, A. Chmielinska, K. B. Goddard, C. Schwick, L. Stoel, D. Valuch, F. Velotti, V. Vlachodimitropoulos, and C. Wiesner, "Impact of LHC and SPS Injection Kicker Rise Times on Lhc Filling Schemes and Luminosity Reach," in *Proc. IPAC'17*, pp. 2043–2046, JACoW Publishing, Geneva, Switzerland, 2017.

[15] J. F. Wagner, R. Bruce, H. Garcia-Morales, W. Höfle, G. Kotzian, R. Kwee-Hinzmann, A. Langner, A. Mereghetti, E. Quaranta, S. Redaelli, A. Rossi, B. Salvachua, G. Stancari, R. Tomás, G. Valentino, and D. Valuch, "First Attempts at using Active Halo Control at the LHC," in *Proc. IPAC'16*, pp. 2486–2489, JACoW Publishing, Geneva, Switzerland, 2016.

[16] L. R. Carver, J. Barranco, N. Biancacci, X. Buffat, W. Höfle, G. Kotzian, T. Lefevre, T. Levens, E. Métral, T. Pieloni, B. Salvant, C. Tambasco, N. Wang, and M. Zobov, "Current Status of Instability Threshold Measurements in the LHC at 6.5 TeV," in *Proc. IPAC'16*, pp. 1434–1437, JACoW Publishing, Geneva, Switzerland, 2016.

[17] B. Goddard, E. Carlier, L. Ducimetière, G. Kotzian, J. A. Uythoven, and F. M. Velotti, "SPS Injection and Beam Quality for LHC Heavy Ions With 150 ns Kicker Rise Time," in *Proc. IPAC'16*, pp. 1360–1362, JACoW Publishing, Geneva, Switzerland, 2016.

[18] W. Höfle, G. Kotzian, and D. Valuch, "Transverse Rigid Dipole and Intra-Bunch Oscillation Detection Using the Transverse Feedback Beam Position Detection Scheme in SPS and LHC," in *Proc. IBIC'15*, pp. 456–460, JACoW Publishing, Geneva, Switzerland, 2015.

[19] G. Iadarola, H. Bartosik, T. Bohl, B. Goddard, G. Kotzian, K. Li, L. Mether, G. Rumolo, E. Shaposhnikova, M. Schenk, and M. Taborelli, "Detailed Studies of Beam Induced Scrubbing in the CERN-SPS," in *Proc. IPAC'15*, pp. 3908–3910, JACoW Publishing, Geneva, Switzerland, 2015.

[20] C. H. Rivetta, J. Cesaratto, J. Dusatko, J. D. Fox, W. Höfle, K. Li, G. Kotzian, and O. Turgut, "Feedback System Design Techniques for Control of Intra-bunch Instabilities at the SPS," in *Proc. IPAC'14*, pp. 1769–1771, JACoW Publishing, Geneva, Switzerland, 2014.

AUTHOR'S PUBLICATIONS PROCEEDINGS

[21] J. D. Fox, J. M. Cesaratto, S. D. Santis, J. Dusatko, W. Höfle, G. Kotzian, K. Pollock, C. Rivetta, O. Turgut, and U. Wehrle, "Development of a 4 GS/s Intra-bunch Instability Control System for the SPS - Next Steps," in *Proc. IPAC'14*, pp. 1766–1768, JACoW Publishing, Geneva, Switzerland, 2014.

[22] G. Kotzian, W. Höfle, R. J. Steinhagen, D. Valuch, and U. Wehrle, "Evaluation of Strip-line Pick-up System for the SPS Wideband Transverse Feedback System," in *Proc. IBIC'13*, pp. 690–693, JACoW Publishing, Geneva, Switzerland, 2013.

[23] F. Dubouchet, W. Höfle, G. Kotzian, T. E. Levens, D. Valuch, and P. Albuquerque, "Tune Measurement from Transverse Feedback Signals in LHC," in *Proc. IBIC'13*, pp. 579–582, JACoW Publishing, Geneva, Switzerland, 2013.

[24] C. H. Rivetta, H. Bartosik, J. M. Cesaratto, J. Dusatko, J. D. Fox, W. Höfle, G. Kotzian, K. Li, M. Pivi, K. Pollock, and O. Turgut, "Control of Intrabunch Dynamics at CERN SPS Ring using 3.2 GS/s Digital Feedback Channel," in *Proc. NAPAC'13*, pp. 1430–1433, JACoW Publishing, Geneva, Switzerland, 2013.

[25] J. M. Cesaratto, H. Bartosik, J. M. Cesaratto, J. Dusatko, W. Höfle, G. Kotzian, J. Olsen, K. Pollock, C. Rivetta, O. Turgut, and U. Wehrle, "First Results and Analysis of the Performance of a 4 GS/s Intra-bunch Vertical Feedback System at the SPS," in *Proc. IPAC'13*, pp. 3070–3072, JACoW Publishing, Geneva, Switzerland, 2013.

[26] W. Höfle, F. Dubouchet, G. Kotzian, and D. Valuch, "Performance of the LHC Transverse Damper with Bunch Trains," in *Proc. IPAC'13*, pp. 3022–3024, JACoW Publishing, Geneva, Switzerland, 2013.

[27] W. Höfle, G. Arduini, R. D. Maria, G. Kotzian, D. Valuch, and V. A. Lebedev, "Suppression of Emittance Growth by Excited Magnet Noise with the Transverse Damper in LHC in Simulations and Experiment," in *Proc. IPAC'11*, pp. 508–510, JACoW Publishing, Geneva, Switzerland, 2011.

[28] W. Höfle, G. Kotzian, M. Schokker, and D. Valuch, "LHC Damper Beam Commissioning in 2010," in *Proc. IPAC'11*, pp. 505–507, JACoW Publishing, Geneva, Switzerland, 2011.

[29] V. Zhabitsky, W. Höfle, G. Kotzian, E. Montesinos, M. Schokker, and D. Valuch, "Beam Tests of the LHC Transverse Feedback System," in *Proc. RuPAC'10*, pp. 275–279, JACoW Publishing, Geneva, Switzerland, 2010.

[30] R. D. Maria, C. Boccard, W. Höfle, G. Kotzian, C. P. Montava, and B. Salvant, "Analysis of the Performance of the SPS Exponential Coupler Striplines using Beam Measurements and Simulation Data," in *Proc. IPAC'10*, pp. 2812–2814, JACoW Publishing, Geneva, Switzerland, 2010.

[31] G. Kotzian, F. Caspers, R. D. Maria, S. Federmann, and W. Höfle, "Ringing in the Pulse Response of Long and Wideband Coaxial Transmission Lines due to Group Delay Dispersion," in *Proc. PAC'09*, pp. 3519–3521, JACoW Publishing, Geneva, Switzerland, 2009.

[32] R. de Maria, J. Fox, W. Höfle, G. Kotzian, G. Rumolo, B. Salvant, and U. Wehrle, "Performance of Exponential Coupler in the SPS with LHC Type Beam for Transverse Broadband Instability Analysis," in *Proc. DIPAC'09*, pp. 83–85, JACoW Publishing, Geneva, Switzerland, 2009.

[33] V. M. Zhabitsky, W. Höfle, and G. Kotzian, "Beam stability in synchrotrons with notch and all-pass filters in the feedback loop of a transverse damper," Tech. Rep. CERN-BE-2009-013, CERN, Geneva, Apr. 2009.

[34] T. Linnecar, M. Angoletta, L. Arnaudon, P. Baudrenghien, T. Bohl, O. Brunner, A. Butterworth, E. Ciapala, F. Dubouchet, J. Ferreira-Bento, D. Glenat, G. Hagmann, W. Höfle, C. Julie, F. Killing, G. Kotzian, D. Landre, R. Louwerse, P. Maesen, P. Martinez-Yanez, J. Molendijk, E. Montesinos, C. Nicou, J. Noirjean, G. Papotti, A. Pashnin, G. Pechaud, J. Pradier, V. Rossi, J. Sanchez-Quesada, M. Schokker, E. Shaposhnikova, R. Sorokoletev, D. Stellfeld, J. Tuckmantel, D. Valuch, U. Wehrle, and F. Weierud, "Hardware and Initial Beam Commissioning of the LHC RF Systems," Tech. Rep. LHC-PROJECT-Report-1172, CERN, Geneva, Oct. 2008.

[35] W. Höfle, P. Baudrenghien, G. Kotzian, and V. Rossi, "Digital Signal Processing for the Multi-bunch LHC Transverse Feedback System," in *Proc. EPAC'08*, pp. 3269–3271, JACoW Publishing, Geneva, Switzerland, 2008.

[36] W. Höfle, P. Baudrenghien, E. V. Gorbachev, F. Killing, I. Kojevnikov, G. Kotzian, N. I. Lebedev, R. Louwerse, A. A. Makarov, E. Montesinos, S. V. Rabtsun, V. Rossi, M. Schokker, E. Thepenier, D. Valuch, and V. Zhabitsky, "LHC Transverse Feedback System and its Hardware Commissioning," in *Proc. EPAC'08*, pp. 3266–3268, JACoW Publishing, Geneva, Switzerland, 2008.

[37] G. Kotzian, W. Höfle, and E. Vogel, "LHC Transverse Feedback Damping Efficiency," in *Proc. EPAC'08*, pp. 3632–3634, JACoW Publishing, Geneva, Switzerland, 2008.

[38] B. Goddard, M. J. Barnes, L. Ducimetière, W. Höfle, and G. Kotzian, "Emittance Growth at LHC Injection from SPS and LHC Kicker Ripple," in *Proc. EPAC'08*, pp. 3629–3631, JACoW Publishing, Geneva, Switzerland, 2008.

[39] V. Zhabitsky, P. Baudrenghien, E. V. Gorbachev, W. Höfle, F. Killing, I. Kojevnikov, G. Kotzian, N. Lebedev, R. Louwerse, A. Makarov, E. Montesinos, N. Pilyar, S. Rabtsun, V. Rossi, M. Schokker, R. Smolkov, E. Thepenier, and D. Valuch, "LHC Transverse Feedback system: First results of commissioning," in *Proc. RuPAC'08*, pp. 97–100, JACoW Publishing, Geneva, Switzerland, 2008.

[40] A. Koschik, B. Goddard, W. Höfle, G. Kotzian, D. K. Kramer, and T. Kramer, "Abort Gap Cleaning Using the Transverse Feedback System: Simulation and Measurements in the SPS for the LHC Beam Dump System," in *Proc. EPAC'08*, pp. 2656–2658, JACoW Publishing, Geneva, Switzerland, 2008.

Appendix A

Damping Time and Feedback Gain

In control systems, the behavior of a second-order system can be characterized by its transfer function. For a standard second-order system, the transfer function is given by:

$$G(s) = \frac{\omega_n^2}{s^2 + 2\zeta\omega_n s + \omega_n^2} \tag{A.1}$$

where ω_n represents the natural frequency of the system, and ζ denotes the damping ratio, which indicates how oscillations in a system decay after a disturbance.

To enhance the damping characteristics of the system, we introduce a damping feedback with gain K. This feedback modifies the system's dynamics, resulting in a new transfer function expressed as:

$$G'(s) = \frac{\omega_n^2}{s^2 + (2\zeta + K)\omega_n s + \omega_n^2} \tag{A.2}$$

In this modified transfer function, the term K effectively increases the damping ratio, thereby influencing the system's response to inputs. The new damping ratio, denoted as ζ', can be formulated as:

$$\zeta' = \zeta + \frac{K}{2\omega_n} \tag{A.3}$$

For our analysis, we assume that the internal damping of the system is weak, which implies that the original damping ratio ζ is very small (i.e., $\zeta \approx 0$). Under this assumption, we can simplify the expression for the new damping ratio to:

$$\zeta' \approx \frac{K}{2\omega_n} \tag{A.4}$$

A. DAMPING TIME AND FEEDBACK GAIN

The damping time, denoted as τ_d, is a critical parameter that describes how quickly the system responds to disturbances [103]. It is related to the damping ratio by the following relationship:

$$\tau_d = \frac{1}{\zeta' \omega_n} \tag{A.5}$$

Substituting for ζ' gives the relationship between damping time and feedback gain:

$$\tau_d = \frac{2}{K} \tag{A.6}$$

References

[1] G. P. D. Giovanni, F. Antoniou, F. Blas, Y. Brischetto, A. Findlay, G. Kotzian, B. Mikulec, and G. Sterbini, "Commissioning of a New Digital Transverse Damper System at the PSB," in *Proc. IPAC'19*, pp. 1050–1053, JACoW Publishing, Geneva, Switzerland, 2019.

[2] D. Valuch and P. Baudrenghien, "Beam phase measurement and transverse position measurement module for the lhc," Tech. Rep. EDMS-929563, CERN, Geneva, 2007.

[3] M. G. Minty, A. W. Chao, and W. L. Spence, "Emittance growth due to decoherence and wakefields," in *Proc. 16th Particle Accelerator Conf. 1995*, (Dallas, Texas), pp. 3037–3039, May 1-5 1995.

[4] O. Brünning, P. Collier, P. Lebrun, S. Myers, R. Ostojic, J. Poole, and P. Proudlock, eds., *LHC Design Report, Vol. 1*, ch. 5.3, p. 103. CERN Scientific Information Service, June 2004.

[5] L. Thorndahl and A. Vaughan, "Transverse feedback for the ISR," *IEEE Transactions on Nuclear Science*, vol. 20, no. 3, pp. 807–808, 1973.

[6] R. E. C., "Bunch-to-bunch transverse feedback for the ags," Tech. Rep. 209, Brookhaven National Laboratory, 10 1984.

[7] C. Carter, C. Christiansen, J. Donnat, G. Gelato, M. Le Gras, H. O. Schönauer, and D. J. Williams, "The transverse feedback system for the CERN PS booster," *IEEE Trans. Nucl. Sci.*, vol. 28, pp. 2270–2272, 1981.

[8] J. Xu, J. Claus, E. Raka, A. G. Ruggiero, and T. J. Shea, "The transverse damper system for rhic," Tech. Rep. BNL-45356; CONF-910505-237, Brookhaven National Laboratory, 1 1991.

[9] P. Baudrenghien, E. V. Gorbachev, W. Höfle, F. Killing, I. Kojevnikov, G. Kotzian, N. I. Lebedev, R. Louwerse, A. A. Makarov, E. Montesinos, S. V. Rabtsun, V. Rossi, M. Schokker, E. Thepenier, D. Valuch, and V. Zhabitsky, "LHC Transverse Feedback System and its Hardware Commissioning," tech. rep., CERN, 2008.

[10] K. Wille, "Calculation of a nonlinear transverse feedback system," Tech. Rep. DESY PET-79/01, DESY, 1979.

[11] J. Rogers, M. Billing, J. Dobbins, C. Dunnam, D. Hartill, T. Holmquist, B. McDaniel, T. Pelaia, M. Pisharody, J. Sikora, and C. Strohman, "Operation of a fast digital transverse feedback system in cesr," in *Proceedings Particle Accelerator Conference*, vol. 4, pp. 2426–2428 vol.4, 1995.

[12] J.-L. Pellegrin, "Transverse Oscillations Damping with Wide-Band Feedback on SPEAR II," in *Proc. PAC'75*, pp. 1500–1505, JACoW Publishing, Geneva, Switzerland, 1975.

[13] J. Wang, K. Zheng, W. Li, L. Wang, Z. Liu, Y. Yang, Z. Zhou, B. Sun, Y. Cheng, L. Huang, J. Cao, D. Liu, and k. ye, "Development of transverse feedback system and instabilities suppress at hls," in *2007 IEEE Particle Accelerator Conference (PAC)*, pp. 269 – 271, 07 2007.

[14] J. Liu, J. C. Yang, J. W. Xia, D. Y. Yin, G. D. Shen, P. Li, B. Wu, S. Ruan, H. Zhao, G. Wang, Z. Q. Dong, K. D. Wang, and L. P. Yao, "Transverse impedances and collective instabilities in a heavy ion accelerator," *Phys. Rev. Accel. Beams*, vol. 21, p. 064403, Jun 2018.

[15] N. Mounet, *The LHC Transverse Coupled-Bunch Instability*. Phd thesis, École Ppolytechnique Fédérale de Lausanne, Lausanne, Switzerland, March 2012. Available at https://cds.cern.ch/record/1451296?ln=en.

[16] W. Höfle, G. Arduini, R. D. Maria, G. Kotzian, D. Valuch, and V. A. Lebedev, "Suppression of Emittance Growth by Excited Magnet Noise with the Transverse Damper in LHC in Simulations and Experiment," in *Proc. IPAC'11*, pp. 508–510, JACoW Publishing, Geneva, Switzerland, 2011.

[17] V. Lebedev, V. V. Parkhomchuk, V. D. Shiltsev, and G. Stupakov, "Emittance growth due to noise and its suppression with the feedback system in large hadron colliders," *Part. Accel.*, vol. 44, pp. 147–164, 1994.

[18] E. Keil, W. Schnell, and P. Strolin, "Feedback damping of horizontal beam transfer errors," Tech. Rep. CERN 69-27, CERN, 1969.

[19] G. P. Jackson, "The effect of chromatic decoherence on transverse injection oscillation damping," in *Proc. Technical Workshop on Feedback Control of Multi-Bunch Instabilities in Proton Colliders at the Highest Energies and Luminosities*, 1993.

[20] J. M. Vogt, J. C. Bergstrom, S. Hu, and V. Poucki, "Bunch Cleaning at the Canadian Light Source," in *Proc. PAC'09*, pp. 4111–4113, 2009.

[21] A. Gamelin, "SOLEIL transverse bunch-by-bunch feedback system," in *Proceedings of I.FAST Workshop 2024 on Bunch-by-Bunch Feedback Systems and Related Beam Dynamics*, 2024.

[22] E. Gianfelice-Wendt *et al.*, "LHC Abort Gap Cleaning Studies During Luminosity Operation," in *3rd International Particle Accelerator Conference*, 5 2012.

[23] M. Soderen, *Online Transverse Beam Instability Detection in the LHC. High Throughput Real-Time Parallel Data Analysis*. Master thesis, Linköping University, Linköping, Sweden, November 2017. Presented 13 Nov 2017.

[24] X. Buffat, S. Furuseth, and G. Vicentini, "Chromaticity measurement using beam transfer function in high energy synchrotrons," in *Proceedings of the ICFA ABDW on High-Intensity and High-Brightness Hadron Beams*, pp. 46–51, JACoW Publishing, Geneva, Switzerland, 2021.

[25] S. A. Antipov, D. Amorim, N. Biancacci, X. Buffat, E. Métral, N. Mounet, A. Oeftiger, and D. Valuch, "Proof-of-principle direct measurement of landau damping strength at the large hadron collider with an antidamper," *Phys. Rev. Lett.*, vol. 126, p. 164801, Apr 2021.

[26] S. A. Antipov, C. Accettura, D. Amorim, A. Bertarelli, N. Biancacci, R. Bruce, E. Carideo, F. Carra, J. Guardia Valenzuela, A. Mereghetti, E. Métral, S. Redaelli, B. Salvant, and D. Valuch, "Transverse beam stability with low-impedance collimators in the high-luminosity large hadron collider: Status and challenges," *Phys. Rev. Accel. Beams*, vol. 23, p. 034403, Mar 2020.

[27] D. J. Peake, M. J. Boland, G. LeBlanc, and R. P. Rassool, "Growth/Damp Measurements and Bunch-by-Bunch Diagnostics on the Australian Synchrotron Storage

Ring," in *Proc. PAC'09*, no. 23 in Particle Accelerator Conference, pp. 4105–4107, JACoW Publishing, Geneva, Switzerland, 2009.

[28] Söderén, Martin and Valuch, Daniel, "Low latency, online processing of the high-bandwidth bunch-by-bunch observation data from the transverse feedback system in the LHC," *EPJ Web Conf.*, vol. 245, p. 01036, 2020.

[29] P. Forck, "Beam Instrumentation and Diagnostics," in *CAS - CERN Accelerator School 2019: Introduction to Accelerator Physics*, 9 2020.

[30] R. E. Shafer, "Beam position monitoring," *AIP Conference Proceedings*, vol. 249, pp. 601–636, 03 1992.

[31] G. Carron, S. Myers, and L. Thorndahl, "The 50 mhz transverse feedback system in the cern isr," *IEEE Transactions on Nuclear Science*, vol. 24, no. 3, pp. 1833–1835, 1977.

[32] R. Bossart, L. Burnod, J. Gareyte, B. de Raad, and V. Rossi, "The damper for the transverse instabilities of the sps," *IEEE Transactions on Nuclear Science*, vol. 26, no. 3, pp. 3284–3286, 1979.

[33] C. Ankenbrandt, E. F. Higgins, and R. P. Johnson, "Suppression of transverse instabilities by fast feedback in the fermilab booster," *IEEE Transactions on Nuclear Science*, vol. 24, no. 3, pp. 1698–1700, 1977.

[34] L. Vos, "Transverse feedback system in the CERN SPS," Tech. Rep. CERN-SL-91-40-BI, CERN, 1992.

[35] R. Takai, T. Honda, T. Nogami, T. Obina, Y. Tanimoto, and M. Tobiyama, "A New Stripline Kicker for PF-AR Transverse Feedback Damper," in *Proc. IBIC'16*, pp. 344–347, JACoW Publishing, Geneva, Switzerland, 2016.

[36] E. V. Gorbachev *et al.*, "LHC transverse feedback system: First results of commissioning," in *21st Russian Particle Accelerators Conference* , pp. 97–100, 9 2008.

[37] R. Bossart, J. P. Moens, and J. Mourier, "The digital delay line of the damper," Tech. Rep. CERN-SPS-ABM-83-088-0070G, CERN, Geneva, 1983.

[38] G. Lambert, "Un convertisseur analogique numerique 8 bit ultra rapide: (Frequence d'echantillonage 100 MHz)," Tech. Rep. CERN-SPS-ARF-Note-GL-gw-84-15, CERN, Geneva, 1984.

[39] R. Bossart, R. Louwerse, and J. Mourier, "The digital notch filter of the damper," Tech. Rep. CERN-SPS-ABM-Note-85-10, CERN, Geneva, 1985.

[40] V. Zhabitsky, I. Korenev, and L. Yudin, "Transverse feedback system with digital filter," in *Proceedings of International Conference on Particle Accelerators*, pp. 2543–2545 vol.3, 1993.

[41] K. Nakamura *et al.*, "Transverse Intra-bunch Feedback in the J-PARC MR," in *Proc. IPAC'14*, pp. 2786–2788, JACoW Publishing, Geneva, Switzerland, 2014.

[42] J. D. Fox, "Progress on intra-bunch GHz bandwidth beam feedback and applications for future accelerators," *Beam Dynamics Newsletter*, no. 77, pp. 19–34, 2019.

[43] S. V. Furuseth, X. Buffat, J. S. Pereira-Cubillo, and D. Valuch, "Emittance growth suppression with a multibunch feedback in high-energy hadron colliders: Numerical optimization of the gain and bandwidth," *Phys. Rev. Accel. Beams*, vol. 24, p. 011003, Jan 2021.

[44] X. Buffat, W. Herr, T. Pieloni, and D. Valuch, "Modeling of the emittance growth due to decoherence in collision at the large hadron collider," *Phys. Rev. Accel. Beams*, vol. 23, p. 021002, Feb 2020.

[45] C. M. Ankenbrandt, E. F. Higgins, and R. P. Johnson, "Suppression of Transverse Instabilities by Fast Feedback in the Fermilab Booster," in *Proc. PAC'77*, pp. 1698–1701, JACoW Publishing, Geneva, Switzerland, 1997.

[46] W. Ebeling, "The Transverse Feedback System in DESY," in *Proc. PAC'81*, pp. 2285–2287, JACoW Publishing, Geneva, Switzerland, 1981.

[47] J. L. Pellegrin and J. R. Rees, "Beam excitation and damping with the transverse feedback system," *Office of Scientific & Technical Information Technical Reports*, 8 1979.

[48] C. Carter, C. Christiansen, J. Donnat, G. Gelato, M. Le Gras, H. Schonauer, and D. J. Williams, "The transverse feedback system for the cern ps booster," *IEEE Transactions on Nuclear Science*, vol. 28, no. 3, pp. 2270–2272, 1981.

[49] A. Blas and G. Kotzian, "Upgraded Transverse Feedback for the CERN PS Booster," in *Proc. HB'18*, pp. 256–259, JACoW Publishing, Geneva, Switzerland, 2018.

[50] R. H. Hilden, J. H. Martin, F. E. Mills, and R. A. Winje, "Apparatus for damping axial coherent beam instabilities in a synchrotron particle accelerator.," *patent*, 4 1968.

[51] B. Sandberg, "Logic and Control Module for the Fermilab Booster Beam Damper," in *Proc. PAC'77*, pp. 1770–1772, JACoW Publishing, Geneva, Switzerland, 1977.

[52] E. F. Higgins, "Electronics for Damping Transverse Instabilities for the Fermilab Booster Synchrotron," in *Proc. PAC'77*, pp. 1830–1833, JACoW Publishing, Geneva, Switzerland, 1977.

[53] R. Bossart, R. Louwerse, and J. Mourier, "The digital notch filter of the damper," tech. rep., CERN, Geneva, 1985.

[54] M. Schweiger, *Digitale Signalverarbeitung für die Feedbacksysteme der Elektronenspeicherringe in PETRA und HERA*. Dissertation, Universität Hamburg, 1993. Ph.D. Thesis; Dissertation, Universität Hamburg, 1993.

[55] V. Vendramini, "Traitement du signal numérique pour le système de contre réaction transverse utilisant un seul pick-up avec application dans le SPS et dans le LHC.," tech. rep., CERN, Geneva, 2002.

[56] P. Baudrenghien, W. Höfle, G. Kotzian, and E. Vogel, "Digital Signal Processing for the Multi Bunch LHC Transverse Feedback System," in *Proc. 11th European Particle Accelerator Conference (EPAC'08), Genoa, Italy, 23-27 June, 2008*, European Particle Accelerator Conference, (Genoa, Italy), pp. 3269–3271, June 2008.

[57] S. Myers, "Stabilization of the Fast Head-Tail Instability by Feedback," in *Proc. PAC'87*, pp. 503–508, JACoW Publishing, Geneva, Switzerland, 1987.

[58] G. Lambert, "Filtre numerique en peigne fonctionnant dans une bande totale de 50 MHz." Technical Notes - 1984.

[59] R. Louwerse, "personal communication."

[60] V. Rossi, "Digital Signal Processing Applications and Implementation for Accelerators: Digital Notch Filter with Programmable Delay and Betatron Phase Adjustment for the PS, SPS and LHC Transverse Dampers," tech. rep., CERN, Geneva, 2002.

[61] H. W., "Effects of pacman bunches in the lhc," Tech. Rep. LHC-Project-Report-39 ; CERN-LHC-Project-Report-39, CERN, July 1996.

[62] A. Ribes Metidieri and X. Buffat, "Studies of pacman effects in the hl-lhc," Tech. Rep. CERN-ACC-NOTE-2019-0037, CERN, September 2019.

[63] V. L., "Tune and stability of high intensity bunch trains in the cern sps and lhc," Tech. Rep. LHC-Project-Report-409 ; CERN-LHC-Project-Report-409, CERN, August 2000.

[64] I. M. Solé, H. Bartosik, V. Kain, K. Paraschou, M. Schenk, and C. Zannini, "Characterisation of Bunch-by-Bunch Tune Shift Effects in the CERN SPS," in *Proc. IPAC'22*, no. 13 in International Particle Accelerator Conference, pp. 148–151, JACoW Publishing, Geneva, Switzerland, 7 2022.

[65] S. Poprocki, S. W. Buechele, J. A. Crittenden, K. Rowan, D. L. Rubin, and J. E. San Soucie, "Measurement and modeling of electron-cloud-induced betatron tune shifts at the cornell electron-positron storage ring test accelerator," *Phys. Rev. Accel. Beams*, vol. 22, p. 081001, Aug 2019.

[66] M. Gasior and O. R. Jones, "High Sensitivity Tune Measurement by Direct Diode Detection," in *Proc. DIPAC'05*, JACoW Publishing, Geneva, Switzerland, 2005.

[67] L. Grech, D. Alves, M. Gąsior, S. Jackson, O. Jones, T. Levens, G. Valentino, and J. Wenninger, "An Alternative Processing Algorithm for the Tune Measurement System in the LHC," in *Proc. IBIC'20*, no. 9 in International Beam Instrumentation Conference, pp. 162–165, JACoW Publishing, Geneva, Switzerland, 10 2020. https://doi.org/10.18429/JACoW-IBIC2020-WEPP27.

[68] R. J. Steinhagen, M. Gasior, S. Jackson, and T. G. Lucas, "Tune system performance with/without gating." https://lhc-beam-operation-committee.web.cern.ch/minutes/Meeting51-16_10_2012/2012-10-16_LBOC_Gated_BBQ_Update.pdf.

[69] R. Bartolini and F. Schmidt, "Sussix: A computer code for frequency analysis of non-linear betatron motion," Tech. Rep. SL/Note 98-017 (AP), CERN, June 1998.

[70] A. W. Chao, K. H. Mess, M. Tigner, and F. Zimmermann, *Handbook of Accelerator Physics and Engineering*. WORLD SCIENTIFIC, 2nd ed., 2013.

[71] S. Y. Lee, *Accelerator Physics*. WORLD SCIENTIFIC, 2nd ed., 2004.

[72] E. J. N. Wilson, *An introduction to particle accelerators*. Oxford: Oxford Univ. Press, 2001.

[73] A. Hofmann, "Single-particle dynamics 1 - basic phase space," in *Proc. Joint US-CERN-Japan-Russia School on Particle Accelerators: Beam Measurement*, (Montreux, Switzerland), pp. 3–20, May 11-20 1998.

[74] K. Schindl, "Space charge," in *Proc. CAS Intermediate Accelerator Physics*, (Zeuthen, Germany), pp. 305–320, Sept. 15-16 2003.

[75] A. Koschik, *Simulation of Transverse Multi-Bunch Instabilities of Proton Beams in LHC*. PhD thesis, Institut für Theoretische Physik, Graz Univ. of Technology, Austria, 2004.

[76] F. Ruggiero, ed., *LHC Luminosity and Energy Upgrade: A Feasibility Study*, ch. 6, p. 98. LHC Project Report 626, Dec. 2002.

[77] J. L. Laclare, "Bunched beam coherent instabilities," in *Proc. CAS Accelerator Physics*, vol. 1, (Oxford, UK), pp. 264–326, Sept. 16-27 1985.

[78] F. Pedersen, "Multibunch instabilities," in *5th Joint US-CERN School on Particle Accelerators*, (Benalmádena, Spain), pp. 269–292, Oct. 29-Nov. 4 1992.

[79] Y. H. Chin, "Robinson and coupled-bunch instabilities," in *Proc. Joint US-CERN-Japan-Russia School on Particle Accelerators: Beam Measurement*, (Montreux, Switzerland), pp. 167–177, May 11-20 1998.

[80] Y. H. Chin, "Impedance and wakefields," in *Proc. Joint US-CERN-Japan-Russia School on Particle Accelerators: Beam Measurement*, (Montreux, Switzerland), pp. 152–166, May 11-20 1998.

[81] B. W. Zotter and S. A. Kheifets, *Impedances and Wakes in High-Energy Particle Accelerators*. Singapore: World Scientific, 1998.

[82] L. Palumbo and V. G. Vaccaro, "Wake fields, impedances and green's function," in *Proc. CAS Accelerator Physics*, vol. 1, (Oxford, UK), pp. 341–369, Sept. 16-27 1985.

[83] J. Gareyte, "Beam observation and the nature of instabilities," *AIP Conference Proceedings*, vol. 184, no. 1, pp. 343–429, 1989.

[84] L. Palumbo, V. G. Vaccaro, and M. Zobov, "Wake fields and impedance," in *Proc. CAS 5th Advanced Accelerator Physics Course*, (Rhodes, Greece), pp. 331–390, Sept. 20-Oct. 1 1993.

[85] E. Shaposhnikova, "Signatures of microwave instability," in *Proc. Joint US-CERN-Japan-Russia School on Particle Accelerators: Beam Measurement*, (Montreux, Switzerland), pp. 351–377, May 11-20 1998.

[86] K. Schindl, "Instabilities," in *Proc. CAS Intermediate Accelerator Physics*, (Zeuthen, Germany), pp. 321–342, Sept. 15-16 2003.

[87] A. Hofmann, "Beam instabilities," in *Proc. CAS Course on Synchrotron Radiation and Free-Electron Lasers*, (Brunnen, Switzerland), pp. 139–185, July 2-9 2003.

[88] H. G. Hereward, "Landau damping," in *Proc. CAS Accelerator Physics*, vol. 1, (Oxford, UK), pp. 255–263, Sept. 16-27 1985.

[89] A. Hofmann, "Landau damping," in *Proc. CAS Intermediate Accelerator Physics*, (Zeuthen, Germany), pp. 271–304, Sept. 15-16 2003.

[90] R. P. Walker, "Radiation damping," in *Proc. CAS 5th General Accelerator Physics Course*, (Jyväskylä, Finland), pp. 461–480, Sept. 7 - 18 1992.

[91] A. Ogata, "Analysis of feedback control of transverse beam oscillation by sampled-data theory," *Nuclear Instruments and Methods in Physics Research*, vol. 222, no. 3, pp. 411–419, 1984.

[92] A. V. Oppenheim, R. W. Schafer, and J. R. Buck, *Discrete-Time Signal Processing*. Upper Saddle River, New Jersey: Prentice-Hall Inc., 2nd ed., 1998.

[93] D. Valuch and V. Stopjakova, "New generation of very low noise beam position measurement system for the lhc transverse feedback," *Journal of Physics: Conference Series*, vol. 2420, p. 012073, jan 2023.

[94] B. S. *et al.*, "Update on Beam Induced RF Heating in the LHC," in *Proc. of International Particle Accelerator Conference (IPAC'13), Shanghai, China, 12-17 May, 2013*, International Particle Accelerator Conference, (Shanghai, China), pp. 1646–1648, JACoW, May 2013.

[95] V. M. Zhabitsky, E. V. Gorbachev, N. I. Lebedev, A. A. Makarov, N. V. Pilyar, S. V. Rabtsun, R. A. Smolkov, P. Baudrenghien, W. Höfle, F. Killing, I. Kojevnikov, G. Kotzian, R. Louwerse, E. Montesinos, V. Rossi, M. Schokker, E. Thepenier, and D. Valuch, "LHC Transverse Feedback System: First Results of Commissionning," tech. rep., CERN, Geneva, 2008.

[96] S. L. Hahn, *Hilbert Transforms in Signal Processing*, pp. 193–239. Artech House, 1st ed., 1996.

[97] D. Valúch and V. Stopjakova, "New generation of very low noise beam position measurement system for the lhc transverse feedback," *Journal of Physics: Conference Series*, vol. 2420, p. 012073, jan 2023.

[98] G. Kotzian, W. Höfle, and D. Valuch, "Sensitivity of the LHC Transverse Feedback System to Intra-Bunch Motion," in *Proc. IPAC'17*, pp. 1916–1919, JACoW Publishing, Geneva, Switzerland, 2017.

[99] W. Höfle, F. Dubouchet, G. Kotzian, and D. Valuch, "Performance of the LHC Transverse Damper with Bunch Trains," in *Proc. IPAC'13*, pp. 3022–3024, JACoW Publishing, Geneva, Switzerland, 2013.

[100] G. Kotzian, "Transverse Feedback Parameter Extraction from Excitation Data," in *Proc. IPAC'17*, pp. 1920–1923, JACoW Publishing, Geneva, Switzerland, 2017.

[101] G. Kotzian, "Possibilities for transverse feedback phase adjustment by means of digital filters," *Journal of Physics: Conference Series*, vol. 874, p. 012089, 07 2017.

[102] G. Kotizan, W. Höfle, and E. Vogel, "LHC Transverse Feedback Damping Efficiency," in *Proc. 11th European Particle Accelerator Conference (EPAC'08), Genoa, Italy, 23-27 June, 2008*, European Particle Accelerator Conference, (Genoa, Italy), pp. 3632–3634, June 2008.

[103] K. Ogata, *Modern Control Engineering*. Upper Saddle River, New Jersey: Prentice-Hall Inc., 5th ed., 2010.

[104] M. Söderén *et al.*, "ADT and ObsBox in LHC Run 2, plans for LS2," in *Proc. 9th LHC Operations Evian Workshop*, (Evian Les Bains, France), pp. 165–171, Jan. 2019.

[105] M. Söderén, G. Kotzian, M. O. Sandonís, and D. Valuch, "Online Bunch by Bunch Transverse Instability Detection in LHC," in *Proc. of International Particle Accelerator Conference (IPAC'17), Copenhagen, Denmark, 14-19 May, 2017*, no. 8 in International Particle Accelerator Conference, (Geneva, Switzerland), pp. 397–399, JACoW, May 2017. https://doi.org/10.18429/JACoW-IPAC2017-MOPAB117.

[106] M. Söderén and D. Valuch, "Low Latency, Online Processing of the High-Bandwidth Bunch-By-Bunch Observation Data From the Transverse Feedback System in the LHC," in *EPJ Web Conf., CHEP 2019*, (Adelaide, Australia), p. 01036, Nov. 2019.

[107] R. E. Meller, A. W. Chao, J. M. Peterson, S. G. Peggs, and M. Furman, "Decoherence of kicked beams," Tech. Rep. SSC-N-360, FNAL, May 1987.

[108] B. Goddard, M. J. Barnes, L. Ducimetière, W. Höfle, and G. Kotzian, "Emittance Growth at LHC Injection from SPS and LHC Kicker Ripple," in *Proc. EPAC'08*, pp. 3629–3631, JACoW Publishing, Geneva, Switzerland, 2008.

[109] G. Kotzian, W. Höfle, and E. Vogel, "LHC Transverse Feedback Damping Efficiency," in *Proc. EPAC'08*, pp. 3632–3634, JACoW Publishing, Geneva, Switzerland, 2008.

[110] D. Teytelmann, "Overview of System Specifications for Bunch by Bunch Feedback Systems," in *Proc. Particle Accelerator Conference (PAC'11), New York, USA, March, 2011*, Particle Accelerator Conference, (New York, USA), pp. 1475–1479, March 2011.

[111] H. Hindi, J. Fox, S. Prabhakar, L. Sapozhnikov, G. Oxoby, I. Linscott, and D. Teytelman, "A Formal Approach to the Design of Multibunch Feedback Systems: LQC Controllers," in *Proc. 4th European Particle Accelerator Conference (EPAC'94), London, England, June, 1994*, European Particle Accelerator Conference, (London, England), pp. 1622–1624, June 1994.

[112] C.-Y. Yao, H. Shang, A. Scaminaci, and N. D. Monte, "Application of Z-transform to Noise Response Modeling of a Bunch-by-bunch Feedback System," in *Proc. International Particle Accelerator Conference (IPAC'13), Shanghai, China, June, 1994*, International Particle Accelerator Conference, (Shanghai, China), pp. 3058–3060, Mai 2013.

[113] M. Tobiyama and E. Kikutani, "KEKB Bunch Feedback Systems," in *Proc. International workshop on collective effects and impedance for B-factories (CEIBA95), Tsukuba, Japan, 12-17 Jun 1995*, (Tsukuba, Japan), pp. 470–474, Jun 1995.

[114] R. Kohaupt, "Feedback Systems at DESY," in *Proc. European Particle Accelerator Conference (EPAC'96), Barcelona, Spain, June, 1994*, European Particle Accelerator Conference, (Barcelona, Spain), pp. 180–181, June 1996.

[115] V. Zhabitsky, "Transverse Feedback System with a Digital Filter and Additional Delay," in *Proc. European Particle Accelerator Conference (EPAC'96), Barcelona, Spain, June, 1994*, European Particle Accelerator Conference, (Barcelona, Spain), pp. 1833–1836, June 1996.

[116] M. Dehler, D. Bulfone, R. Kramert, M. Lonza, P. Pollet, and T. Schilcher, "Commissioning Results of the Multi Bunch Feedback System at SLS," in *Proc. 9th European Particle Accelerator Conference (EPAC'04), Lucerne, Switzerland, 5-9 July, 2004*, European Particle Accelerator Conference, (Lucerne, Switzerland), pp. 2508–2510, July 2004.

[117] T. Nakamura, S. Dat'e, K. Kobayashi, and T. Ohshima, "Transverse Bunch-by-Bunch Feedback System for the SPring-8 Stoarge Ring," in *Proc. 9th European Particle Accelerator Conference (EPAC'04), Lucerne, Switzerland, 5-9 July, 2004*, European Particle Accelerator Conference, (Lucerne, Switzerland), pp. 2649–2651, July 2004.

[118] T. Nakamura, K. Kobayashi, W. X. Cheng, T. Honda, M. Izawa, T. Obina, and M. Tadano, "Single-Loop Two-Dimensional Transverse Feedback for Photon Factory," in *Proc. 10th European Particle Accelerator Conference (EPAC'06), Edinburgh, England, 5-9 June, 2006*, European Particle Accelerator Conference, (Edinburgh, England), pp. 3006–3008, June 2006.

[119] D. Bulfone, M. Dehler, V. Forchi, M. Lonza, and L. Zambon, "The ELETTRA Digital Multi-Bunch Feedback Systems," in *Proc. 8th European Particle Accelerator Conference (EPAC'02), Paris, France, 3-7 June, 2002*, European Particle Accelerator Conference, (Paris, France), pp. 2061–2063, June 2002.

[120] A. Menor De Onate and G. Kotzian, "Algorithms for Tune Estimation and Damper Control," tech. rep., CERN, 2023.